

Aalborg Universitet



**AALBORG
UNIVERSITY**

Modeling and Stability Analysis of Converter-Based Wind Turbine Systems

Dimitropoulos, Dimitrios

DOI (link to publication from Publisher):
[10.54337/aau715860557](https://doi.org/10.54337/aau715860557)

Publication date:
2024

Document Version
Publisher's PDF, also known as Version of record

[Link to publication from Aalborg University](#)

Citation for published version (APA):
Dimitropoulos, D. (2024). *Modeling and Stability Analysis of Converter-Based Wind Turbine Systems*. Aalborg University Open Publishing. <https://doi.org/10.54337/aau715860557>

General rights

Copyright and moral rights for the publications made accessible in the public portal are retained by the authors and/or other copyright owners and it is a condition of accessing publications that users recognise and abide by the legal requirements associated with these rights.

- Users may download and print one copy of any publication from the public portal for the purpose of private study or research.
- You may not further distribute the material or use it for any profit-making activity or commercial gain
- You may freely distribute the URL identifying the publication in the public portal -

Take down policy

If you believe that this document breaches copyright please contact us at vbn@aub.aau.dk providing details, and we will remove access to the work immediately and investigate your claim.

**MODELING AND STABILITY
ANALYSIS OF CONVERTER-BASED
WIND TURBINE SYSTEMS**

**BY
DIMITRIOS DIMITROPOULOS**

PhD Thesis 2024



AALBORG UNIVERSITY
DENMARK

Modeling and Stability Analysis of Converter-Based Wind Turbine Systems

Ph.D. Dissertation
Dimitrios Dimitropoulos

Dissertation submitted January 12, 2024

Submitted: January 2024

Main Supervisor: Prof. Frede Blaabjerg
Aalborg University

Co-supervisor: Prof. Xiongfei Wang
KTH Royal Institute of Technology
and Aalborg University

Assessment: Associate Professor Baoze Wei (chairman)
Aalborg University, Denmark
Professor Akshay Rathore
Singapore Institute of Technology, Singapore
Professor Soledad Bernal-Perez
Universitat Politècnica de València, Spain

PhD Series: Faculty of Engineering and Science, Aalborg University

Department: AAU Energy

ISSN: 2446-1636
ISBN: 978-87-94563-08-6

Published by:
Aalborg University Open Publishing
Kroghstræde 1-3
DK – 9220 Aalborg Øst
aauopen@aau.dk

© Copyright: Dimitrios Dimitropoulos

Biography

Dimitrios Dimitropoulos



Dimitrios Dimitropoulos received the MEng in Electrical and Computer Engineering from National Technical University of Athens (NTUA), Athens, Greece, in 2015, and the joint M.Sc. in Energy Innovation from KTH Royal Institute of Technology, Stockholm, Sweden, and UPC – Polytechnic University of Catalonia, Barcelona, Spain, in 2019. Since 2020 he has been working toward the Ph.D. degree in power electronic systems from Aalborg University, Aalborg, Denmark. He completed a research internship in the Power Systems Group at IREC – Catalonia Institute for Energy Research, Barcelona, Spain from October 2018 to January 2019, and a Master thesis project at RISE Research Institutes of Sweden, Gothenburg, Sweden, from February to September 2019. He was a Guest Researcher with Ørsted Wind Power, Fredericia, Denmark, from October 2022 to March 2023. His research interests include modeling, control and stability analysis of converter-based power systems with penetration of wind power.

Abstract

The evolution of societal needs in the 21st century across economic, social, and technological dimensions has been in parallel with an increased energy demand. This phenomenon necessitates the transformation of the existing power grid in order to follow a sustainable path. Therefore, wind power technology has seen significant employment in recent years, and it now constitutes a primary renewable energy source. This shift marks a transition from traditional fossil fuel-based energy generation, leading to rapid advancements in wind turbine technology and an increased share of wind power in global energy production. Power electronic converters play a crucial role in integrating wind farms into the main grid by aligning the demands of the grid with those of wind turbines.

Nevertheless, the transition from synchronous machine-based power systems to converter-based power systems has introduced new stability challenges. These challenges, potentially affecting the system's normal operation, include new categories of system instabilities associated with wind turbine technology. Small-signal dynamics have been identified as a significant cause of instabilities in both low and high-frequency ranges. The focus of this PhD thesis is on the small-signal modeling of wind turbine and wind farm systems, and includes the design and control structure of wind turbine models which are used for implementing stability analysis studies.

Specifically, this PhD thesis investigates the grid-following converter control on the grid-side of wind turbines, with state-space modeling employed for designing the system's small-signal model. The stability of the system is evaluated under various grid strengths, where the tuning of the controllers plays a critical role in ensuring stable operation. In addition, the stability impact of the alternating voltage controller's (AVC) design on the system's stability is under study. The bandwidth of the controllers is examined, both in the inner and outer loops

of grid-following converters in wind turbines, in order to ensure the stability boundaries in each test case. This approach is first utilized to analyze the stability in a single grid-side converter of a wind turbine, and then is expanded to systems with multiple converters of wind turbines. All the examined test cases regarding the stability analysis of the wind turbine's small-signal model are validated by corresponding time domain simulations, ensuring the conclusions of this study.

In addition to controller tuning, the PhD thesis explores hardware solutions in stability analysis. Notably, it addresses the emergence of subsynchronous oscillations observed in large wind farms in recent years. For that purpose, an aggregated wind farm model is used, and the stability impact of incorporating a synchronous condenser into the wind farm's model is examined, particularly in weak grid conditions, to mitigate existing subsynchronous oscillations. Here, the influence of the synchronous condenser's power rating on system stability is highlighted, demonstrating that an inappropriate selection may not adequately mitigate subsynchronous oscillations. The significance of the wind farm's small-signal modeling is underscored, in which a synchronous condenser state-space model is included, as the optimal range of the synchronous condenser's rating is determined for the wind farm system under study.

The findings of this thesis are anticipated to be valuable for future research on the stability of wind farms connected to the main grid, as well as for the industrial aspects of wind power technology.

Dansk Resumé

Udviklingen af samfundsmæssige behov i det 21. århundrede på økonomiske, sociale og teknologiske områder har været parallelt med en øget efterspørgsel efter energi. Dette fænomen nødvendiggør en transformation af det eksisterende elnet for at følge en bæredygtig vej. Derfor har vindkraftteknologi set betydelig anvendelse i de seneste år og udgør nu en primær vedvarende energikilde. Dette skift markerer en overgang fra traditionel energiproduktion baseret på fossile brændstoffer, hvilket fører til hurtige fremskridt inden for vindturbineteknologi og en øget andel af vindkraft i den globale energiproduktion. Konverterere spiller en afgørende rolle i integrationen af vindmølleparker i elsystemet ved at afstemme kravene i nettet med dem fra vindturbinerne.

Ikke desto mindre har overgangen fra strømsystemer baseret på synkromaskiner til konverterbaserede elsystemer introduceret nye stabilitetsudfordringer. Disse udfordringer, som potentielt kan påvirke systemets normale drift, inkluderer nye kategorier af systeminstabiliteter forbundet med vindturbineteknologi. Småsignal dynamik er blevet identificeret som en betydelig årsag til ustabiliteter i både lave og høje frekvensområder. Fokus for denne ph.d.-afhandling er på småsignalmodellering af vindturbin- og vindmølleparksystemer og omfatter design og kontrolstruktur af vindturbinmodeller, der anvendes til gennemførelse af stabilitetsanalysestudier.

Specifikt undersøger denne ph.d.-afhandling kontrol af grid-following konverterere på netside af vindturbiner, med tilstandsrummodellering anvendt til at designe systemets småsignalsmodel. Systemets stabilitet vurderes under forskellige netstyrker, hvor tuning af kontrollerne spiller en kritisk rolle i at sikre stabil drift. Derudover undersøges stabilitetspåvirkningen af vekselsstrømskontrollerens (AVC) design på systemets stabilitet. Kontrollerens båndbredde undersøges, både i de indre og ydre løkker af grid-following konverterere i vind-

turbiner, for at sikre stabilitetsgrænserne i hvert testtilfælde. Denne tilgang anvendes først til at analysere stabiliteten i en enkelt grid-following konverter af en vindturbine, og derefter udvides den til systemer med flere konvertere af vindturbiner. Alle de undersøgte testtilfælde vedrørende stabilitetsanalysen af vindturbinens småsignalsmodel valideres ved tilsvarende tidsdomænesimuleringer, hvilket sikrer konklusionerne af denne undersøgelse.

Ud over tuning af kontrollere udforsker ph.d.-afhandlingen hardwareløsninger i stabilitetsanalyse. Bemærkelsesværdigt adresserer den fremkomsten af subsynkroner svingninger observeret i store vindmølleparker i de senere år. Til dette formål anvendes en aggregeret vindmølleparkmodel, og stabilitetspåvirkningen af at inkorporere en synkronkondensator i vindmølleparkens model undersøges, især i svage netforhold, for at afhjælpe eksisterende subsynkroner svingninger. Her fremhæves indflydelsen af synkronkondensatorens effektrating på systemstabilitet, hvilket demonstrerer, at et upassende valg muligvis ikke tilstrækkeligt kan afhjælpe subsynkroner svingninger. Betydningen af vindmølleparkens småsignalsmodellering understreges, hvor en synkronkondensator state-space model er inkluderet, da det optimale område for synkronkondensatorens rating bestemmes for vindmølleparkssystemet under undersøgelse.

Resultaterne af denne afhandling forventes at være værdifulde for fremtidig forskning i stabiliteten af vindmølleparker tilsluttet hovednettet, samt for de industrielle aspekter af vindkraftteknologi.

Contents

Biography	iii
Abstract	v
Dansk Resumé	vii
Thesis Details	xiii
Preface	xv
I Report	1
1 Introduction	3
1.1 Background	3
1.1.1 Wind Power Technology	5
1.1.2 Stability and Control in Modern Power Systems	11
1.1.3 Small-Signal Stability in Wind Turbine Systems	17
1.1.4 State-of-the-art in Small-Signal Modelling with Grid-Following Control	21
1.1.5 Mitigating of Sub-synchronous Oscillations in Wind Farms	22
1.1.6 State-of-the-art in Mitigation of SSOs with a Synchronous Condenser	25
1.2 Thesis Motivation and Research Tasks	25
1.2.1 Research Questions and Objectives	26
1.2.2 Project Limitations	28
1.3 Thesis Outline	29

1.4	List of Publications	31
2	Small-Signal Stability of Grid-Following Wind Turbine	33
2.1	Background	33
2.2	State-Space Modeling of Wind Turbines Grid-Side Control	34
2.2.1	dq - Transformation	35
2.2.2	Phase-Locked Loop (PLL) and its Design	37
2.2.3	Current Controllers (CC) and their Design	39
2.2.4	Time Delay	43
2.2.5	LC Filter and Grid Impedance	44
2.3	Grid Strength Definition and Small-Signal Stability Assessment .	45
2.3.1	Stability Impact of Current Controller for Different Grid Strengths	47
2.3.2	PLL dynamics in Weak Grid Case	47
2.4	Conclusion	53
3	Stability Impact of Alternate Voltage Controller (AVC) on Wind Turbines	55
3.1	Background	55
3.2	Updated State-Space Modeling	56
3.2.1	Alternate Voltage Controller (AVC) Modeling	57
3.3	Small-Signal Stability Analysis Assessment	59
3.3.1	Equilibrium Points Computation	59
3.3.2	Eigenvalue Analysis Concerning PLL and AVC Critical Bandwidth	60
3.3.3	Time-Domain Stability Analysis	65
3.4	Stability Region Mapping of PLL and AVC for Different Cases of AVC's LPF	73
3.4.1	Weak Grid Case Scenario	73
3.4.2	Strong Grid Case Scenario	75
3.5	Small-Signal Analysis in Multi-Converter System	76
3.5.1	Eigenvalue Stability Analysis and Time Domain Analysis in Multi-Converter Model	79
3.6	Conclusion	85

Contents

4	Modeling and Mitigation of Subsynchronous Oscillations in Wind Farms	89
4.1	Background	89
4.2	Wind Farm's Small-Signal Model with HVAC Connection	90
4.2.1	Aggregated Wind Turbine Model	90
4.2.2	HVAC Transmission System Model	91
4.2.3	Wind Farm Model Accuracy through Eigenvalue-Based Stability Analysis	96
4.3	Mitigation of Subsynchronous Oscillations with Synchronous Condenser	100
4.3.1	Synchronous Condenser's State-Space Model	101
4.3.2	Stability Impact of Synchronous Condenser's Rating	109
4.4	Conclusion	112
5	Conclusion	115
5.1	Summary	115
5.2	Main Contributions of the Thesis	117
5.3	Research Perspectives and Future Work	119
	References	121
	References	121

Thesis Details

Thesis Title: Modeling and Stability Analysis of Converter-Based Wind Turbine Systems
Ph.D. Student: Dimitrios Dimitropoulos
Supervisors: Prof. Frede Blaabjerg, Aalborg University
Prof. Xiongfei Wang, KTH Royal Institute of Technology and Aalborg University

The main body of this thesis consist of the following papers:
Publications in referred journals:

- [J1] **D. Dimitropoulos**, X. Wang and F. Blaabjerg, “Stability Impacts of an Alternate Voltage Controller (AVC) on Wind Turbines with Different Grid Strengths,” *Energies*, vol. 16, no. 3, 2023, Art. no. 1440.
- [J2] **D. Dimitropoulos**, M. K. Bakhshizadeh, L. Kocewiak, X. Wang and F. Blaabjerg, “Impact of Synchronous Condenser’s Rating on Mitigating Subsynchronous Oscillations in Wind Farms,” submitted to *IEEE Access*.
- [J3] **D. Dimitropoulos**, X. Wang and F. Blaabjerg, “Stability Analysis in Multi Voltage-Source Converter Systems of Wind Turbines,” submitted to *Elsevier’s e-Prime - Advances in Electrical Engineering, Electronics and Energy*.

Publications in referred conferences:

- [C1] **D. Dimitropoulos**, X. Wang and F. Blaabjerg, “Small-Signal Stability Analysis of Grid-Connected Converter under Different Grid Strength

Cases,” in *Proc. 2022 IEEE 13th International Symposium on Power Electronics for Distributed Generation Systems (PEDG)*, Kiel, Germany, 2022, pp. 1-6.

This dissertation has been submitted for assessment in partial fulfillment of the Ph.D. degree. Based on the publications shown above, the thesis serves as a summary of those, highlighting the primary outcome of the Ph.D. project. Parts of the results are used directly or indirectly in the extended summary of the thesis. The co-author statements have been made available to the assessment committee and are also available at the Faculty of Engineering and Science, Aalborg University.

Preface

This dissertation summarizes the outcomes of the PhD project 'Modeling and Stability Analysis of Converter-Based Wind Turbine Systems' performed at AAU Energy, Aalborg University, Denmark. This PhD project has been supported by the WinGrid consortium (Wind farm – grid interactions: exploration and development), funded by the H2020-MSCA-ITN programme. Therefore, I would like to acknowledge the WinGrid consortium for funding my PhD project, and thank all its members - professors and PhD students - for the interactions we had.

I would like to express my gratitude to my main supervisor, Professor Frede Blaabjerg, for his constant guidance, support, encouragement, and patience during my PhD studies. His in-depth knowledge in the field of power electronics, his passion for research and his leadership skills will always inspire me not only as an engineer and researcher, but also as a person, and I consider our collaboration a great privilege. Additionally, I would like to thank my co-supervisor, Professor Xiongfei Wang, for the many discussions we had on my research topics and the ideas he provided that helped me to face many challenges. His commitment to hard work motivated me to do the same and overcome any obstacles I encountered.

Special thanks go to Dr. Mads Graungaard Taul, who also co-supervised me during my first year. His ideas and assistance have been invaluable, not only for a good start in my project but also for a smooth beginning in a new city and working environment. In addition, I would like to thank all my colleagues at AAU Energy, Aalborg University, for the discussions we had, as well as their help and support in various aspects during my PhD studies.

I also want to thank Dr. Lukasz Kocewiak and Dr. Mohammad Kazem Bakhshizadeh, who supervised me during my external stay at Ørsted S/A in

Gentofte. They offered great ideas to expand the topic of my research, but most importantly, they provided deep insights into how the wind power industry operates. I really enjoyed the time I spent in Gentofte, and I have great memories from all the members of the Power System Solutions Department, as they made me feel like a true member of their group.

I wish to thank my friends and family for their support during my work at Aalborg University. Even short talks about irrelevant matters helped me to cope with stress during my PhD studies, especially in times when I felt like being at a dead end with my research.

Last but definitely not least, I wish to acknowledge the great love and support I received from my wife, Despina. Despina and I have been together since my first year as an undergraduate student in Greece, and she has always encouraged me to follow my dreams and achieve my ambitions. She is a person who drives me to become better, and this PhD would not have been accomplished without her.

Dimitrios Dimitropoulos
Aarhus, January 12, 2024

“Σὰ βγεῖς στὸν πηγαμὸ γιὰ τὴν Ἰθάκη, νὰ εὐχεσαι νᾶναι μακρὺς ὁ δρόμος, γεμάτος περιπέτειες, γεμάτος γνώσεις.”

"When you depart for Ithaca, wish for the road to be a long one, full of adventure, full of knowledge."

– *Constantine P. Cavafy*

Part I
Report

Chapter 1

Introduction

1.1 Background

The power system has undergone significant transformation in the last decade. The conventional ways of electric power generation through the burning of fossil fuels, such as coal, is being gradually replaced by alternative technologies based on wind and solar power. The power electronic converter technology is the key element that enables the large-scale integration of renewable energy sources into modern power systems. To transmit the substantial amounts of renewable electricity generated from sources like offshore wind farms over long distances, High Voltage Direct Current (HVDC) technology can be employed. If the distance is short, it will be done by high voltage AC cables. Fig. 1.1 illustrates the representation of a modern grid.

Therefore, as fossil fuel-based energy sources are being replaced with renewable energy sources to electrify the main grid, investments in new renewable power assets have constantly surpassed those in new fossil fuel-powered plants between 2015 and 2021, according to the latest report jointly prepared by the International Renewable Energy Agency (IRENA) and Climate Policy Initiative (CPI). Notably, renewable capacity experienced a remarkable growth of 130% from 2011 to 2021, compared to a mere 24% growth in non-renewable capacity (Fig. 1.2), with solar photovoltaic (PV) demonstrating the most rapid expansion [2].

Wind power generation has played a significant role in the transition to the carbon free power system. Based on the latest Renewables Global Status Report

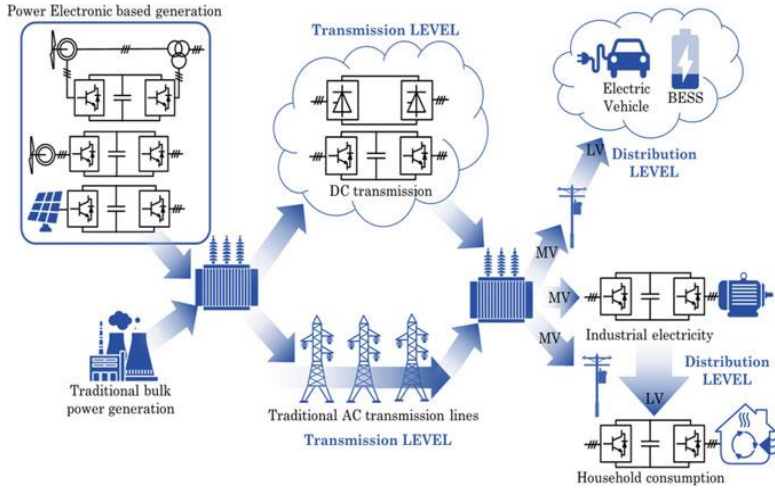


Fig. 1.1: Modern power system with power electronic converter applications [1].

(GSR) by the Renewable Energy Policy Network for the 21st Century (REN21), more than 77 GW of wind power capacity was added globally in 2022, including 68.4 GW onshore and nearly 8.8 GW offshore, resulting in a 9% increase in total operating capacity to an estimated 906 GW, as shown in Fig. 1.3. This made 2022 the third-largest year for new wind power installations. However, compared to 2021, global grid-connected additions declined by over 17% (5% onshore and 58% offshore) primarily due to slowdowns in China and the United States. Europe was the only region where installations increased in 2022 [3].

Looking ahead, Global Wind Energy Council (GWEC) projects a global addition of 680 GW of wind capacity between 2023 and 2027, with 130 GW of that being offshore capacity, as illustrated in Fig 1.4. Onshore wind installations in China are expected to lead the way with 300 GW, followed by Europe with nearly 100 GW. Offshore wind energy will play an increasingly significant role, with an estimated global addition of over 60 GW between 2023 and 2025, and 68 GW in 2026–2027. Wind energy is expected to achieve the milestone of 2 TW of installed capacity by the end of 2030 [4].

1.1. Background

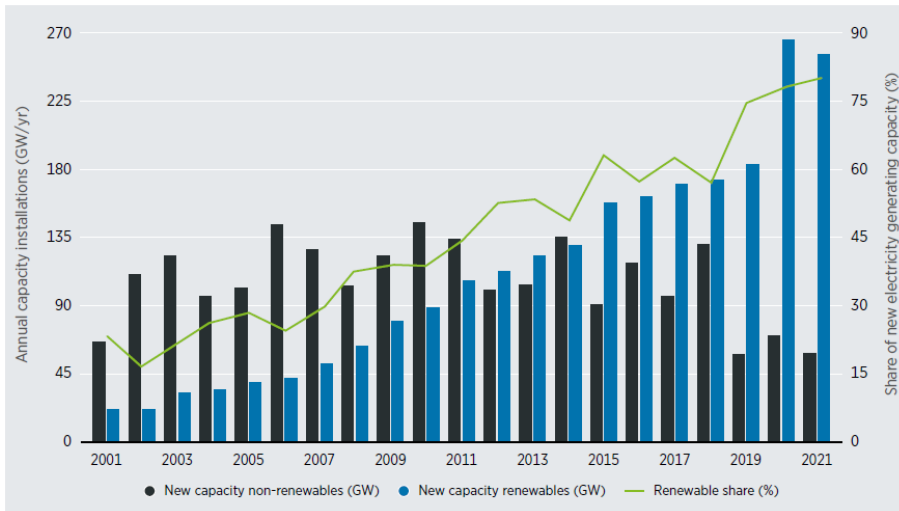


Fig. 1.2: Share of new electricity capacity in the period 2001-2021 [2].

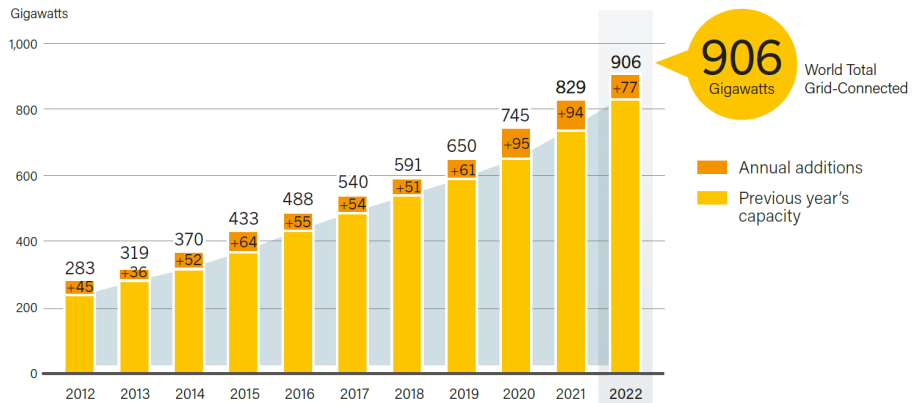


Fig. 1.3: Global Capacity and Annual Additions of Wind Power 2012-2022 [3].

1.1.1 Wind Power Technology

As already analyzed, wind farms significantly contribute to the electric power generation nowadays, and they have an increasingly important impact on the

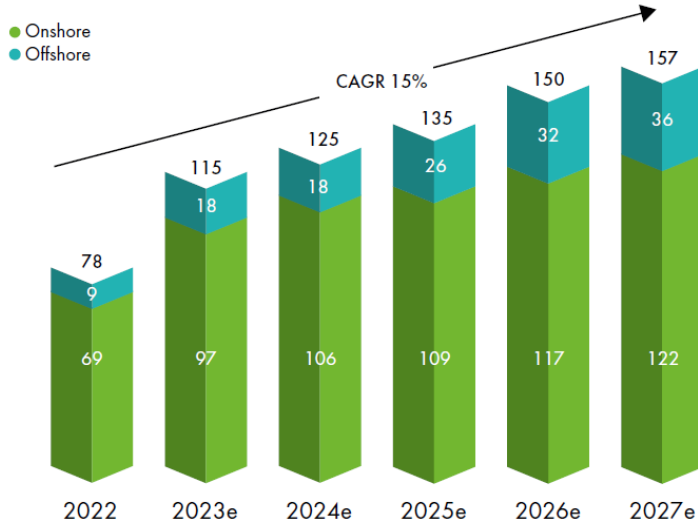


Fig. 1.4: Future global wind power installations 2022-2026 [4].

power system stability as well as the power quality. The expectations for wind power generating units include regulation of active and reactive power, maintaining voltage and frequency control, and fast response to dynamic and transient phenomena [5]. The power electronic technology plays a critical role in wind farm control and system configuration in order to meet these requirements. Power electronic converters align the characteristics of wind turbines with grid demands such as voltage, frequency, active power and reactive power control [6].

A wind turbine system consists of a turbine rotor, a generator, a gearbox that adjusts the turbine rotor's low speed to match the generator's higher speed, a power electronic system, and a grid-connecting transformer. The power electronic system includes back-to-back voltage-source converters (VSCs) to interface wind turbine generators with the grid. The commonly used generators for variable-speed, pitch-regulated wind power generation are the Type-3 doubly-fed induction generator (DFIG) and the Type-4 permanent magnet synchronous generator (PMSG) [7], which are shown in Figs. 1.5 and 1.6, respectively.

Introduced in 1996 by many wind turbine manufacturers, DFIG technology offered flexibility over constant speed wind turbines prevalent until then, par-

1.1. Background

ticularly in terms of power quality and energy yield [5]. With the stator of the DFIG directly grid-connected and the rotor connected via back-to-back converters, this design advantageously allows a fraction of the power production to be fed through the power converter system. As such, the power electronic converter system's nominal power can be less than the wind turbine's nominal power [8], allowing the rotor speed variation within $\pm 30\%$ of the wind power. The control system of a wind turbine with a DFIG topology must limit the power during high wind speeds, adjust the active power drawn to track the maximum operating point, and regulate reactive power exchanged with the grid on demand. Today, wind turbine systems using DFIG topology constitute 50% of the wind energy market [7].

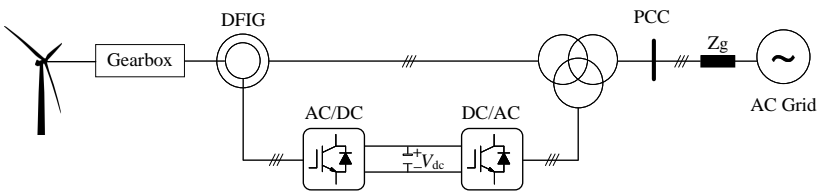


Fig. 1.5: Type-3 Wind turbine system with doubly-fed induction generator (DFIG).

The adoption of full-scale converter systems with PMSG gained popularity after 2005 due to their better grid fault ride-through characteristics compared to DFIG [9]. PMSG, primarily excited by permanent magnets, is a cost-effective and appealing choice [6]. It is also an efficient option, with 65% lower power losses than a typical DFIG wind turbine system [10]. Gearbox omission, an option in PMSG systems, has the advantage of noise reduction [11]. A full-scale power converter system enables PMSG-equipped wind turbines to fully control active and reactive power. As in DFIG systems, the generator of PMSG systems is decoupled from the grid by the DC link and can operate across a wide frequency range for optimal performance. At the same time, the grid-side converter independently controls active and reactive power generation, enhancing the system's dynamic response [6]. Nonetheless, full-scale converters experience higher losses and costs than partly-rated converters with DFIG [5].

When considering the power generation at the wind farm scale, two key factors must be addressed. Firstly, due to the high cost of energy, the efficiency of power transmission is of great importance. Secondly, the significant power

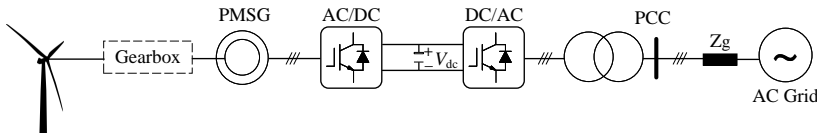


Fig. 1.6: Type-4 Wind turbine system with permanent magnet synchronous generator (PMSG).

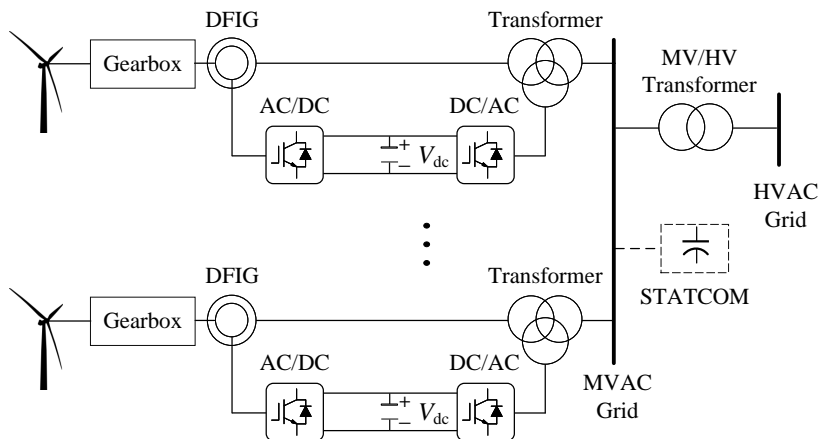
capacity of wind farms necessitates an active role in supporting the power grid. Therefore, the wind farm's configuration and the design are of vital importance [12].

Figs. 1.7 and 1.8 illustrate primary electrical configurations of wind farms utilizing these technologies. Fig. 1.7a shows a wind farm equipped with DFIG and power electronics. This configuration enables both active and reactive power control and variable speed operation of wind turbines, maximizing energy capture while reducing mechanical stress and acoustic noise [6]. The reactive power capability is limited in this configuration, necessitating the use of a static synchronous compensator (STATCOM) to comply with certain grid requirements [5]. In fact, STATCOMs are required in case of long AC lines to maintain the allowed AC voltage level [13]. Fig. 1.7b depicts a wind farm employing a full-scale power converter system with PMSG. This configuration offers extended reactive power capability compared to DFIG-based wind farms, as the grid-side converter provides the required reactive power for each generation unit [5].

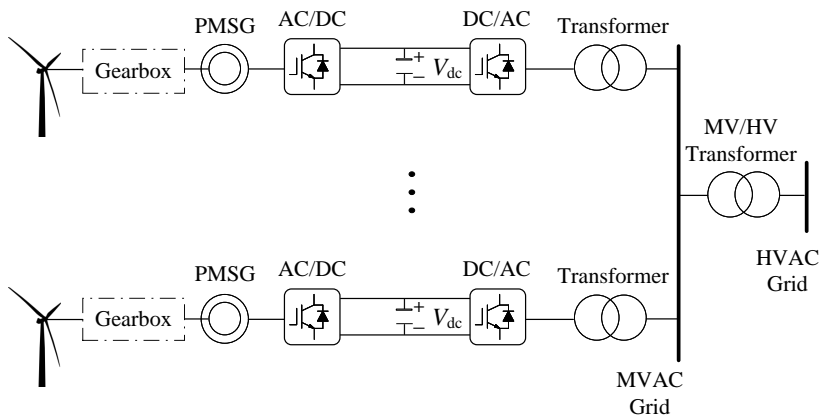
When dealing with long distances, for example in offshore wind farms, high-voltage dc (HVDC) technology has been employed in recent years. HVDC transmission is an important option, as it can achieve high power transfer with high transmission efficiency [12]. Furthermore, there is no reactive power during power transmission; therefore, reactive power compensators, like STATCOMS, are unnecessary in HVDC systems, as power can be transferred over long distances with constant voltage at the receiving end. DC lines can also transfer higher power with the same size and insulation level compared to AC lines; this allows for smaller cable sizes in the DC system [13].

Various configurations are feasible for HVDC transmission systems, as illustrated in Fig. 1.8a and Fig. 1.8b. In the configuration shown in Fig. 1.8a, the medium AC voltage from the wind farm undergoes conversion to high DC voltage on the transmission side, facilitated by a boost transformer. This DC power

1.1. Background



(a) Wind farm configuration based on DFIG system with ac grid

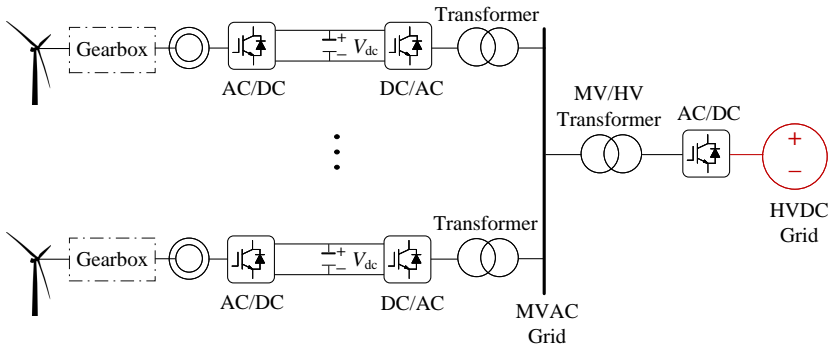


(b) Wind farm configuration based on full-scale converter system with ac grid

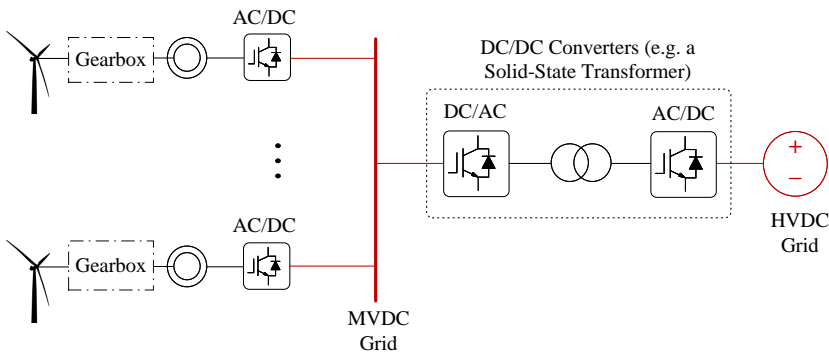
Fig. 1.7: Wind farm configurations with ac power transmission [12].

is then transferred to the onshore system, where it is converted back to the AC voltage. For the power conversion at high voltage, either half-controlled power semiconductors, such as thyristors, or fully controlled power semiconductors like insulated-gate bipolar transistors (IGBTs) in series, may be deployed [5]. In Fig. 1.8b, HVDC transmission is achieved through the use of fully active con-

trollable power converters, specifically, solid-state transformers (SSTs). In this case, the low-to-medium voltage (LV/MV) from the wind turbines is converted to a medium-to-high DC voltage for transmission. This setup enables full DC power delivery across both distribution and transmission lines. Consequently, the overall efficiency of wind power delivery is improved compared to the configuration presented in Fig. 1.8a, as a result of the reduction in the number of required converters and transformers [5, 12].



(a) Wind farm configuration based on full-scale converter system with VSC rectifier and transmission dc grid



(b) Wind farm configuration based on full-scale converter system with both dc distribution and dc transmission grid

Fig. 1.8: Wind farm configurations with dc power transmission [5].

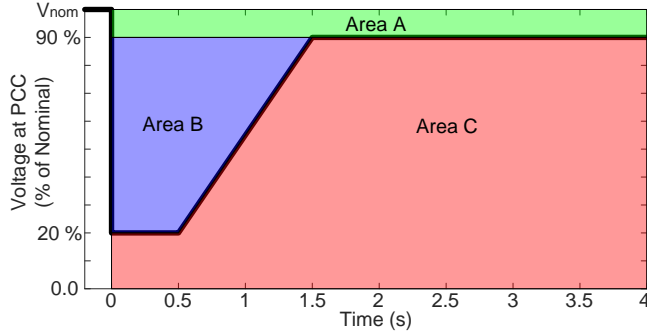
1.1. Background

1.1.2 Stability and Control in Modern Power Systems

Despite the several advantages of the increase in wind power penetration to the modern power systems, the transition from synchronous generators to VSCs has led to the appearance of oscillations in a wide range of frequencies. Therefore, stability issues are likely to occur and the overall power system reliability could be threatened. Stability issues are related to the grid requirements, since grid operators have specified the requirements for the integration of wind power plants and the contribution to ancillary services to the system. In Denmark, a wind power plant must be designed to withstand voltage dips down to 20% of the voltage in the point of common coupling (PCC) over a period of minimum 0.5 seconds without disconnecting, as shown in Fig. 1.9a. Area A represents post-disturbance situations where the wind power plant must stay connected to the system with normal production, and Area C the cases where the wind power plant's disconnection is allowed. Area B corresponds to post-disturbance situations where the wind power plant should stay connected and provide voltage support to the system by supplying controlled reactive current. In that way the voltage is stabilized after a disturbance. The reactive current requirements during voltage dips for the Danish grid are shown in Fig. 1.9b [14].

In general, power systems are exposed to two main types of disturbances: small-signal disturbances and large-signal disturbances. Small-signal disturbances, such as fluctuations in load, demand that the system adjusts its operation in order to continue functioning smoothly. Large-signal disturbances, typically severe incidents like a major generator loss or a short circuit in a transmission line, require the system to be able to overcome them; structural changes may also occur, as a result of isolating the faulted elements in order to sustain normal operations [15].

Power system stability measures the system's resilience to return to an operational equilibrium from a disturbed initial condition. The success of this recovery largely depends on the system variables maintaining specific limits, which helps to keep the entire system largely stable [16]. Conventionally, the dynamic traits of power systems were predominantly determined by the performance of synchronous generators, their controlling mechanisms, and the dynamic attributes of the loads. Prior studies, therefore, mainly concentrated on slower, electromechanical phenomena prevalent in systems governed by synchronous machines [15]. Fast transients associated with the network and fast-response devices were often considered out of scope and ignored as they usually dissipate rapidly



(a) Voltage dip tolerance requirements

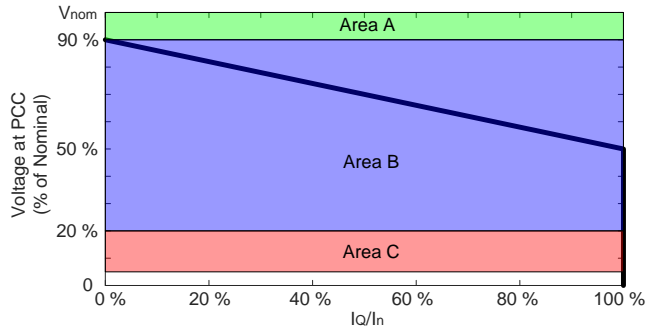
(b) Reactive current I_Q injection requirements

Fig. 1.9: Grid code requirements from the Danish transmission system operator Energinet for wind power plants [14].

in the power system [17].

However, as mentioned in subsection 1.1.1, a significant transformation of the global electric power systems is taking place, primarily characterized by the increased deployment of power electronic converter interfaced technologies, with a focus on VSC technology [18]. The extensive integration of such technologies into generation, load, and transmission has shifted the dynamic response of power systems to rely more heavily on these fast-response power electronic devices. This shift has brought a change into the power system's dynamic behavior, leading to a fundamental difference in the grid-synchronization dynamics of converter-based resources compared to synchronous machines, and it has be-

1.1. Background

come crucial to rethink the categorization of stability [16]. The updated power system stability categories are depicted in Fig. 1.10.

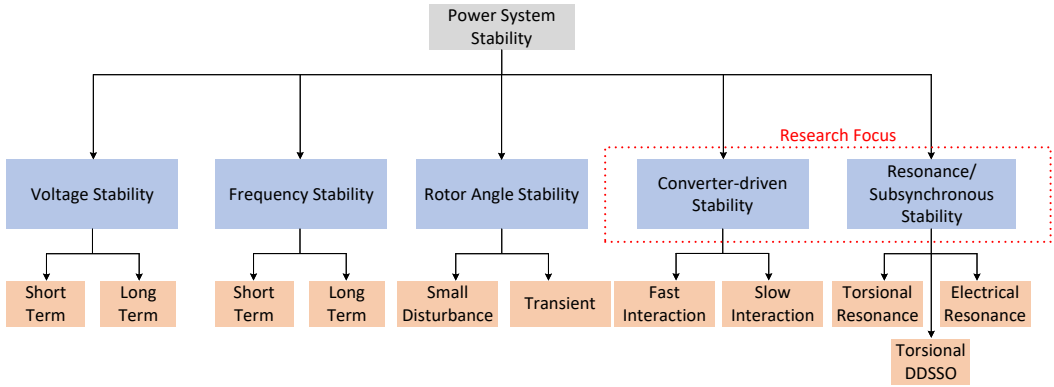


Fig. 1.10: Classification of power system stability in power electronic-based power systems [16]. DDSSO: Device-dependent subsynchronous oscillations.

The classical power system stability categories in traditional power systems are including voltage, frequency and rotor-angle stability.

- **Voltage stability:** Voltage stability refers to a power system’s capacity to maintain steady voltages at all buses in the system, keeping them close to the nominal value after experiencing a disturbance [15]. The stability relies on the ability to balance a load demand and supply from the power system [19].

Depending on the timeframe under consideration, voltage stability can be presented as a short-term or a long-term phenomenon. Short-term voltage stability is related with the dynamics of fast acting load elements such as induction motors, electronically managed loads, HVDC links, and inverter-based generators. For this type of stability, comprehensive dynamic load modeling is of vital importance, with the primary concern being short circuit faults near load areas [16].

In contrast, long-term voltage stability is concerned with slower responding equipment, including tap-changing transformers, thermostatically controlled loads, and generator current limiters. It usually emerges as a gradual reduction of voltages at certain network buses. This stability is typi-

cally not triggered by an initial fault, but rather by the subsequent outage of transmission and generation equipment post fault clearance [16].

- **Frequency stability:** Frequency stability represents a power system's ability to preserve a constant frequency after experiencing a substantial system disruption, which leads to an imbalance between load and generation. The success of this stability depends on the ability to reestablish and uphold a balance between the system's generation and load, with the least possible unintentional load shedding [15].

The characteristic time of the processes and devices activated to regain stability can determine whether the frequency stability manifests as a short-term or a long-term phenomenon. In fact, there are typically three distinct phases during an incident that cause a decrease in frequency within a system predominantly governed by synchronous generators: (i) the initial inertia response from the synchronous generators, (ii) the primary frequency response from both generators and load damping, and (iii) the automatic generation controls that restore the frequency to its nominal value.

These stages highlight the vital controls and responses necessary to maintain frequency stability in the system.

- **Rotor angle stability:** Rotor angle stability involves the competency of the interconnected synchronous machines within a power system to remain in synchronism under normal operating conditions and to regain synchronism following small or large disturbances [15].

Rotor angle stability can be categorized into small-disturbance stability and transient stability. Small-disturbance oscillatory stability arises mainly due to the absence of adequate negative damping torque, whereas negative or insufficient synchronizing torque leads to transient instability.

The rise of converter technology in power systems has brought changes into the above-mentioned traditional stability categories. With regard to rotor angle stability, the converter technology affects both small-disturbance stability and transient stability. This impact is due to the diminished inertia following the displacement of conventional synchronous generators [20]. However, other factors, such as the type of controls and the number of converter-based generating units, may also be influential. Furthermore, the converter technology can significantly contribute to frequency stability, especially by regulating the system

1.1. Background

frequency. In fact, due to the high penetration of converters altering the frequency response of power systems to resemble that of smaller systems, tuning of converter controls becomes crucial for these systems to offer a fast primary frequency response [21].

However, even if the converter technology can provide frequency stability, it significantly influences the dynamic behavior and oscillatory phenomena of modern power systems. In particular, systems based on power converters contribute limited short-circuit current, typically varying from 0 to 1.5 per unit (pu) for a fully interfaced converter resource. The Phase-Locked Loop (PLL) and the inner-current control loop are key components in the system's dynamic recovery post-disturbance. In settings with a low short-circuit ratio (SCR), the responses of the inner current-control loop and the PLL can be seen as oscillations through a coupling mechanism. This oscillatory behavior can be attributed to the PLL's slower synchronization with network voltage and high gains in the inner-current control loop and PLL. The specific SCR at which these oscillations occur can fluctuate, but are likely to happen when the SCR falls below 1.5 to 2 [16].

Consequently, the increasing converter penetration has led to the introduction of two new stability classes, which are the converter-driven and the resonance stability.

- **Converter-driven stability:** Converter-driven stability is related to the dynamic behavior of converter-based systems, as a result of the VSC interface with the grid [22]. The wide timescale dynamics of Converter Interfaced Generators' (CIGs) controls can incite cross-couplings with the electromechanical dynamics of machines and electromagnetic transients in the network. These interactions can potentially trigger unstable power system oscillations over a broad frequency spectrum [23]. Converter-driven instabilities are categorized into slow-interaction converter-driven stability (typically at low frequencies, less than 10 Hz) and fast-interaction converter-driven stability (generally at higher frequencies, from tens to hundreds of Hz, and potentially extending into the kHz range).

Fast-interaction converter-driven stability is associated with power system instabilities caused by fast converter interactions. Such interactions occur between the fast inner-current loops of converter-based systems and power electronic-based systems like HVDC and Flexible AC Transmission Systems (FACTS), as well as the passive components in the power system.

These interactions can induce harmonic instability typically in the hundreds of Hz to several kHz range [24,25]. The fast interactions can also be stimulated by the presence of multiple inverters in close proximity [26,27], as well as high-frequency converter switching that may activate parallel and series resonances related to the power filters - which often have an LCL structure - or parasitic feeder capacitors [25].

On the other hand, slow-interaction converter-driven stability relates to instabilities caused by slower dynamic interactions between the control systems of the power electronic converters and the slow-response components of the power system. These slower dynamics include the electromechanical dynamics of synchronous generators and certain generator controllers. The subsynchronous oscillations (SSOs) indicative of instability predominantly arise from outer control loops, such as the voltage and power controller, and the PLL of VSC-based systems [24,28]. Indeed, the respective gains and bandwidths of these controllers impact low-frequency oscillations. Furthermore, weak grid conditions - with a SCR of 2 or less - along with the tuning of outer loop control parameters, can also induce low-frequency instability phenomena [28–30].

- **Resonance stability:** Resonance stability is concerned with resonance that occurs when energy is exchanged in an oscillatory manner between components in the power system. The growth of these oscillations, often manifested in the amplification of voltage, current, or even torque magnitudes within electrical power systems, indicates a lack of sufficient energy dissipation in the flow path, leading to resonance instability [16]. This concept can be further subdivided into "Torsional Resonance" and "Electrical Resonance," both of which encompass SSOs.

In the context of conventional power systems featuring synchronous generators, torsional resonance was the only form of resonance stability. It is related to the torsional interactions between the series compensated lines and the turbine-generator mechanical shaft. Subsynchronous torsional oscillations can be further divided into subsynchronous resonance (SSR) and device-dependent subsynchronous oscillations (DDSSO). SSR is a condition in an electrical power system where substantial energy is exchanged with a turbine-generator at one or more of the natural subsynchronous torsional oscillation modes of the combined turbine-generator mechanical

1.1. Background

shaft [31]. DDSSO, on the other hand, arises from the interaction of fast-acting control devices, such as HVDC lines and Flexible AC Transmission Systems (FACTS) like STATCOMs and Static Var Compensators (SVCs), with the torsional mechanical modes of nearby turbine-generators [31].

Electrical resonance has been observed in converter-based systems with induction generators; more specifically, it results from the interaction between variable speed induction generators used in DFIG (see also Fig. 1.5) and the series compensation. In fact, the self-excitation type SSR occurs when the series capacitor forms a resonant circuit at subsynchronous frequencies with the effective inductance of the induction generator. At these frequencies, the overall apparent resistance of the circuit becomes negative, prompting subsynchronous oscillations. As the control action of DFIG converter controls is the primary factor in generating negative damping at these electrical resonant frequencies, these oscillation phenomena are referred to as subsynchronous control interaction (SSCI). Various events involving DFIGs and series compensation that led to SSCI phenomena are investigated in [32–37].

1.1.3 Small-Signal Stability in Wind Turbine Systems

As previously discussed, the shift from conventional power grids based on synchronous machines to those driven by converters has not only enhanced the grid's efficiency and flexibility but also introduced documented stability challenges [23]. Power converters of wind turbines are typically equipped with multi-timescale control systems that regulate the current and power exchanged with the grid [38]. These converters' extensive timescale control dynamics can interact with the electromechanical dynamics of electrical machines and power networks' electromagnetic transients, potentially leading to converter-driven or electrical instability, which can be present in a broad frequency range [39].

Fig. 1.11 presents a Type-4 full-scale wind turbine system, in which the two control structures of the back-to-back converter topology are presented; these are the machine-side converter (MSC) control and the grid-side converter (GSC) control. The research in this thesis is based on the grid-following control of the GSC, where a PLL is utilized to estimate the phase of the voltage at the PCC to keep synchronization with the grid; this control scheme is also similar in Type-3 DFIG wind turbine systems. Fig. 1.12 illustrates the general grid-following

control structure of the GSC in Fig. 1.11, with an overview of the frequency range of oscillations that each controller might cause. The control loops of the VSC consist of the inner current control loop (CC), PLL, Direct Voltage Control (DVC), and Alternating Voltage Control (AVC).

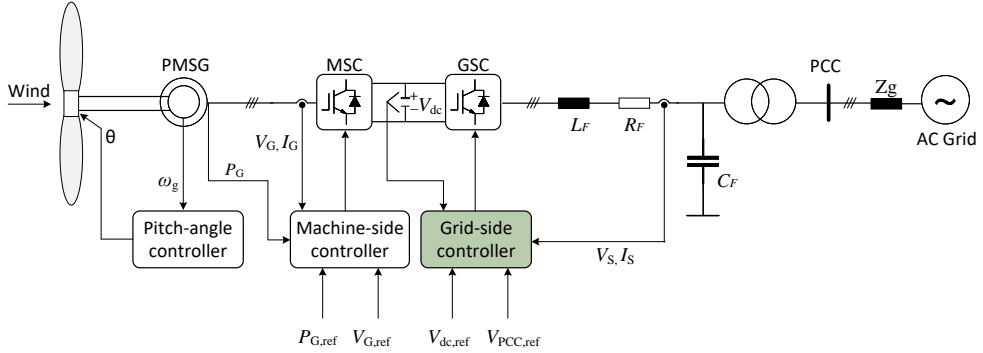


Fig. 1.11: Type-4 full-scale wind turbine system with its control structure.

The primary cause of these harmonics and resonances in power electronic-based systems is the small-signal dynamics of converters. This is because converters often introduce a negative damping effect in the power system, which can occur in different frequency ranges depending on the converters' specific controllers and the conditions of the power system [29, 40–43]. For example, the PLL and the digital control system's time delay add a negative damping effect in the low and high-frequency range, respectively [41, 42].

Hence, the small-signal stability analysis of wind power generation systems has gained increasing attention. To date, small-signal models of DFIG and PMSG wind turbines have been developed and analyzed [44]. There are two primary approaches for system-level analysis of small-signal stability: the eigenvalue analysis based on the state-space model, and the frequency-domain impedance-based analysis [45].

The eigenvalue analysis method, founded on the linear system theory and Lyapunov stability theory, relies on the capacity of the complex power system to be linearized around a stable operating point [44]. This method has been extensively used for power system stability studies involving low-frequency oscillations and sub-synchronous torsional interactions. A state-space representa-

1.1. Background

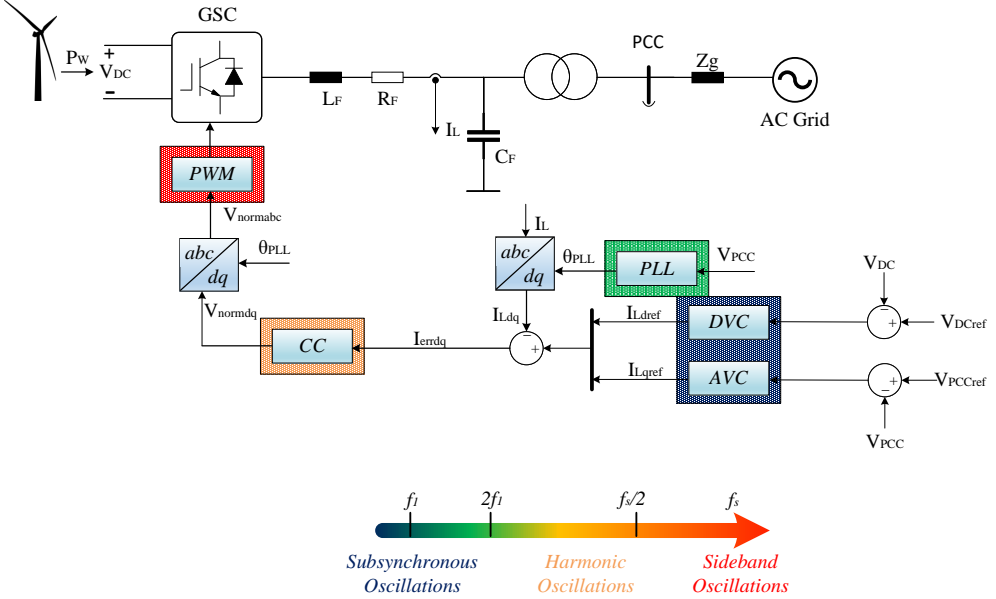


Fig. 1.12: Multiple-timescale control system of an aggregated grid-side VSC with grid-following control using a PLL.

tion provides a comprehensive analysis of the system dynamics, where it is used to perform eigenvalue analysis. This analysis is typically conducted around an equilibrium point where the nonlinear model is linearized, and the stability analysis is carried out by observing the state matrix's eigenvalues [46]. Moreover, utilizing state matrix eigenvector and participation factor analysis enables the identification of grid components or converters that are contributing to instability or resonance issues. This facilitates the determination of appropriate control parameters or modifications to grid or filter design that can effectively address such problems [47].

Impedance-based analysis is another popular method used to address the small-signal stability of interconnected converter systems in the frequency domain [48, 49]. In this approach, the system is divided into two subsystems at the PCC, and then the ratio of the subsystems' impedances is used as the open-loop gain of the entire system. The system dynamics can be evaluated based on the Nyquist Stability Criterion (NSC) through this open-loop [50]. Stability

can also be evaluated by obtaining the Bode plot from the ratio of the system's impedances, and then monitoring the stability margins [46]. One of the key advantages in impedance-based analysis is the possibility of black-box modeling of converters, allowing for the prediction of system dynamics without prior knowledge of system parameters. Furthermore, the impedance-based method predicts the system stability at the converters' terminals, enabling the identification of each converter's contribution to system stability [23].

Each of the aforementioned principal stability analysis methods is capable of effectively determining the stability of the system. A weakness of the impedance-based method is that it could potentially lead to inaccurate stability predictions when there are Right Half-Plane (RHP) poles hidden in the measured or estimated impedances [51]. Given that it cannot predict the stability of the entire system from a specific interfacing point, examining the stability at various interfacing points becomes necessary [52]. On the other hand, a main disadvantage of the eigenvalue-based method is its inability to predict sustained harmonic oscillations in VSC based HVDC systems caused by pulse-width modulation (PWM) switching [52].

As the eigenvalue-based analysis allows for the assessment of the stability of the entire system at a given operating point, this methodology is favored in the research undertaken in this thesis. Alternative methods of small-signal stability include harmonic state-space modeling and passivity-based stability analysis. Harmonic state-space modeling is employed in three-phase unbalanced systems to delineate the interactions of multiple frequency components [53]. Passivity-based analysis extends the concepts of impedance-based modeling method, aiming to quantify the converter impedance with a passivity index, verifying whether the system maintains stability or not [47].

Time domain analysis for stability studies is a useful complement to the small-signal analysis techniques previously discussed, as it considers the large-signal non-linear dynamics of different elements. Given the frequency range of interest, time domain stability analysis should be based on electromagnetic transient (EMT) and/or real-time simulation techniques [46]. EMT tools are particularly advantageous as they allow for the incorporation of actual controls and consider all control and element non-linearities. This is crucial as converter non-linearities and realistic delays may significantly impact dynamic oscillations [54]. Beyond their direct use in stability analysis, EMT tools can also serve as a validation method for instabilities identified with small-signal stability tools.

1.1. Background

1.1.4 State-of-the-art in Small-Signal Modelling with Grid-Following Control

Recent years have seen extensive research in the field of small-signal modeling, predominantly using the state-space approach. The state-space model for a grid-connected inverter, incorporating proportional-integral (PI) controllers and Park's transformation, is constructed and analyzed in [55]. However, this model does not linearize the system around equilibrium points, nor does it provide eigenvalue analysis. In [52, 56–60], the eigenvalue trajectories for the system are presented, indicating a linearization of the state-space model. It is to be noted, though, that in [52, 56–59] the inclusion of a digital time delay is overlooked, while [60] does not explore the dynamics of the PLL coupling to the grid. In [61], the time delay is approached using a 1st order Padé approximation, but according to [62], a 3rd order approximation would yield more precision. Thus, there is a clear need for an analytical approach to state-space modeling that contains PLL dynamics and time delay to perform stability analysis accurately in both low and high frequency ranges. Addressing this need forms the 1st research objective of the thesis outlined in subsection 1.2.

Additionally, the influence of outer-loop controllers like DVC and AVC on small-signal stability has been a focus area for many researchers, as incorporated in the studies cited above. The AVC controller's effect is integrated into the impedance-based model in [63, 64]. As documented in [29, 65], various state-space modeling techniques for converter-based systems have been investigated, with an emphasis on modularity and the inclusion of outer-loop control dynamics. Moreover, the AVC's effect is included in the state-space model derived from the VSC output voltage transfer function in [66]. Models in [67–69] also incorporate the AVC controller. However, the stability impact of the AVC controller's design has not been studied in depth, indicating an area that demands further investigation. This area of needed research forms the basis of the thesis 2nd research objective, as detailed in subsection 1.2.

Lastly, a modular methodology has been employed in [59, 65] to design models of systems with multiple VSCs, reflecting a higher complexity. Nonetheless, the first case employs an L filter, and the second overlooks the PLL dynamics. A Component Connection Method (CCM) offers an alternative representation for multi-VSC systems, as thoroughly explored in [60, 70]. Yet, this method faces challenges with depicting the internal connections due to control couplings as indicated in [62]. Therefore, a comprehensive modular methodology that incor-

porates all control dynamics and system complexities, including filter capacitance and PLL dynamics, is essential. The development and stability analysis of such a comprehensive model represent the 3rd research objective, as presented in subsection 1.2.

1.1.5 Mitigating of Sub-synchronous Oscillations in Wind Farms

As detailed in subsection 1.1.2, the stability driven by converters and the stability due to resonance are closely linked with SSOs in wind farms, which can be influenced by the low strength of the grid, the SCR and the PLL parameters, as well as the rapidly-acting control devices that interact with turbine generators, such as STATCOMs and SVCs. While SSOs were initially observed in conventional power systems in the 70s—with the mechanisms of oscillation and mitigation techniques well-documented since then [71]—the interest in researching SSOs within wind farms has been increased in the last 15 years. This is attributed to an incident in 2009 involving a sustained oscillation phenomenon in Texas’s Southern power grid, where the oscillation frequency (20 Hz) was significantly lower than the synchronous frequency. This incident was triggered by a line fault leading to a radial connection of a wind farm to a 50% series compensated line. A similar oscillatory incident occurred in the Buffalo Ridge area of Minnesota due to analogous reasons [72, 73]. Hence, the examination and analysis of SSOs in wind farms, coupled with the investigation of mitigation strategies, have emerged as crucial topics for the system’s stability in recent years.

Several strategies have been proposed and implemented to mitigate these phenomena. These strategies can be classified into two main categories: control/software solutions and hardware solutions, as illustrated in Fig. 1.13, and they can be implemented in DFIG (Type-3) and PMSG (Type-4) systems [74].

Software Solutions

The software solutions for mitigating SSOs include the adjustment of converter controller parameters, the application of digital filters [75–78], and the deployment of virtual synchronous generator (VSG) concepts [73, 79, 80] and direct power control (DPC) concepts [81] based on grid-forming control. Typically, the PLL parameters, as well as the MSC control and GSC control parameters of the wind turbine, are tuned to reduce the effects of SSOs.

1.1. Background

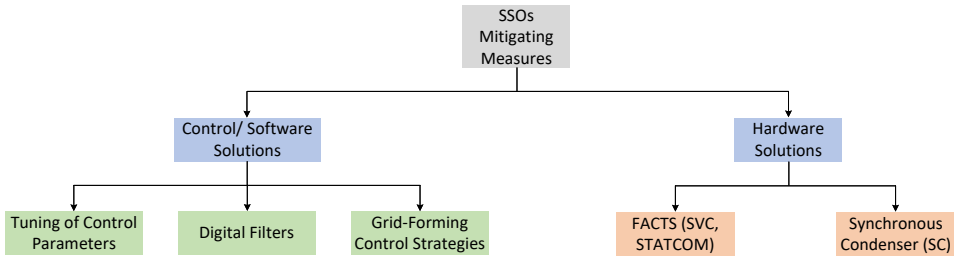


Fig. 1.13: Mitigating Measures of Subsynchronous Oscillations (SSOs) [74].

Specifically, the modification of PLL control parameters is a commonly used strategy to alleviate subsynchronous oscillations induced by converter instability, as highlighted in section 1.1.2. The PLL's parameters have been found to significantly affect the stability of both DFIG systems [82] and PMSG systems [28]. Nevertheless, such tuning might not fully meet other requirements such as fast Fault Ride-Through (FRT) capability and power quality, which the controllers were originally designed for without considering SSOs [74]. As such, several constraints must be considered when adjusting converter controllers' parameters in modern power grids [74].

Digital filters are employed mainly in DFIG systems to prevent subsynchronous currents from flowing through the rotor, thereby avoiding the development of negative resistances. For electrical resonance, a 2^{nd} order Notch filter has been commonly used [76]. However, these filters are typically calibrated for a fixed frequency, while the frequency at which SSR occurs can fluctuate depending on the operating conditions. This variability limits their effectiveness, explaining why Notch filters are not widely used for SSO mitigation [74].

Concerning grid-forming control strategies for SSO mitigation, the VSG is a viable option for PMSG systems [83] and DFIG systems [79]. In fact, it does not rely on PLL, thus reducing the risk of converter-driven instability. However, the performance of VSG for MSC may be inferior to vector control because it regulates the current transients through a current limiter, while vector control manages them through MSC's current control, resulting in improved transient performance [84]. On the contrary, DPC has demonstrated effective performance in mitigating electrical resonance in DFIG systems, as it decreases the DFIG's equivalent resistance, leading to less negative damping in the subsynchronous frequency range. Yet, there is limited research on the implementation of DPC in

stability analysis studies for complex systems, as most research has been focused on single-machine infinite bus systems [81].

Hardware Solutions

Hardware strategies for mitigating SSOs typically involve the integration of additional equipment into the grid of the system operator [73]. These solutions often rely on FACTS devices. Various FACTS devices, including SVC, Thyristor Controlled Series Capacitors (TCSC) and STATCOM, have been deployed to mitigate electrical resonance instability e.g. caused by the DFIG control system. [85].

The primary function of SVC is to ensure voltage support and restrain SSR [86]. However, TCSC is generally considered more effective than SVC in suppression, given its ability to operate in distinct areas by modulating its firing angle. Notably, TCSC is a series device, while SVC is a shunt device, and the series device has proven to be more successful in mitigating SSR induced by DFIG.

On the other hand, STATCOM includes functions such as reactive power control, voltage regulation, and SSR mitigation [87–89]. A STATCOM equipped with a simple voltage regulator at the terminals of wind farms can successfully dampen the induction generator effect in DFIG systems even without the need for other specific controls. Moreover, when installed at the PCC, a STATCOM featuring a controller for phase angle and modulation index can help to mitigate the potential risk of SSR in DFIG and PMSG systems under both steady state and fault conditions.

However, a significant drawback of FACTS-based solutions is the substantial capital investment required. SVC and STATCOM may be feasible solutions if additional system services such as voltage support are required along with SSR mitigation. Alternatively, in other cases, more cost-effective solutions may be more suitable.

Another hardware approach that has attracted substantial research interest is the Synchronous Condenser (SC) [90–93]. Compared to FACTS devices, SCs offer several advantages. They have been gaining increasing popularity due to their capacity to control voltage, inject reactive power, and provide system inertia simultaneously [94, 95]. SCs are synchronous machines that do not generate electric power but spin freely without a prime mover. By adjusting their field voltage, SCs can regulate their reactive power exchange with the grid, thus re-

1.2. Thesis Motivation and Research Tasks

enforcing the network to which they are connected [96]. Specifically, when an SC is connected to the grid, the equivalent impedance from the PCC's perspective decreases, which can impact system stability, a benefit that a STATCOM without an additional damping controller may not provide. SCs can enhance system damping in DFIG and PMSG based systems. Furthermore, unlike other mitigation measures, SCs can mitigate SSO without the need for upgrades or additional damping controllers [97].

1.1.6 State-of-the-art in Mitigation of SSOs with a Synchronous Condenser

Multiple studies have been conducted on the role of SCs as a mitigating measure for SSOs. In [98], the study focuses on the impact of a SC in a photovoltaic power plant, particularly examining its stability effects during voltage dips. The benefits of SCs have been emphasized over other hardware solutions such as STATCOM and SVC, with this comparison discussed in [97,99,100]. The work in [101,102] examines the combined effects of control strategies in converter-based power systems utilizing SCs. The optimization of SC allocation in the power grid and the related cost and sizing considerations have been explored in [96,103–105]. A notable real-world application of SCs in the Australian power system is documented in [106], where their deployment significantly mitigated SSOs and enhanced the integration of renewable energy sources. Nevertheless, existing studies have not concentrated on different SC's power ratings and their impact on the mitigation of existing SSOs issues without introducing new dynamics post-implementation. This identified need for further inquiry formulates the 3rd research objective of the thesis, as detailed in subsection 1.2.

1.2 Thesis Motivation and Research Tasks

As highlighted in previous sections, the increased integration of wind power into the primary power grid could potentially lead to stability issues, and there are many examples. Consequently, it is essential to first develop accurate models capable of conducting stability analysis studies before the installation of a wind power plant begins. This research field has drawn attention from both academy and industry the last ten years, the latter keen on ensuring a safe integration of wind power plants into the grid in order to limit the risk. Key industry stake-

holders include wind farm developers, wind turbine manufacturers, and Transmission System Operators (TSOs) in regions where the wind power technology is implemented.

Accurate small-signal modeling could provide insights into the impact of certain conditions on the stable operation of a wind turbine in a wind farm, such as the grid strength. Additionally, the design of the outer loop AVC controller is a factor that could significantly influence the system's stability, a detail which can be examined through small-signal modeling. Beyond tuning the control parameters of the wind turbine to maintain a stable system operation, incorporating a synchronous condenser into the initial wind farm's small-signal model can further offer valuable conclusions about mitigating potential oscillations.

In alignment with the research motivation described earlier, the following research gaps have been identified.

- There is a need for accurate small-signal models of a grid-connected wind turbine. The model's accuracy is vital to study the sensitivity to operating conditions and grid specifications. Here, it is essential to define the range of stable operation under steady-state conditions accurately.
- Further exploration is required to understand the impact of the AVC design on the stability of the wind turbine. An optimal tuning and design of this controller can help to maintain grid stability at the PCC, highlighting its significance.
- For cases of unstable operation in large wind farms, particularly in weak grid scenarios, the introduction of a synchronous condenser as a mitigation measure is a promising solution. Further examination is needed to understand the impact of the synchronous condenser's rating to mitigate unwanted oscillations in the wind farm.

This project aims to provide further insights into these areas.

1.2.1 Research Questions and Objectives

According to the previously defined research gaps, this Ph.D. projects aims to look into the modeling of wind turbines connected to the grid, where the root cause of possible converter-driven and resonance stability issues will be explained and studied. For that purpose, the following research question is formulated.

1.2. Thesis Motivation and Research Tasks

“How can wind turbines be modeled and analyzed in order to accurately characterize their interactions with the grid under small-signal disturbances, and how could mitigating measures be included in larger wind farm systems?”

This general research question can be split into the following research sub-questions.

- What type of sub-models could a wind turbine model include, in order to accurately determine the instabilities in the low and high frequency range?
- How does the grid-following control behave for different levels of grid strength in wind turbine systems?
- How does the design of the AVC controller in grid-following converter control affect the system’s stability in accordance with the grid strength?
- Under which conditions can a synchronous condenser effectively mitigate SSOs in wind farms?

To answer the aforementioned research questions, the following research objectives of the Ph.D. are identified:

Analyzing the sensitivity of controllers’ designs in a wind turbine’s model using grid-following control under different grid strengths

It is critical to explore the dynamics of the current controller and understand how they are affected by variations in the SCR, which determines the grid strength. Moreover, a state-space model should be capable of identifying the PLL dynamics e.g. under weak grid conditions. Time-domain simulations can serve as a primary tool for validating instabilities identified in the eigenvalue-based stability analysis of the small-signal model.

Evaluating the stability impact of the AVC controller’s design on converter-based systems

The design of the AVC control can significantly influence a wind turbine’s stability as it alters the bandwidths of AVC as well as PLL, potentially leading to instabilities. Thus, it is necessary to examine the impact of these controllers

on the wind turbine's model and validate it in accordance with grid strength to derive useful conclusions.

Analyzing a multi-VSC small-signal model of wind turbines in order to assess the stability impact of its control design

Having investigated the stability influence within a system utilizing a single VSC of a wind turbine, advancing the study to systems incorporating multiple VSCs becomes important. Consequently, a comprehensive small-signal model for multi-VSC systems needs to be formulated, capable of accurately portraying the dynamics of controllers in both the low and high frequency ranges.

Assessing the stability impact of a synchronous condenser in wind farms during the occurrence of SSOs

In situations where SSOs are detected in small-signal models of wind farms, a synchronous condenser is a known solution to provide the necessary voltage stability. However, further research is needed to determine the appropriate power rating of a synchronous condenser under such conditions. Furthermore, potential issues that might arise from the use of an unsuitable synchronous condenser need to be identified. The foundation for this analysis can be a small-signal model of the wind farm.

1.2.2 Project Limitations

Considering the complexity of power systems with wind power penetration, the following assumptions and simplifications have been adopted.

- The MSC control of the wind turbine's converter system is considered as a constant dc source with a controllable current controller.
- The anti-paralleled diodes and the switches of the inverter are treated as ideal components.
- The external network seen from the grid-connected converter is represented as a simple Thevenin equivalent.
- Grid-following converter control is utilized for formulating the control structure of the GSC.

1.3. Thesis Outline

- State-space modeling is preferred for the stability analysis studies in this work, as it can predict the entire system's stability; other stability analysis methods are not utilized.
- In both Chapter 2 and Chapter 3, we conduct simulations on a scaled-down system, with a power level significantly lower than that of a realistic wind turbine system.
- In Chapter 4, aggregated modeling is implemented in order to represent the wind turbines that formulate the offshore wind farm under study.
- The dynamical study of the wind farm in Chapter 4 is solely focused on HVAC interconnections. HVDC interconnections are not examined in this analysis.

1.3 Thesis Outline

The outcomes of the Ph.D. project are summarized in this thesis based on authored and published papers during the study. The thesis is structured in two parts: the report and the associated publications. The report contains a concise overview of the primary research conducted in this project, whereas the chosen publications feature the outcomes of the papers published during this Ph.D. study. Fig. 1.14 visually demonstrates the layout of the thesis, indicating the connection between each chapter and the selected publications.

The report is organized into 5 main chapters. Chapter 1 gives the introduction to the Ph.D. study, by discussing on the background and presenting the main motivations of the conducted research.

Chapter 2 presents the small-signal model of a wind turbine, focusing on the grid-connected VSC part. It provides a thorough description of the developed state-space model, and studies the system's stability for different cases of grid strength, in order to assess the proposed model's accuracy.

Chapter 3 focuses on the outer loop control of the wind turbine's small signal model, aiming to stress out the impact of the AVC controller design on the system's lower frequency instability, again in accordance with the grid strength as well as the PLL. It also provides a stability assessment of a multi-VSC model, with a control structure based on the one previously discussed, where each VSC submodel corresponds to a wind turbine in a wind farm.

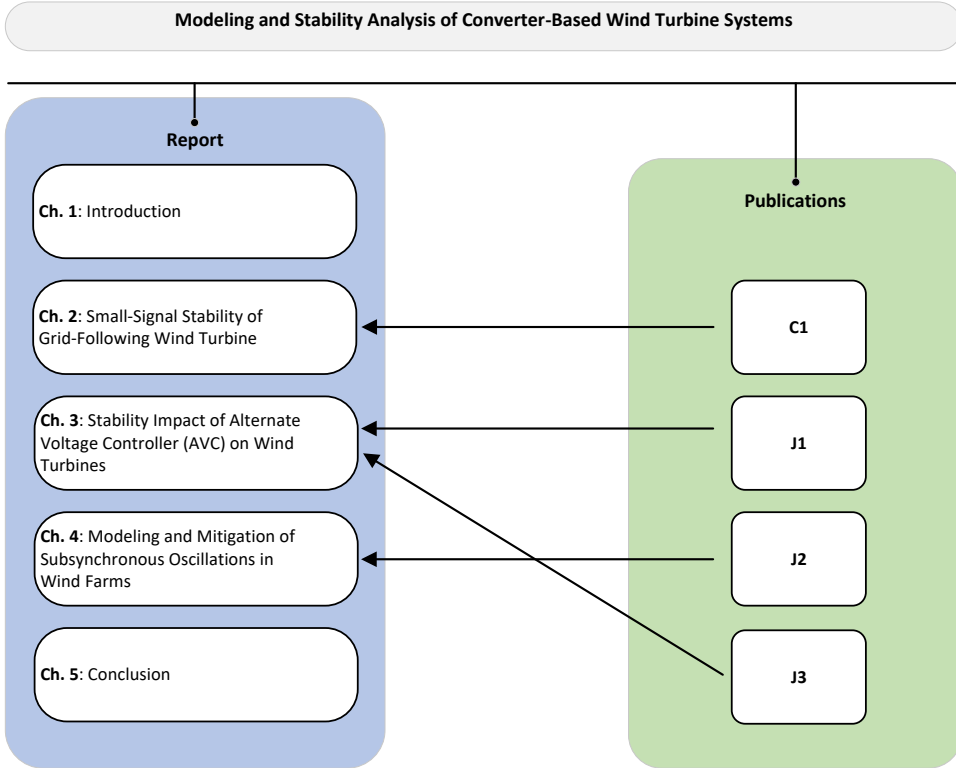


Fig. 1.14: Thesis layout and the correlation between the report and corresponding publications.

Chapter 4 moves on to the wind farm level and discusses the mitigation of SSOs that may arise in a wind farm; the main focus is on the modeling and inclusion of a synchronous condenser in the wind farm as a key mitigating method of those oscillations.

Finally, Chapter 5 summarizes the main contributions of this Ph.D. study and suggests some research perspectives to be studied in the future.

1.4 List of Publications

The outcomes of the project have been disseminated in various forms, including journal and conference papers. The publications are shown in Fig. 1.14 in relation with the thesis, and the full list is given below.

Publication in refereed journals:

- [J1] **D. Dimitropoulos**, X. Wang and F. Blaabjerg, “Stability Impacts of an Alternate Voltage Controller (AVC) on Wind Turbines with Different Grid Strengths,” *Energies*, vol. 16, no. 3, 2023, Art. no. 1440.
- [J2] **D. Dimitropoulos**, M. K. Bakhshizadeh, L. Kocewiak, X. Wang and F. Blaabjerg, “Impact of Synchronous Condenser’s Rating on Mitigating Subsynchronous Oscillations in Wind Farms,” submitted to *IEEE Access*.
- [J3] **D. Dimitropoulos**, X. Wang and F. Blaabjerg, “Stability Analysis in Multi Voltage-Source Converter Systems of Wind Turbines,” submitted to *Elsevier’s e-Prime - Advances in Electrical Engineering, Electronics and Energy*.

Publication in refereed conferences:

- [C1] **D. Dimitropoulos**, X. Wang and F. Blaabjerg, “Small-Signal Stability Analysis of Grid-Connected Converter under Different Grid Strength Cases,” in *Proc. 2022 IEEE 13th International Symposium on Power Electronics for Distributed Generation Systems (PEDG)*, Kiel, Germany, 2022, pp. 1-6.

Chapter 2

Small-Signal Stability of Grid-Following Wind Turbine

2.1 Background

In Chapter 1, the importance of small-signal modeling was highlighted, as it enables the development of a comprehensive state-space model of the overall system. State-space modeling plays a key role in assessing the robustness and understanding the dynamic phenomena induced by the system's control structures [45]. The focus of this chapter is the development and study of a linearized small-signal model of a VSC connected to the grid via an LC filter. The model considers the dynamic interactions between the PLL and the grid, while also accommodating the impact of time delay in the control loop. Furthermore, an emphasis is placed on how the stability of the small-signal model is sensitive to control gain variations of the inner current control loop and the PLL across different grid strength scenarios. The accuracy and effectiveness of this analysis are supported by both time-domain simulations and frequency-domain analysis using Fast-Fourier Transformation (FFT) analysis.

2.2. State-Space Modeling of Wind Turbines Grid-Side Control

state-space models of the system components.

$$\begin{aligned}\dot{x} &= Ax + R(x, u) \\ y &= S(x, u)\end{aligned}\tag{2.1}$$

The control system architecture under consideration in this work is graphically represented in Fig. 2.1. The structure involves a grid-following converter employing vector current control (CC). Synchronization between the converter and the grid is accomplished via a PLL. The active and reactive power levels, used to calculate the reference converter current (I_{Ldref} in d-axis and I_{Lqref} in q-axis), are regulated to align with their respective active and reactive reference values (P_{ref} and Q_{ref} respectively) through open-loop control. This approach proves adequate as the operation of an ideal converter is assumed. Additionally, a stable DC link voltage V_{DC} is assumed to be provided to the inverter in this context, as the response time of the inner control loop of the current is much faster than the outer loop of the voltage. In practice, however, the DC link voltage is determined from the power balance between the MSC and the GSC of the wind turbine. The dc-link voltage must be regulated to control the power flow and also improve the quality of the ac-side current.

2.2.1 dq - Transformation

In this model, the control system operates in the rotating dq frame, oriented in relation to the PCC voltage phase angle, denoted as θ_1 . Simultaneously, the control system is governed by the PLL output angle θ_{PLL} . Under dynamic conditions, the divergence between these two angles remains insignificant [49].

To provide clarity on the dynamics introduced by the PLL, two dq frames are defined: the grid dq frame, defined by θ_1 , and the control dq frame, defined by θ_{PLL} . During stable operation, the PLL accurately traces the grid voltage angle, resulting in a synchronized alignment of the control dq frame with the grid dq frame [J1]. However, any perturbations in the grid voltage will induce a phase shift, $\Delta\theta$, between the two reference frames. This shift necessitates a period for the PLL to adjust and align with the new grid voltage angle [107].

The converter's current I_L and the PCC voltage V_{PCC} are output variables influenced by the control dq frame. In the following subsections of the chapter, when these variables are represented in the control dq frame, they will be indicated by a superscript c , as in [C1] and [J1]. The subscript θ signifies steady-

state values of the associated variables. The relationship between the two dq frames is illustrated in Fig. 2.2.

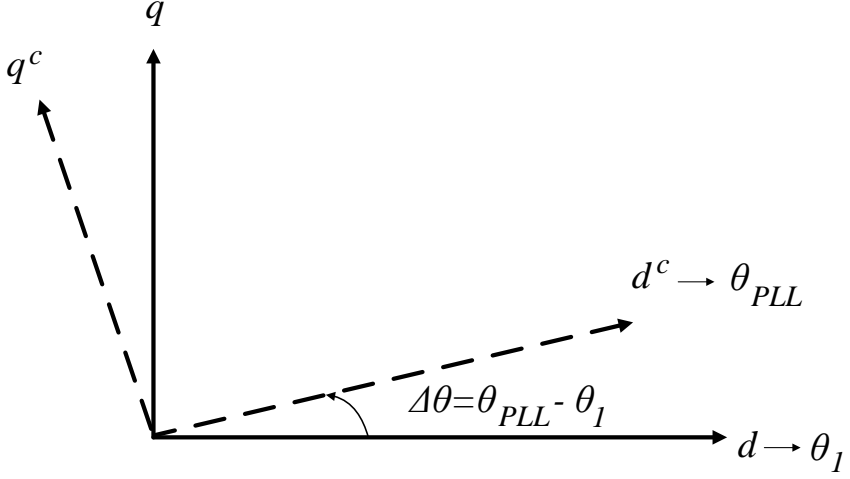


Fig. 2.2: Control (θ_{PLL}) and grid (θ_1) dq frame used for the voltage-source converter. Source: [J1].

The transformation equations between the control and the grid dq frame derived from the Park and inverse Park transformation equations, and they are outlined below:

$$\begin{bmatrix} V_{PCCd}^c \\ V_{PCCq}^c \end{bmatrix} = \begin{bmatrix} \cos(\theta_{PLL} - \theta_1) & \sin(\theta_{PLL} - \theta_1) \\ -\sin(\theta_{PLL} - \theta_1) & \cos(\theta_{PLL} - \theta_1) \end{bmatrix} \begin{bmatrix} V_{PCCd} \\ V_{PCCq} \end{bmatrix} \quad (2.2)$$

$$\begin{bmatrix} I_{Ld}^c \\ I_{Lq}^c \end{bmatrix} = \begin{bmatrix} \cos(\theta_{PLL} - \theta_1) & \sin(\theta_{PLL} - \theta_1) \\ -\sin(\theta_{PLL} - \theta_1) & \cos(\theta_{PLL} - \theta_1) \end{bmatrix} \begin{bmatrix} I_{Ld} \\ I_{Lq} \end{bmatrix} \quad (2.3)$$

Following the linearization of the transformation equations between the two dq frames, the small-signal equations are given as:

$$\Delta V_{PCCd}^c = \Delta V_{PCCd} + V_{PCCq,0} \Delta\theta \quad (2.4)$$

$$\Delta V_{PCCq}^c = \Delta V_{PCCq} - V_{PCCd,0} \Delta\theta \quad (2.5)$$

2.2. State-Space Modeling of Wind Turbines Grid-Side Control

$$\Delta I_{Ld}^c = \Delta I_{Ld} + I_{Lq,0} \Delta \theta \quad (2.6)$$

$$\Delta I_{Lq}^c = \Delta I_{Lq} - I_{Ld,0} \Delta \theta \quad (2.7)$$

2.2.2 Phase-Locked Loop (PLL) and its Design

The control architecture of the PLL is depicted in Fig. 2.3. The q-axis component voltage V_{PCCq} at the PCC is utilized as the input to the PLL, and the PI controller generates the angular speed of the PCC voltage, referred to as ω_{PLL} . The PI controller effectively neutralizes the voltage V_{PCCq} , thereby ensuring the alignment of the PCC voltage with the d-axis.

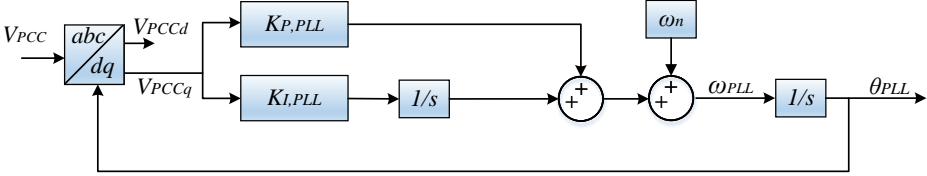


Fig. 2.3: Control structure of the used PLL shown in Fig. 2.1. Source: [C1].

The state variables of the PLL are:

$$x_{PLL} = \begin{bmatrix} \theta_{PLL} & \Phi_{PLL} \end{bmatrix} \quad (2.8)$$

where $\Phi_{PLL} = \int V_{PCCq}^c dt$.

The differential equations of the PLL are the following:

$$\dot{\theta}_{PLL} = K_{I,PLL} \Phi_{PLL} + K_{P,PLL} V_{PCCq}^c + \omega_n \quad (2.9)$$

$$\dot{\Phi}_{PLL} = V_{PCCq}^c \quad (2.10)$$

where ω_n is the system's nominal angular frequency.

Design of PLL

As mentioned in 2.2.1, the PLL estimates the PCC phase voltage angle, and the divergence between the converter and the grid dq frame results in the phase

error $\Delta\theta$. Linearization can be implemented when $\Delta\theta$ is very small, and the closed-loop transfer function of the PLL, based on the PLL block diagram representation in Fig. 2.4 that explains the phase error, is given as:

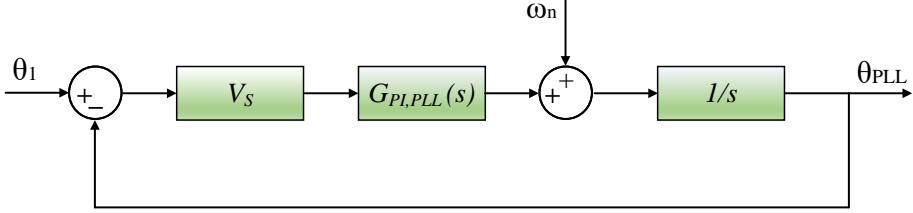


Fig. 2.4: Block diagram of the PLL control loop used for the PLL's design.

$$G_{cl,PLL}^d(s) = \frac{\theta_1(s)}{\theta_{PLL}(s)} = \frac{G_{ol,PLL}^d(s)}{1 + G_{ol,PLL}^d(s)} = \frac{V_S K_{P,PLL} s + V_S K_{I,PLL}}{s^2 + V_S K_{P,PLL} s + V_S K_{I,PLL}} \quad (2.11)$$

where V_S represents the nominal voltage of the grid, and $G_{ol,PLL}^d$ is the open-loop transfer function of the PLL.

A normalized way of expressing the 2nd order closed-loop transfer function is:

$$G_{cl,PLL}^d(s) = \frac{2\zeta_{PLL}\omega_{N,PLL}s + \omega_{N,PLL}^2}{s^2 + 2\zeta_{PLL}\omega_{N,PLL}s + \omega_{N,PLL}^2} \quad (2.12)$$

where ζ_{PLL} is the damping ratio and $\omega_{N,PLL}$ is the natural angular frequency. The relationship between $\omega_{N,PLL}$ and the rise time $t_{r,PLL}$ is approximated as:

$$\omega_{N,PLL} = \frac{1.8}{t_{r,PLL}} \quad (2.13)$$

and the PLL control parameters can be tuned as shown below:

2.2. State-Space Modeling of Wind Turbines Grid-Side Control

$$K_{P,PLL} = \frac{2\zeta_{PLL}\omega_{N,PLL}}{V_S} \quad (2.14)$$

$$K_{I,PLL} = \frac{\omega_{N,PLL}^2}{V_S} \quad (2.15)$$

In the following sections and chapters of this thesis, the selected rise time is equal to 50 ms, and the 2nd order system of the PLL is optimally damped (i.e. with a 5% overshoot), which lead to $\zeta_{PLL}=0.707$.

2.2.3 Current Controllers (CC) and their Design

The current control loop, depicted in Fig. 2.5, together with the feedforward voltage, is responsible for the regulation of the converter's output current. This is achieved by formulating a proper reference for the output voltage. From Fig. 2.5, the following equations regarding the output of the current controllers in the dq axis can be obtained as:

$$V_{\text{normd}} = \frac{1}{V_{\text{DC}}} \left(V_{\text{PCCd}} - \omega_{\text{PLL}} L_F I_{Lq}^c + K_{P,d} I_{\text{errd}} + K_{I,d} q_{\text{errd}} \right) \quad (2.16)$$

$$V_{\text{normq}} = \frac{1}{V_{\text{DC}}} \left(V_{\text{PCCq}} + \omega_{\text{PLL}} L_F I_{Ld}^c + K_{P,q} I_{\text{errq}} + K_{I,q} q_{\text{errq}} \right) \quad (2.17)$$

where q_{errdq} corresponds to the integrators of the current controllers, and L_F is the filter inductance.

In the vector current control scheme, the converter current can be limited and the control performance can be improved by the decoupling control in the d-q coordinate system [108]. The error current I_{errdq} is calculated by taking the difference between the d- and q-axis current references and the converter's measured currents. The reference currents to the d- and q-axis are derived based on the specified active and reactive power references, which constitute the operating point of the system, and they are described in the following equations.

$$I_{Ld\text{ref}} = \frac{P_{\text{ref}}}{1.5V_S} \quad (2.18)$$

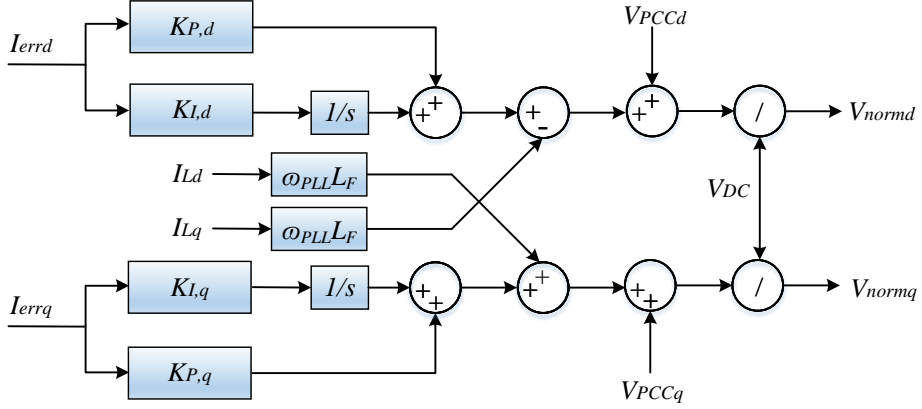


Fig. 2.5: Control structure of the current controller (CC) in Fig. 2.1. Source: [C1].

$$I_{Lqref} = -\frac{Q_{ref}}{1.5V_S} \quad (2.19)$$

The state variables of the current controller are:

$$x_{CC} = \begin{bmatrix} q_{errd} & q_{errq} \end{bmatrix} \quad (2.20)$$

The differential equations of the current controller are the following:

$$\dot{q}_{errd} = I_{Ldref} - I_{Ld}^c \quad (2.21)$$

$$\dot{q}_{errq} = I_{Lqref} - I_{Lq}^c \quad (2.22)$$

Design of Current Controllers

The d- and q-axis component of the inner current control loop have the same dynamics. Therefore, the design procedure of only the d-component in the inner current control loop can be utilized, and it is depicted in Fig. 2.6.

In Fig. 2.6, $G_{PI}^d(s)$ represents the d-component of the PI current controller, $G_{delay}(s)$ the time delay and $G_F(s)$ the filter (plant) transfer function. The filter capacitance C_F (shown in Fig. 2.1) deals only with the switching ripple frequencies and can be neglected in this analysis, as the inverter model with an

2.2. State-Space Modeling of Wind Turbines Grid-Side Control

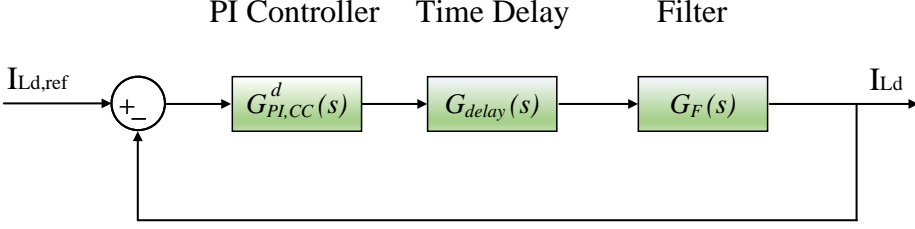


Fig. 2.6: Block diagram of current control loops in the d- reference frame.

LCL filter is the same with the model with an L-filter at frequencies lower than half of the resonance frequency of the filter [18]. The transfer functions of the current control loops are shown below:

$$G_{PI,CC}^d(s) = K_{P,d} + \frac{K_{I,d}}{s} \quad (2.23)$$

$$G_{delay}(s) = \frac{1}{1 + 1.5T_S s} \quad (2.24)$$

$$G_F(s) = \frac{1}{R_F + L_F s} \quad (2.25)$$

where T_S is the sampling period.

According to Fig. 2.6, the cross-coupling $\omega_{PLL}L_F I_{Lq}$ and the voltage feed-forward V_{PCCd} terms for the d-axis current component control loop (which are shown in Fig. 2.5) have been neglected, as they can be considered as disturbances into the system. Therefore, the open-loop and closed-loop transfer functions can be defined:

$$G_{ol,CC}^d(s) = G_{PI,CC}^d(s)G_{delay}(s)G_F(s) = \frac{K_{P,d}T_F(1 + T_I s)}{T_I L_F s(1 + 1.5T_S s)(1 + T_F s)} \quad (2.26)$$

$$G_{cl,CC}^d(s) = \frac{G_{ol,CC}^d(s)}{1 + G_{ol,CC}^d(s)} = \frac{K_{P,d}T_F(1 + T_I s)}{T_I L_F s(1 + 1.5T_S s)(1 + T_F s) + K_{P,d}T_F(1 + T_I s)} \quad (2.27)$$

where $T_I = K_{P,d}/K_{I,d}$ is the integrator time constant and $T_F = L_F/R_F$ is the filter time constant (R_F is the filter resistance). The transfer function equations are applicable for the q-axis current, too.

In order to simplify the closed-loop transfer function, the filter time constant T_F is chosen to be equal to the integrator time constant T_I . Therefore, the closed-loop transfer function of the current control is:

$$G_{cl,CC}^d(s) = \frac{K_{P,d}}{L_F s(1 + 1.5T_S s) + K_{P,d}} = \frac{\frac{2K_{P,d}}{3T_S L_F}}{s^2 + \frac{2}{3T_S} s + \frac{2K_{P,d}}{3T_S L_F}} \quad (2.28)$$

which is a 2nd order system system, with

$$\omega_{N,CC}^2 = \frac{2K_{P,d}}{3T_S L_F} \quad (2.29)$$

$$\zeta_{CC} = \frac{1}{3T_S \omega_{N,CC}} \quad (2.30)$$

where $\omega_{N,CC}$ is the natural frequency of the system and ζ_{CC} is the damping ratio.

Choosing to have a system optimally damped leads to $\zeta_{CC} = 0.707$. Therefore, the proportional and integral gain of the current control can be expressed as:

$$K_{P,d} = \frac{L_F}{3T_S} \quad (2.31)$$

$$K_{I,d} = \frac{L_F}{3T_S T_f} \quad (2.32)$$

Therefore, in case the current controller is optimally designed, the closed-loop transfer function can be expressed as:

$$G_{cl,CC}^d(s) = \frac{1}{1 + 3T_S s} \quad (2.33)$$

and the controller's bandwidth is

2.2. State-Space Modeling of Wind Turbines Grid-Side Control

$$f_{bw,CC}^d = \frac{1}{6\pi T_S} = \frac{f_S}{20} \quad (2.34)$$

where f_S is the sampling frequency.

2.2.4 Time Delay

Time delay, a critical factor in digital control systems, is incorporated into this analysis. According to [62], the delay can be modeled using a 3^{rd} -order Padé approximation, which approximates the delay in the system by using the transfer function provided in (2.35):

$$e^{-T_d s} = \frac{(b_0 + b_1 T_d s + \dots + b_l (T_d s)^l)}{(a_0 + a_1 T_d s + \dots + a_k (T_d s)^k)} \quad (2.35)$$

where l and k are the order of Padé approximation,

$$a_j = \frac{(l+k-j)!k!}{j!(k-j)!}, j = 0, \dots, k \quad (2.36)$$

and

$$b_i = (-1)^i \frac{(l+k-i)!l!}{i!(l-i)!}, i = 0, \dots, l \quad (2.37)$$

The delay time, T_d , is typically set to be 1.5 times the sampling period T_S due to the digital implementation ($1 \cdot T_S$) and the digital modulator ($0.5 \cdot T_S$).

The state variables that describe the time delay are as follows:

$$x_{TD} = \begin{bmatrix} x_{del,1d} & x_{del,2d} & x_{del,3d} & x_{del,1q} & x_{del,2q} & x_{del,3q} \end{bmatrix} \quad (2.38)$$

The differential equations of the digital time delay, where each equation can be utilized in both the d- and q-frame, are given as:

$$\dot{x}_{del,1dq} = 0x_{del,1dq} + 1x_{del,2dq} + 0x_{del,3dq} \quad (2.39)$$

$$\dot{x}_{del,2dq} = 0x_{del,1dq} + 0x_{del,2dq} + 1x_{del,3dq} \quad (2.40)$$

$$\dot{x}_{del,3dq} = -\frac{120}{T_d^3}x_{del,1dq} - \frac{60}{T_d^2}x_{del,2dq} - \frac{12}{T_d}x_{del,3dq} + V_{normdq} \quad (2.41)$$

2.2.5 LC Filter and Grid Impedance

As depicted in Fig. 2.7, the model incorporates an LC filter, to reduce the higher order harmonics deriving from the converter, as well as the modulation harmonics. Additionally, the dynamics of the grid impedance are taken into account within the state-space subsystem, with the related state variables presented below:

$$x_{LC} = \begin{bmatrix} I_{Ld}^c & I_{Lq}^c & V_{PCCd} & V_{PCCq} & I_{od} & I_{oq} \end{bmatrix} \quad (2.42)$$

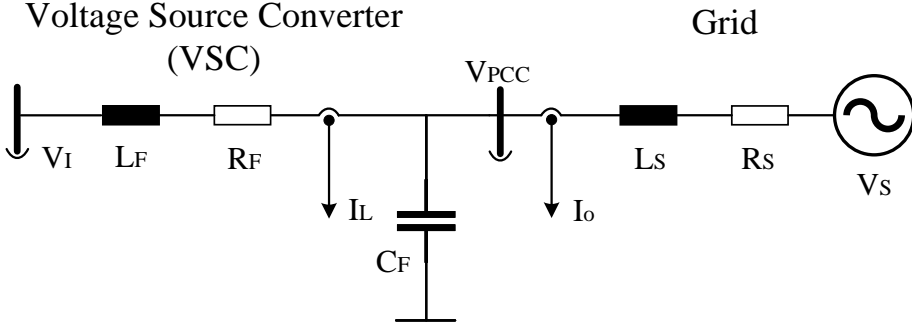


Fig. 2.7: LC filter and grid impedance circuit in Figure 2.1. Source: [J1].

The Padé approximation of the time delay is utilized to calculate the VSC bridge voltage V_I , as V_I is the output of the time-delay state-space subsystem:

$$V_{Id} = V_{DC} \left(\frac{240}{T_d^3} x_{del,1d} + 0x_{del,2d} + \frac{24}{T_d^1} x_{del,3d} - V_{normd} \right) \quad (2.43)$$

$$V_{Iq} = V_{DC} \left(\frac{240}{T_d^3} x_{del,1q} + 0x_{del,2q} + \frac{24}{T_d^1} x_{del,3q} - V_{normq} \right) \quad (2.44)$$

The state equations for the converter current I_L , the PCC voltage V_{PCC} , and the output current I_o are presented in (2.45)–(2.50):

$$\dot{I}_{Ld}^c = -\frac{R_F}{L_F} I_{Ld}^c + \left(-\frac{1}{L_F} V_{PCCd}^c \right) + \omega_{PLL} I_{Lq}^c + \frac{1}{L_F} V_{Id} \quad (2.45)$$

2.3. Grid Strength Definition and Small-Signal Stability Assessment

$$\dot{I}_{Lq}^c = -\frac{R_F}{L_F} I_{Lq}^c + \left(-\frac{1}{L_F} V_{PCCq}^c \right) - \omega_{PLL} I_{Ld}^c + \frac{1}{L_F} V_{Iq} \quad (2.46)$$

$$\dot{V}_{PCCd} = \frac{1}{C_F} I_{Ld} + \left(-\frac{1}{C_F} I_{od} \right) + \omega_n V_{PCCq} \quad (2.47)$$

$$\dot{V}_{PCCq} = \frac{1}{C_F} I_{Lq} + \left(-\frac{1}{C_F} I_{oq} \right) - \omega_n V_{PCCd} \quad (2.48)$$

$$\dot{I}_{od} = \frac{1}{L_S} V_{PCCd} + \left(-\frac{R_S}{L_S} I_{od} \right) + \left(-\frac{1}{L_S} V_{Sd} \right) + \omega_n I_{oq} \quad (2.49)$$

$$\dot{I}_{oq} = \frac{1}{L_S} V_{PCCq} + \left(-\frac{R_S}{L_S} I_{oq} \right) + \left(-\frac{1}{L_S} V_{Sq} \right) - \omega_n I_{od} \quad (2.50)$$

where R_S is the grid resistance and L_S is the grid inductance.

The final vector that includes all the state variables of the VSC system shown in (2.8), (2.20), (2.38) and (2.42), can now be defined as:

$$x = \begin{bmatrix} x_{PLL} & x_{CC} & x_{TD} & x_{LC} \end{bmatrix} \quad (2.51)$$

2.3 Grid Strength Definition and Small-Signal Stability Assessment

The stability assessment of the converter-based system begins with the identification of potential equilibrium points derived from the linearized state-space model. As described in [C1], the local stability is determined via a linear approximation of the system's state-space model represented by:

$$\dot{x} = Ax \quad (2.52)$$

Here, A signifies the Jacobian matrix entailing the partial derivatives of the system at the fixed points, which are identified by solving $\dot{x} = 0$ across all state equations of the system.

The power grid's strength is determined by the SCR, which defines the ratio of the maximum short-circuit power S_{SC} at the PCC to the rated power S_N of the VSC [C1]. The SCR can be expressed as:

$$SCR = \frac{S_{SC}}{S_N} = \frac{\frac{3}{2} \frac{(V_S)^2}{|Z_S|}}{\frac{3}{2} V_{PCC} I_{Ldref}} \quad (2.53)$$

Thus, grid impedance Z_S plays an important role in grid strength determination, as an increase in the impedance results in a decrease in short-circuit power.

An eigenvalue analysis is conducted on the small-signal model, using the system and control parameters outlined in Table 2.1. The control parameters are selected according to section 2.2; therefore, the primary goal of the default PI 's current controller is to maintain a closed loop current bandwidth approximately $1/20$ of the switching frequency, based on (2.34). A low PLL bandwidth is selected—equivalent to 11.77 Hz—to minimize potential distortion of the PLL output signals due to high-order harmonics. The selected operating point regarding the system's active and reactive power is 30 kW and 0 kVAR, respectively. The grid inductance L_S is defined by (2.53), while the grid resistance R_S is assumed to be zero for this analysis.

Table 2.1: System and Default Control Parameters of Grid-Connected Converter System. Source: [C1].

	Description	Value
V_S	Grid Phase Voltage (peak value)	311 V
f_n	Rated Frequency	50 Hz
V_{DC}	DC Link Voltage Reference	800 V
L_F	Filter Inductance	5 mH
R_F	Filter Resistance	0.1 Ω
C_F	Filter Capacitance	10 μF
f_{sw}	Switching Frequency	20 kHz
f_S	Sampling Frequency	20 kHz
P_{ref}	Nominal Active Power	30 kW
Q_{ref}	Reactive Power	0 kVAR
K_{I0}	Default Integral Gain of Current Control	666.7
K_{P0}	Default Proportional Gain of Current Control	33.3
$K_{I,PLL0}$	Default Integral Gain of PLL	4.1672
$K_{P,PLL0}$	Default Proportional Gain of PLL	0.1637

2.3. Grid Strength Definition and Small-Signal Stability Assessment

2.3.1 Stability Impact of Current Controller for Different Grid Strengths

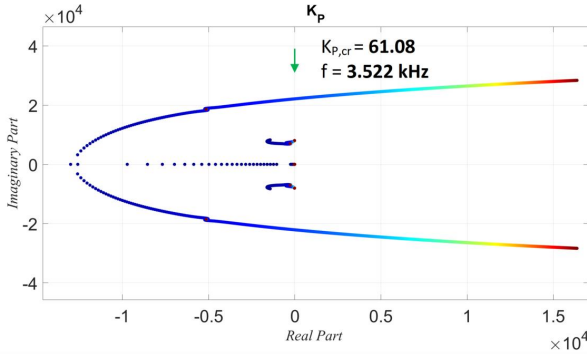
In Fig. 2.8, the eigenvalue analysis of the small-signal model is examined, where the system and current control parameters specified in Table 2.1 are used. The grid inductance L_S is defined to match a given SCR, and the grid resistance R_S is assumed to be zero. A positive real part of a complex eigenvalue, indicating a negative damping, is a sign of instability. As such, every time a parameter undergoes a change, a new eigenvalue analysis is needed, ultimately yielding an eigenvalue trajectory that represents the stability trend of the specific control parameter.

The controller gains are adjusted between 0.1 (deep blue) and 10 (deep red) times the default controller value, showcasing the pair of eigenvalues linked to system instability; the corresponding critical gain as well as the critical frequency are indicated. After observing the eigenvalue trajectories, the system appears to lose stability as the proportional gain of the current controller increases. The critical frequency is around 1/6 of the sampling frequency f_S across all simulation cases.

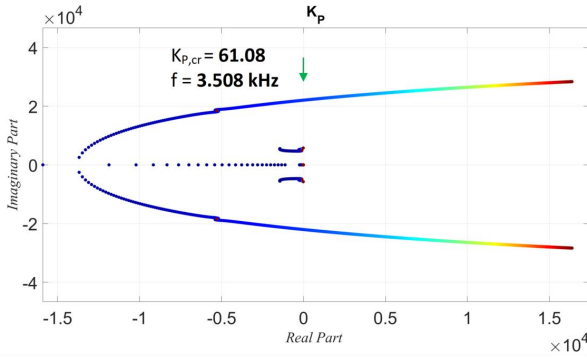
To verify the dynamic response of the small-signal model, time-domain simulations were conducted using MATLAB Simulink and PLECS Blockset. The circuit and control parameters mirrored those of the small-signal model in Table 2.1. Step changes were applied to the current control parameters at $t = 2$ seconds, while system stability was maintained. Subsequently, the controller gains adopted critical values impacting system stability, and the dq-frame inductor current I_L was used to depict the instability scenarios in Fig. 2.9. As the system approached instability, FFT analysis was conducted to identify the dominant frequency and draw a comparison with the critical frequency of the corresponding small-signal model; the corresponding simulation results are presented in Fig. 2.10. A close match was observed between these simulation outcomes and the corresponding stability analysis results of the small-signal study displayed in Fig. 2.8.

2.3.2 PLL dynamics in Weak Grid Case

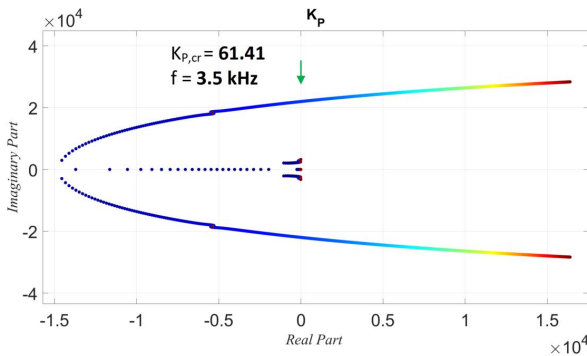
Previously, the sensitivity of the current controller's design under different grid strength scenarios was examined and validated. The weak grid case, with an SCR of 1.5, was then chosen for further analysis. For this scenario, an eigenvalue



(a) SCR equal to 10



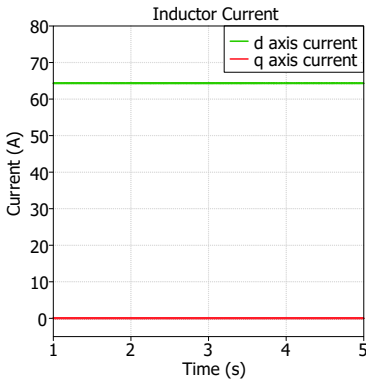
(b) SCR equal to 5



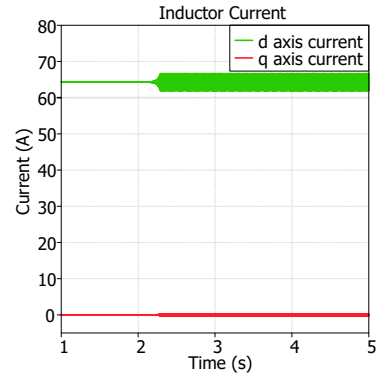
(c) SCR equal to 1.5

Fig. 2.8: Eigenvalue trajectories for variations in proportional gain of current controller (K_P) for different grid strength cases. K_P is varied from 0.1 (deep blue) to 10 (deep red) times K_{P0} . Green arrow means instability point. Source: [C1].

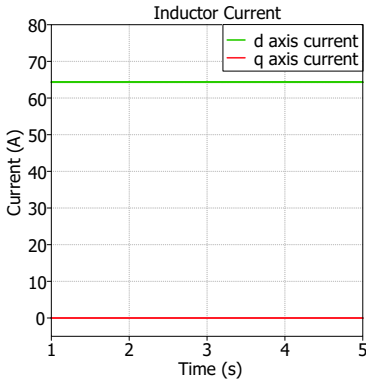
2.3. Grid Strength Definition and Small-Signal Stability Assessment



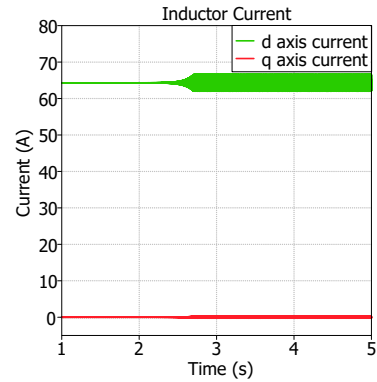
(a) SCR = 10 when $K_P = 58.27$ at $t=2$ sec. The system remains stable.



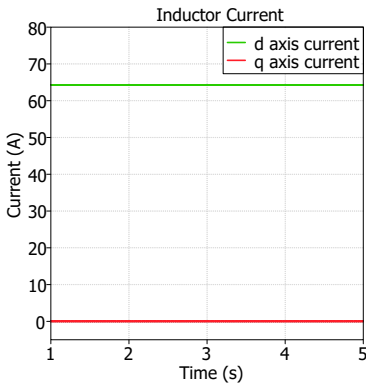
(b) SCR = 10 when $K_P = 58.61$ at $t=2$ sec. The system becomes unstable.



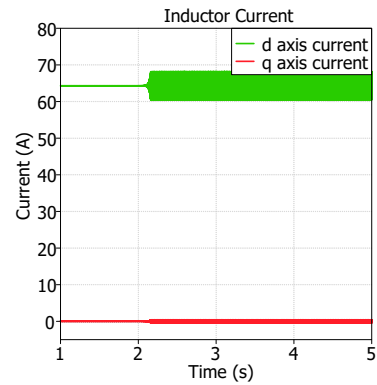
(c) SCR = 5 when $K_P = 58.27$ at $t=2$ sec. The system remains stable.



(d) SCR = 10 when $K_P = 58.61$ at $t=2$ sec. The system becomes unstable.

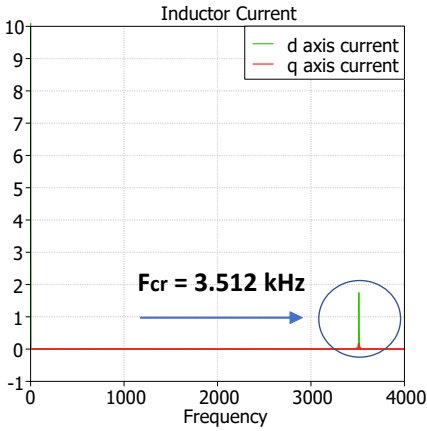


(e) SCR = 1.5 when $K_P = 58.61$ at $t=2$ sec. The system remains stable.

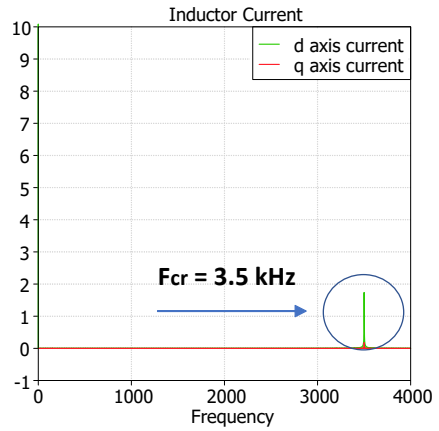


(f) SCR = 1.5 when $K_P = 58.94$ at $t=2$ sec. The system becomes unstable.

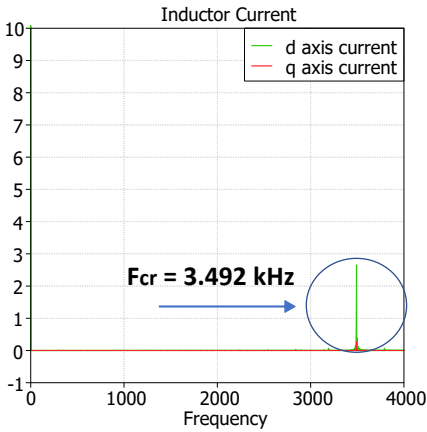
Fig. 2.9: Time-domain simulations - inductor current I_{Ld} for different grid strength cases and very small changes in K_P at $t=2$ sec. Source: [C1].



(a) SCR equal to 10 - FFT analysis



(b) SCR equal to 5 - FFT analysis



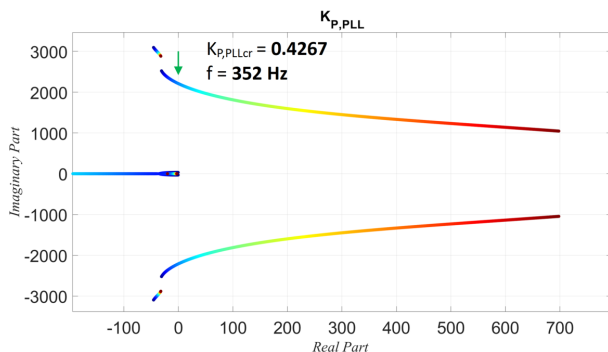
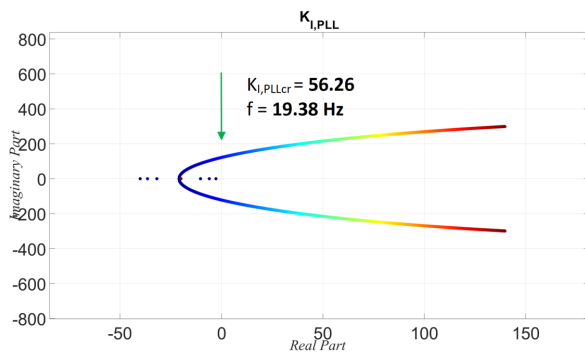
(c) SCR equal to 1.5 - FFT analysis

Fig. 2.10: Frequency analysis (FFT) of the inductor current I_{Ld} (see Fig. 2.9) when instability is observed after changes in K_P are applied at $t=2$ sec for different grid strength cases. Source: [C1].

analysis was conducted considering the parameters of the PLL control.

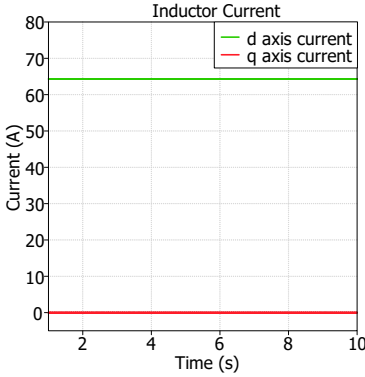
The point where instability first arose was highlighted by the eigenvalues pair. Variations in $K_{P,PLL}$ and $K_{I,PLL}$ were implemented, and the resulting eigenvalue trajectories can be seen in Fig. 2.11. An increase in both controller gains, and

2.3. Grid Strength Definition and Small-Signal Stability Assessment

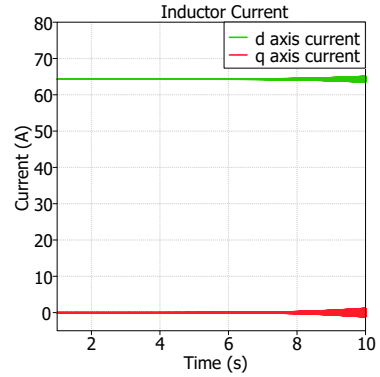
(a) $K_{P,PLL}$ is varied from 0.1 (blue) to 10 (red) times $K_{P,PLL0}$ (b) $K_{I,PLL}$ is varied from 0.1 (blue) to 100 (red) times $K_{I,PLL0}$ **Fig. 2.11:** Eigenvalue trajectories for variations in PLL gains ($K_{P,PLL}$ and $K_{I,PLL}$) for weak grid case scenario (SCR equal to 1.5). Green arrow means instability. Source: [C1].

consequently the PLL bandwidth, was found to contribute to instability. The reason for the instability is the possible interference with the inner current control loop, which has a faster response compared to PLL, and this fact makes high PLL bandwidths undesirable. However, the possible issues related with the dynamic performance of the PLL when it is designed with a low bandwidth should be considered.

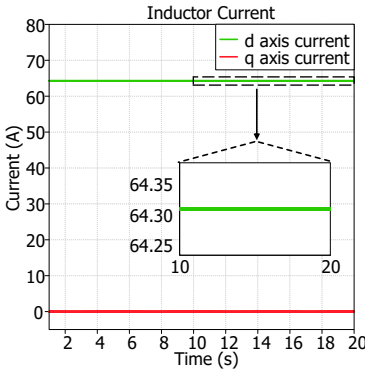
Similarly to the current controller's test cases, time domain simulations were



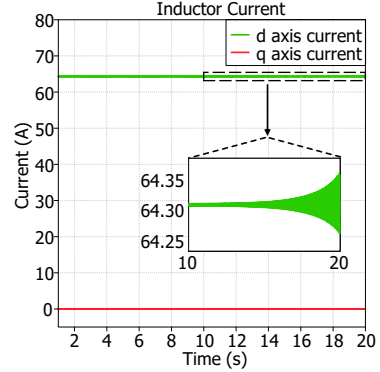
(a) $K_{P,PLL} = 0.3274$ at $t=2$ sec. The system remains stable.



(b) $K_{P,PLL} = 0.3437$ at $t=2$ sec. The system becomes unstable.



(c) $K_{I,PLL} = 54.17$ at $t=2$ sec. The system remains stable.

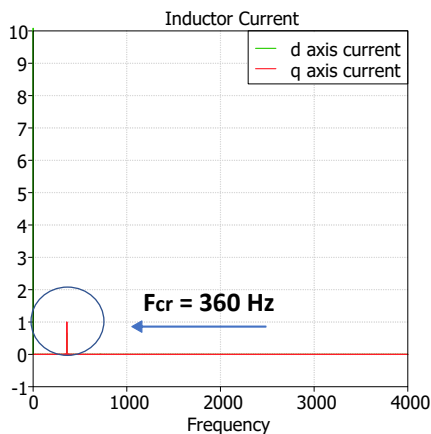


(d) $K_{I,PLL} = 58.34$ at $t=2$ sec. The system becomes unstable.

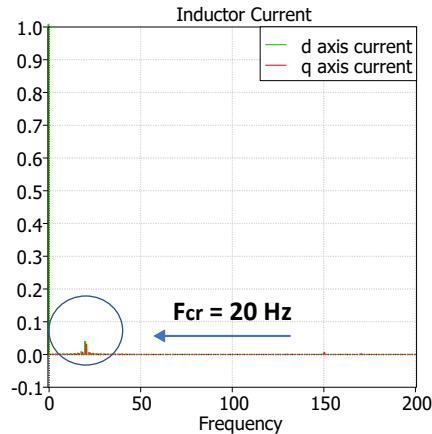
Fig. 2.12: Time-domain simulations - inductor current I_{Ld} for weak grid case scenario (SCR equal to 1.5) when small changes in the PLL control gains are applied at $t=2$ sec. Source: [C1].

conducted to investigate the sensitivity of the PLL control parameters when the SCR is set to 1.5. In this case, the PLL bandwidth increased from its default setting of 11.77 Hz to 22.6 Hz and 34.1 Hz, in response to step changes in $K_{P,PLL}$ and $K_{I,PLL}$, respectively. The outcomes of the simulation in time and frequency domain are presented in Figs. 2.12 and 2.13, respectively, and align closely with the stability analysis results from the small-signal model depicted in Fig. 2.11;

2.4. Conclusion



(a) FFT Analysis after a step change of $K_{P,PLL}$



(b) FFT Analysis after a step change of $K_{I,PLL}$

Fig. 2.13: FFT analysis - inductor current I_{Ld} (see Fig. 2.12) when instability is observed for weak grid case scenario (SCR equal to 1.5) after changes in the PLL control gains are applied at $t=2$ sec. Source: [C1].

thus, the eigenvalue trends observed in the small-signal model are confirmed.

2.4 Conclusion

The chapter has focused on creating a non-linear state-space model of a grid-connected VSC that includes an LC filter. The incorporation of the effects from the PLL dynamics, current control dynamics, LC filter and digital time delay has been considered in the structure of the small-signal model. A comprehensive small-signal model, characterized by detailed state equations, was analyzed for each component of the system. The eigenvalue trajectories were determined, and the trends in these eigenvalues were evaluated through time-domain simulations and FFT analysis when the system became unstable.

A high alignment was observed between the results derived from small-signal, time-domain, and FFT analysis for varying grid strength test scenarios, proving the high validity of the developed small-signal model. Consequently, this has enabled a highly accurate study of the sensitivity of vector current control and PLL structure within a non-linear grid-following converter model. The

valuable insight from the stability analysis performed could be the basis for further research directed to more complicating control topologies - such cases are presented in Chapter 3, where other controllers are explored - or to ensure a controller robustness.

There are certain limitations to be considered. While this research examined various SCR scenarios to cover all the grid strength aspects, it primarily focused on a specific operating point (30 kW, 0 kVAR). Nevertheless, the model's proven precision offers the opportunity to explore its sensitivity under a wide range of operating conditions. In addition, the simple case of modeling a 30 kW wind turbine has been evaluated through simulations of the grid-side converter in this chapter. This modelling approach lays the foundation for studying a more realistic case, as this model is upscaled to a 240 MW wind farm in Chapter 4.

Chapter 3

Stability Impact of Alternate Voltage Controller (AVC) on Wind Turbines

3.1 Background

A small-signal model for a grid-connected and grid-following VSC was developed in Chapter 2, with an emphasis on the inner current loop control and the PLL. This domain has gathered considerable research attention, addressing both eigenvalue-based and impedance-based stability analyses, and various control configurations have been explored to find out which one is the best in the literature.

Yet, the influence of the Alternate Voltage Controller (AVC) design, particularly when incorporating a low-pass filter (LPF), on system stability could be further investigated. The LPF within the AVC is very important, as it is necessary for filtering out voltage harmonics in the low-frequency range, specifically those up to the 2nd order of 50 Hz, which are typically introduced by outer-loop control interactions. Nevertheless, research into how this LPF might impact the control bandwidths of the outer loop controllers is still lacking. Thus, in this chapter, this gap is addressed, and the effects of the AVC's LPF on the stability of converter-based systems, in relation to the grid's strength, are analyzed. In fact, insight is provided into how AVC's design might alter the critical parameters of the PLL and AVC, which could result in system instabilities. The

small-signal analysis is validated through time domain simulations, and then the stability regions of the PLL and AVC bandwidth can be identified for the range of the AVC's LPF cutoff frequency under study.

After the model validation, the small-signal stability of a multi-VSC system connected to the grid is also analyzed, which follows the same principles with the model that includes the AVC control. The stability impact of its control parameters is studied, where high- and low- frequency interactions are identified by using participation factor analysis. This model can be the basis for future studies in grid-connected multi-VSC systems that include AVC control.

3.2 Updated State-Space Modeling

The grid-side converter of a wind turbine is reexamined, adopting again a grid-following control approach. Drawing from the methodology of Chapter 2, a PLL is integrated to synchronize the converter with the grid. A notable inclusion in this study is the AVC, which is tasked to regulate the voltage at the VSC's PCC. The AVC is used in grid-connected VSC systems of wind turbines, and especially in weak grid cases, where maintaining the alternating-voltage level at the PCC is of utmost importance and it can be a challenge [109]. This updated system configuration, featuring the AVC, can be viewed in Fig. 3.1, where most variables have already been defined in Chapter 2.

Elements such as the state-space models for the PLL, digital time delay, LC filter, and grid impedance are carried over from Chapter 2. Within the state-space model for the current controller, the reference for the q-axis current is governed by the AVC control loop, which will be elaborated upon in the following sections. Meanwhile, the d-axis current reference is derived from the set active power injection, as illustrated in (2.18). Furthermore, given that the feed-forward voltage, which is the voltage at PCC V_{PCC} , integrates a low-pass filter in the d-q domain (FF,LPF in Fig. 3.1), specific state equations are incorporated into the current controller's state-space model, and they are shown below:

$$\dot{V}_{PCCd, LPF} = -\omega_{FF,LPF}V_{PCCd,LPF} + \omega_{FF,LPF}V_{PCCd}^c \quad (3.1)$$

$$\dot{V}_{PCCq, LPF} = -\omega_{FF,LPF}V_{PCCq,LPF} + \omega_{FF,LPF}V_{PCCq}^c \quad (3.2)$$

3.2. Updated State-Space Modeling

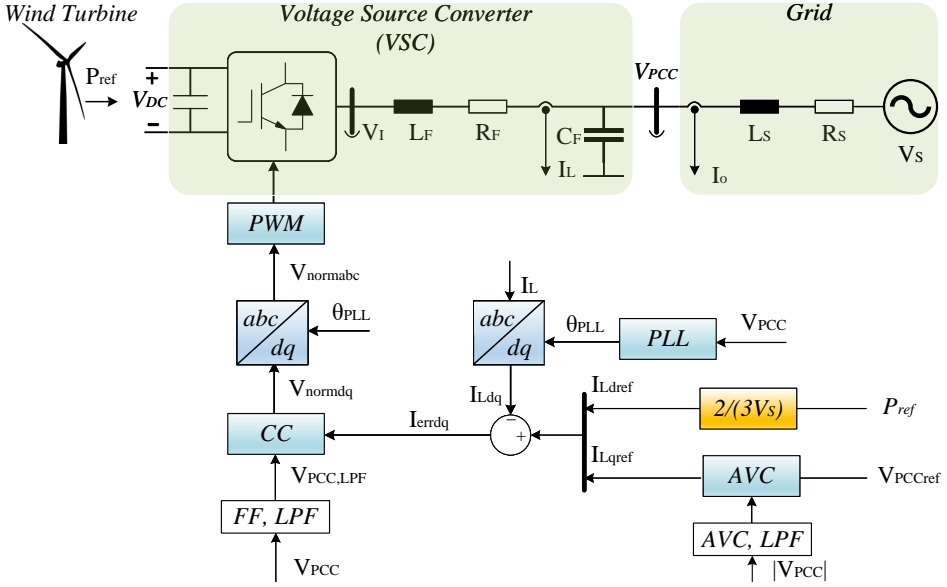


Fig. 3.1: Control structure of a wind turbine's grid-following converter which also entails an alternate voltage controller (AVC) including a low-pass filter (AVC,LPF). Source: [J1].

where $V_{PCC,LPF}$ is the feed-forward voltage after being filtered and $\omega_{FF,LPF}$ is the cutoff frequency of the low-pass filter at the feedforward voltage.

The updated current controller's vector, which now also includes the state variables of the low-pass filter at the feed-forward voltage, is shown below:

$$x_{CC,upd} = \begin{bmatrix} q_{errd} & q_{errq} & V_{PCCd,LPF} & V_{PCCq,LPF} \end{bmatrix} \quad (3.3)$$

3.2.1 Alternate Voltage Controller (AVC) Modeling

The outer control loop is in charge of the generation of the q-axis current reference (reactive current), in order to maintain a constant AC voltage. The AVC plays a vital role in modulating the voltage at the point of common coupling and it is typically implemented by using the classical PI control mechanism [J1]. This can be seen in Fig. 3.2.

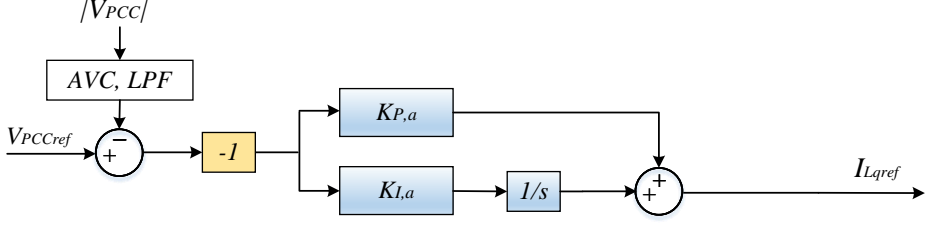


Fig. 3.2: Control structure of the alternate voltage controller (AVC) in Figure 3.1. Source: [J1].

As depicted in Fig. 3.2, the voltage magnitude at the PCC aligns with the desired reference voltage after it is filtered. This process is crucial for eliminating undesirable 2^{nd} -order harmonics introduced by outer-loop control interactions, as previously discussed in section 3.1. Therefore, the cutoff frequency of the low-pass filter (AVC,LPF in Figs. 3.1 and 3.2) will be at least equal to 100 Hz. The voltage magnitude is represented as V_M , defined as:

$$V_M = |V_{PCC}| = \sqrt{V_{PCCd}^2 + V_{PCCq}^2} \quad (3.4)$$

Subsequently, the reference current along the q-axis can be extracted using the following equation:

$$I_{Lqref} = -\left(K_{P,a}(V_{PCCref} - V_{M,LPF}) + K_{I,a}q_{errac}\right) \quad (3.5)$$

where q_{errac} represents the integrator of AVC, V_{PCCref} is the reference voltage at the PCC given as input to the AVC and $V_{M,LPF}$ is the voltage magnitude after being filtered.

The state variables of the AVC are:

$$x_{AVC} = \begin{bmatrix} q_{errac} & V_{M,LPF} \end{bmatrix} \quad (3.6)$$

The differential equations of the AVC are the following:

$$\dot{q}_{errac} = V_{PCCref} - V_{M,LPF} \quad (3.7)$$

$$\dot{V}_{M,LPF} = -\omega_{AVC,LPF}V_{M,LPF} + \omega_{AVC,LPF}V_M \quad (3.8)$$

where $\omega_{AVC,LPF}$ is the cutoff frequency of the low-pass filter at V_M .

3.3. Small-Signal Stability Analysis Assessment

3.3 Small-Signal Stability Analysis Assessment

The final state-space vector of the VSC system in (2.51) is now updated after including the state-space submodel of the AVC in (3.6) and the updated state-space submodel of the current controller in (3.3), and can be defined as:

$$x_{upd} = \begin{bmatrix} x_{PLL} & x_{CC,upd} & x_{AVC} & x_{TD} & x_{LC} \end{bmatrix} \quad (3.9)$$

The linearization of the updated state-space model is implemented by utilizing the linear approximation in (2.52), similarly with the discussion in Chapter 2. As the reference current in the q-axis is estimated by the AVC control loop, the corresponding fixed operating point needs to be estimated in order to proceed with the linearization around it and do the analysis. The equilibrium points computation is, therefore, implemented in 3.3.1, as well as in [J1].

3.3.1 Equilibrium Points Computation

The steady states of the state-space model include the voltage at PCC $V_{PCC,0}$ and the inductor current $I_{L,0}$, both in the dq reference frame. These states are utilized in (2.4)–(2.7).

Given that V_{PCCq} is set to zero by the PLL, the relevant equilibrium state $V_{PCCq,0}$ is also zero. With that fact and the definition of V_M in (3.4), the equilibrium state $V_{PCCd,0}$ is equal to V_{PCCref} ; furthermore, the equilibrium state of the inductor current along d-axis, $I_{Ld,0}$, is equal to I_{Ldref} . These equilibrium states were utilized in the linearization process at Chapter 2.

Kirchhoff's voltage law (KVL) on the grid side is utilized to derive the equilibrium state of the inductor current along the q-axis, $I_{Lq,0}$:

$$V_{PCCd,0} = V_{Sd,0} + R_S I_{od,0} - \omega_n L_S I_{oq,0} \quad (3.10)$$

Equations (3.11) and (3.12) illustrate the relationship between the steady-state converter current and the output current, for both the d- and q-axes:

$$I_{od,0} = I_{Ld,0} = I_{Ldref} \quad (3.11)$$

$$I_{oq,0} = I_{Lq,0} - \omega_n V_{PCCd,0} C_F \quad (3.12)$$

The grid voltage along the d-axis, represented as $V_{Sd,0}$, is defined as:

$$V_{Sd,0} = |V_{Sabc}| \cos \delta \quad (3.13)$$

Here, δ symbolizes the grid angle relative to each converter's capacitor voltage. This angle can be deduced by considering the active power injected to the grid by the converter in the abc frame:

$$P = \frac{3}{2} \frac{|V_{PCCabc}| |V_{Sabc}| \sin(\delta)}{\omega_n L_S} \quad (3.14)$$

As already discussed, the control is aligned with the d-axis. Consequently, the active power in the dq frame can be determined solely from the d-axis variables:

$$P = \frac{3}{2} V_{PCCd} I_{od} = \frac{3}{2} |V_{PCCabc}| I_{od} \quad (3.15)$$

Using both (3.14) and (3.15), the angle δ can be estimated, leading to:

$$\cos\delta = \sqrt{1 - \left(\frac{\omega_n L_S I_{od}}{|V_{Sabc}|} \right)^2} \quad (3.16)$$

Thus, by integrating (3.11), (3.12), (3.13), and (3.16) into (3.10), the equilibrium state of the inductor current on the q-axis is determined as:

$$I_{Lq,0} = \frac{\sqrt{|V_{Sabc}|^2 - \left(\omega_n L_S I_{Ldref} \right)^2} + R_S I_{Ldref} - V_{PCCref} \left(1 - (\omega_n)^2 L_S C_F \right)}{\omega_n L_S} \quad (3.17)$$

Upon the determination of these equilibrium points, the state-space model is linearized around them.

3.3.2 Eigenvalue Analysis Concerning PLL and AVC Critical Bandwidth

The eigenvalue analysis is conducted on the updated small-signal model that entails AVC control, and the corresponding updated system and control parameters are shown in Table 3.1, most of which are the same as in Chapter 2. To mitigate the influence of potential distortions on the PLL output signals from high-order harmonics, a low PLL bandwidth—specifically, 7.27 Hz—is chosen, following the discussion in subsection 2.2.2 of Chapter 2. The operating point of the active power is 30 kW, and the current controller's bandwidth is equal to 1 kHz, according to the discussion in subsection 2.2.3 of Chapter 2. The grid inductance, L_S , is given by (2.53), whereas, for this analysis, the grid resistance R_S is assumed negligible. The AVC's design is specified by L_S , which

3.3. Small-Signal Stability Analysis Assessment

in turn affects the AVC bandwidth if there is a change in the grid's strength. The reaction time of the inner-current loop is significantly faster than that of the outer-AVC loop; therefore the AVC's bandwidth should be notably below the current controller's bandwidth [J1].

Table 3.1: System and Default Control Parameters of Grid-Connected Converter System with AVC Control. Source: [J1].

	Description	Value
V_S	Grid Phase Voltage (peak value)	311 V
f_n	Rated Frequency	50 Hz
V_{DC}	DC Link Voltage Reference	800 V
L_F	Filter Inductance	5 mH
R_F	Filter Resistance	0.1 Ω
C_F	Filter Capacitance	10 μF
f_{sw}	Switching Frequency	20 kHz
f_S	Sampling Frequency	20 kHz
V_{PCCref}	Reference PCC Voltage (peak value)	280 V
P_{ref}	Nominal Active Power	30 kW
$\omega_{FF,LPF}$	Cutoff Frequency of Feedforward Voltage	100 rad/s
$K_{I,CC0}$	Default Integral Gain of Current Control	666.7
$K_{P,CC0}$	Default Proportional Gain of Current Control	33.3
$K_{I,PLL0}$	Default Integral Gain of PLL	0
$K_{P,PLL0}$	Default Proportional Gain of PLL	0.1637
$K_{I,a0}$	Default Integral Gain of AVC	100
$K_{P,a0}$	Default Proportional Gain of AVC	0

For the eigenvalue analysis, three different cutoff frequencies for the AVC's low-pass filter, denoted $f_{AVC,LPF}$, are chosen. Specifically, $f_{AVC,LPF}$ values of 20 Hz, 50 Hz (matching the nominal frequency), and 100 Hz are selected. The latter is considered the highest permissible cutoff frequency, since the filter's purpose is to isolate the 2^{nd} -order harmonics.

The eigenvalue sensitivity analysis is implemented to determine the small-signal stability and the controllers' impact. This assessment entails the adjustment of the control parameters of the system's control configurations, and subsequently analyzing the relationship between instability and the scale of the modifications. With each variation of the tested controller, the equilibrium states

of the state-space model are recalculated, and this continues until the system becomes unstable.

Weak Grid Case Scenario (SCR=1.5)

Firstly, a scenario of a weak grid is examined when the SCR stands at 1.5. Here, the grid inductance L_S is 10.3 mH and the AVC bandwidth equals 51 Hz. The VSC system's PLL proportional gain, $K_{P,PLL}$, undergoes several adjustments, beginning at 0.1 times its original value $K_{P,PLL0}$ (in deep blue) and increasing up to 10 times (in deep red). This is done to identify the specific PLL bandwidths that may create system instability. This analysis seeks to identify the range of $K_{P,PLL}$ values that contribute to a stable system. The outcomes of this investigation are illustrated in Fig. 3.3, where the critical PLL proportional gain, known as $K_{P,PLLcr}$, and its corresponding PLL bandwidth are determined for the studied $f_{AVC,LPF}$. Additionally, the oscillation frequency F_{cr} of the critical mode of instability is presented.

Similarly, this procedure is applied to identify the critical AVC bandwidth at which the system loses stability. The system's VSC default AVC integral gain, $K_{I,a0}$, is adjusted from 0.1 (deep blue) to 10 times (deep red). The findings are depicted in Fig. 3.4, where both the critical AVC integral gain $K_{I,acr}$, and the corresponding AVC bandwidth are identified for the relevant $f_{AVC,LPF}$. The oscillation frequency F_{cr} of the critical instability mode is also displayed. Concluding from the results, it appears that in weak grid scenarios, instability appears when the AVC bandwidth approaches 1/6 of the magnitude of the current controller's bandwidth.

Strong Grid Case Scenario (SCR=10)

Then, the scenario of a strong grid is examined, wherein the SCR is set to 10. In this case, the grid inductance, L_S , stands at 1.5 mH and the AVC bandwidth is recorded at 7.7 Hz. The PLL proportional gain $K_{P,PLL0}$ in the VSC of the system is altered, varying from 0.1 times (in deep blue) up to 10 times (in deep red). The aim is to ascertain whether there exist any critical PLL bandwidths under which the system would become unstable. The findings from this part of the study are illustrated in Fig. 3.5. Notably, based on the results, no critical PLL bandwidths that would compromise stability are identified for the examined $f_{AVC,LPF}$.

3.3. Small-Signal Stability Analysis Assessment

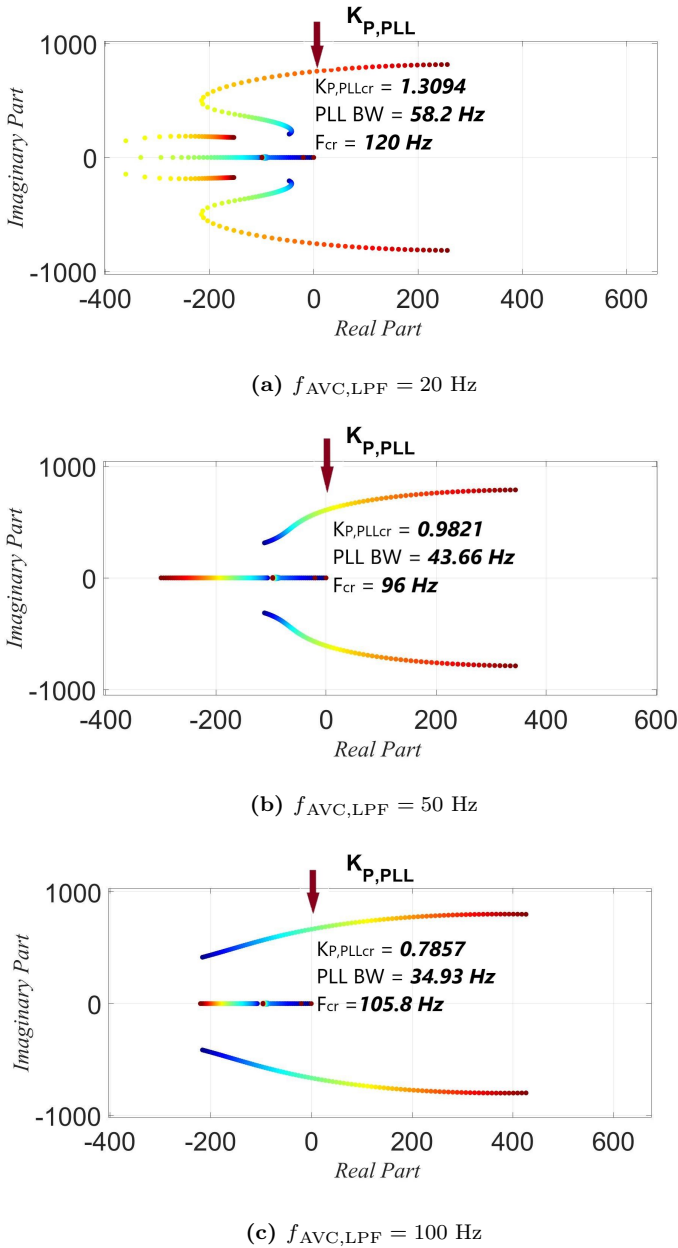


Fig. 3.3: Eigenvalue-based stability analysis for different AVC filter cases in the weak grid case scenario (SCR = 1.5). The critical bandwidth of the PLL is identified after $K_{P,PLL0}$ varies from 0.1 (deep blue) to 10 (deep red) times. Red arrow means instability. Source: [J1].

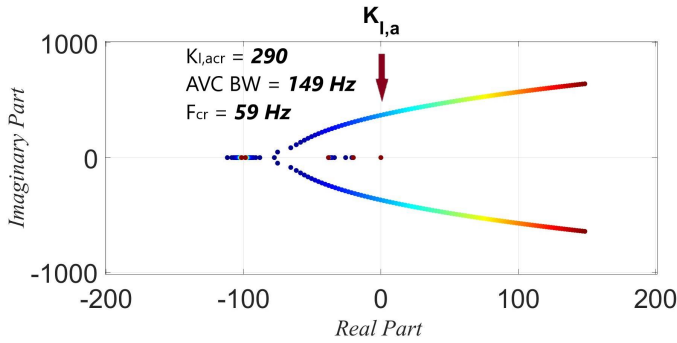
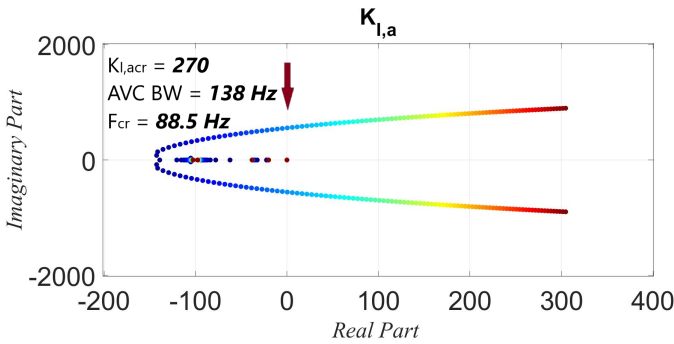
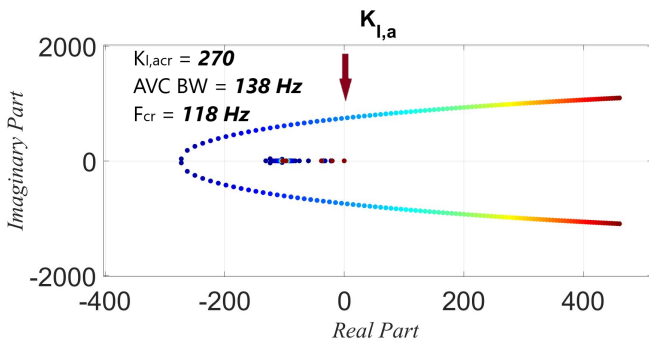
(a) $f_{AVC,LPF} = 20$ Hz(b) $f_{AVC,LPF} = 50$ Hz(c) $f_{AVC,LPF} = 100$ Hz

Fig. 3.4: Eigenvalue-based stability analysis for different AVC filter cases in the weak grid case scenario ($SCR = 1.5$). The critical bandwidth of the AVC is identified after $K_{I,a0}$ varies from 0.1 (deep blue) to 10 (deep red) times. Red arrow means instability. Source: [J1].

3.3. Small-Signal Stability Analysis Assessment

To estimate the critical AVC bandwidth at which the system would become unstable, the integral gain $K_{I,a0}$ is varied, ranging from 1 (in deep blue) to 200 times (in deep red). The outcomes of this stage of the analysis are presented in Fig. 3.6. Here, both the critical AVC integral gain, denoted as $K_{I,acr}$, and its associated AVC bandwidth are identified for the specific $f_{AVC,LPF}$. In addition, the oscillation frequency F_{cr} of the critical mode of instability is depicted.

Drawing on these results, the instability in the strong grid case emerges when the AVC bandwidth obtains a relatively high value. This threshold appears to be marginally greater than $2/3$ of the bandwidth of the current controller. Furthermore, there is a noticeable trend indicating that as $f_{AVC,LPF}$ increases, this critical bandwidth tends to undergo a reduction.

3.3.3 Time-Domain Stability Analysis

To validate the dynamic response of the used small-signal model, time domain simulations were conducted using MATLAB Simulink and the PLECS block set, similarly with Chapter 2. Both weak and strong grid case scenarios were explored in these simulations. According to the following simulations, the steady state inductor current in the q-axis I_{Lq} is not zero, as the voltage at PCC is controlled by the AVC to follow a given reference value; in addition, it is different in each strength case, accordingly to (3.17). The model was subjected to three distinct cases of AVC's low-pass filter, with $f_{AVC,LPF}$ set to 20 Hz, 50 Hz, and 100 Hz. FFT analysis was employed to identify the dominant frequency under unstable system conditions. Subsequently, a comparison with results from the eigenvalue-based stability analysis was performed.

Time Domain Analysis in Weak Grid Case Scenario

In the weak grid case scenario, where $SCR = 1.5$, an initial examination of the influence of PLL on the system's stability was conducted under different $f_{AVC,LPF}$ cases. At $t = 1.5$ seconds, a step change was introduced to the default proportional gain of the PLL, denoted as $K_{P,PLL0}$, during stable system conditions. This alteration led the controller's gain to a value, represented by $K_{P,PLLcr}$, that critically impacted the system's stability. To illustrate instances of instability, the inductor current I_L in the dq frame was deployed. In Fig. 3.7, both the $K_{P,PLLcr}$ and the corresponding critical frequency, as detected through FFT analysis, are depicted.

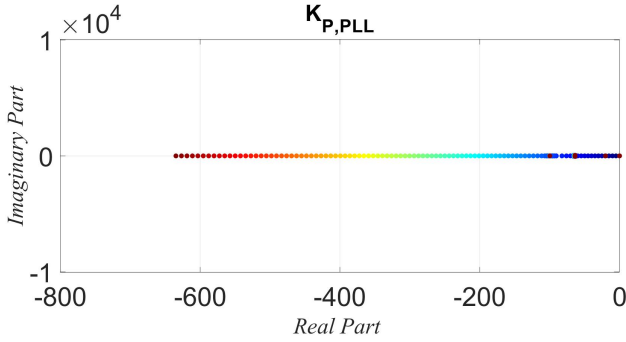
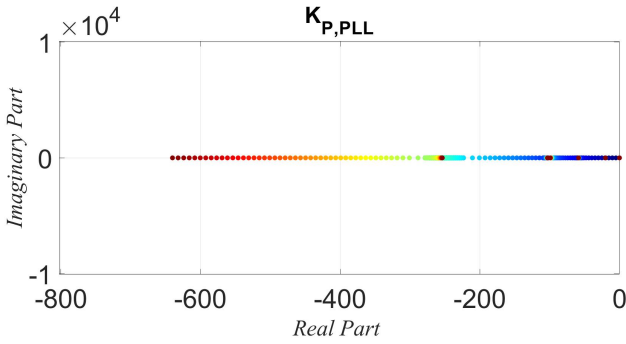
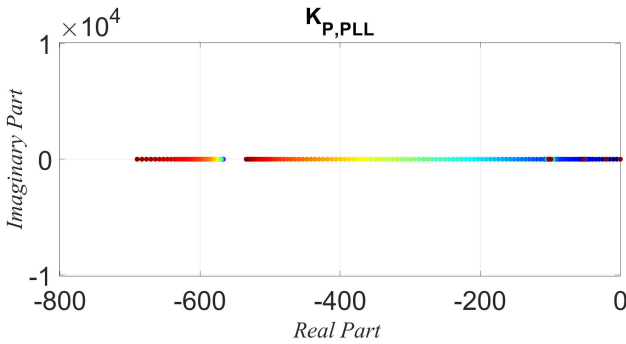
(a) $f_{AVC,LPF} = 20$ Hz(b) $f_{AVC,LPF} = 50$ Hz(c) $f_{AVC,LPF} = 100$ Hz

Fig. 3.5: Eigenvalue-based stability analysis for different AVC filter cases in the strong grid case scenario ($SCR = 10$). $K_{P,PLL0}$ varies from 0.1 (deep blue) to 10 (deep red) times. Source: [J1].

3.3. Small-Signal Stability Analysis Assessment

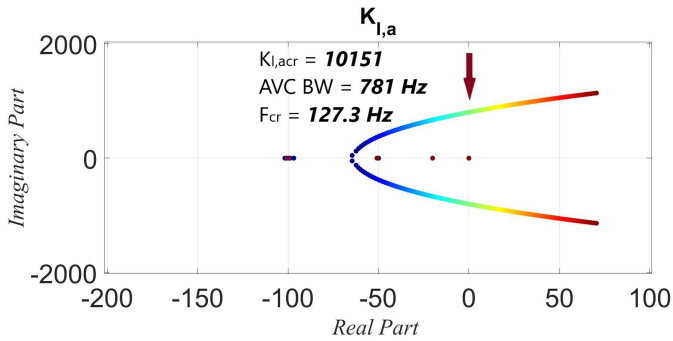
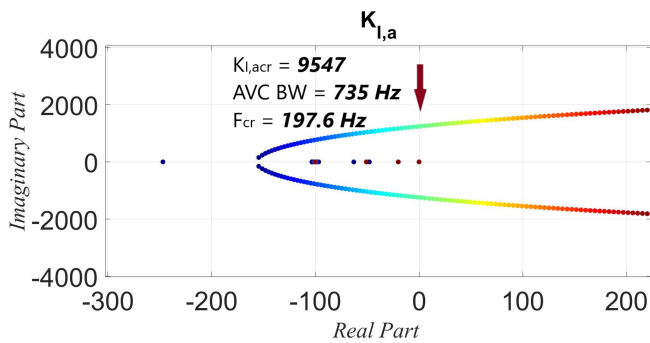
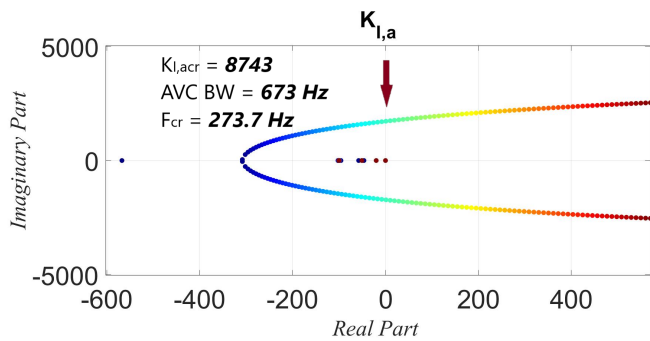
(a) $f_{AVC,LPF} = 20$ Hz(b) $f_{AVC,LPF} = 50$ Hz(c) $f_{AVC,LPF} = 100$ Hz

Fig. 3.6: Eigenvalue-based stability analysis for different AVC filter cases in the strong grid case scenario (SCR = 10). The critical bandwidth of the AVC is identified after $K_{I,a0}$ varies from 1 (deep blue) to 200 (deep red) times. Red arrow means instability. Source: [J1].

Then, the effect of the AVC bandwidth on the system's stability was examined under the same $f_{\text{AVC,LPF}}$ conditions. At $t = 1.5$ seconds, when the system was stable, a ramp change with a minimal slope was applied on the integral gain of the AVC, symbolized by $K_{\text{I,a0}}$. Opting for a ramp was necessary by its capacity to represent multiple steps, offering a more accurate representation for integrated values compared to a single step. This procedure allowed for the identification of the controller's gain value, referred to as $K_{\text{I,acr}}$, that impacted the system's stability. To depict the instability scenarios, the inductor current in the dq frame was once again employed. Fig. 3.8 exhibits the $K_{\text{I,acr}}$ and the associated critical frequency, as determined by the FFT analysis.

The results presented in Figs. 3.7 and 3.8 align closely with those obtained from the small-signal stability analysis depicted in Figs. 3.3 and 3.4, respectively. Consequently, this serves to affirm the high level of accuracy that the eigenvalue-based stability analysis offers in the weak grid case scenario.

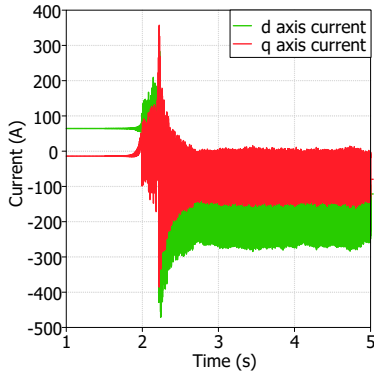
Time Domain Analysis in Strong Grid Case Scenario

In the strong grid case scenario ($SCR = 10$), the analysis procedure is the same as in the weak grid case scenario. Initially, the influence of PLL on the system's stability was examined under varying $f_{\text{AVC,LPF}}$ cases. For all $f_{\text{AVC,LPF}}$ cases, the same step change was applied to $K_{\text{P,PLL0}}$ at $t = 1.5$ s (equal to 10 times $K_{\text{P,PLL0}}$) during a stable system state. The time domain simulation outcomes, representing the inductor current in the dq frame, are depicted in Fig. 3.9. These findings prove that alterations in $f_{\text{AVC,LPF}}$ exert no influence on the system's stability, even when the $K_{\text{P,PLL}}$ is increased. Thus, in the strong grid—and across all $f_{\text{AVC,LPF}}$ cases—the system remains stable when the PLL bandwidth is changed.

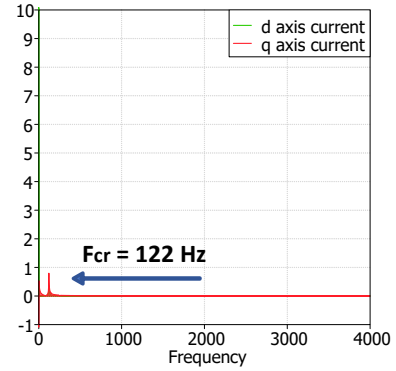
Similarly to the weak grid case scenario, the effect of the AVC bandwidth on the system stability was examined during the simulation procedure for different $f_{\text{AVC,LPF}}$ cases. At $t = 1.5$ s, while the system was stable, a ramp change with a higher slope than that in the weak grid case was applied to $K_{\text{I,a0}}$. This adjustment was necessary as the instability appeared at a significantly higher AVC bandwidth. Fig. 3.10 presents the graphs of the inductor current in the dq frame, alongside the corresponding FFT analysis, thereby illustrating the instances of instability.

Remarkably, the simulation results illustrated in Figs. 3.9 and 3.10 align closely with those obtained from the small-signal stability analysis, as depicted

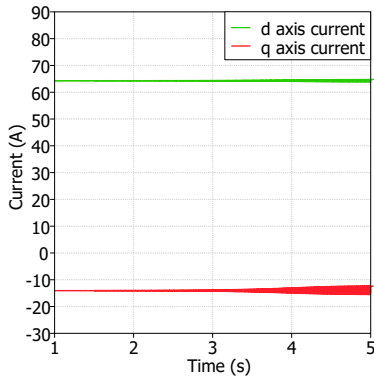
3.3. Small-Signal Stability Analysis Assessment



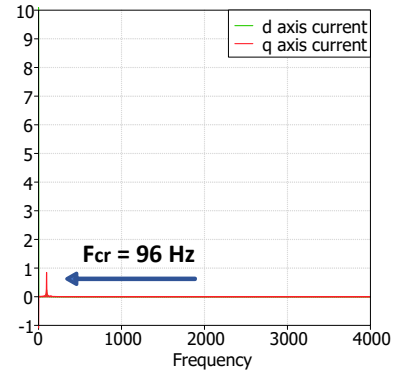
(a) $K_{P,PLLcr} = 1.3094$ when $f_{AVC,LPF} = 20$ Hz



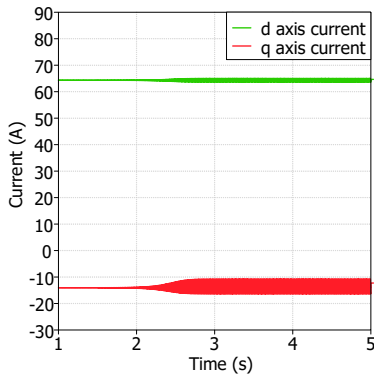
(b) Dominant oscillation frequency when $f_{AVC,LPF} = 20$ Hz



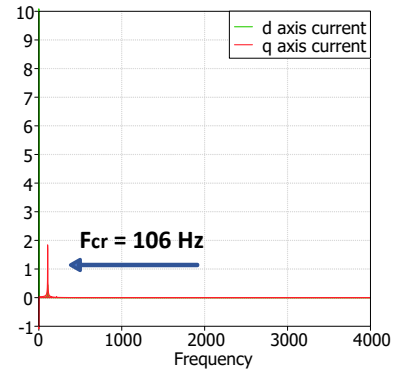
(c) $K_{P,PLLcr} = 0.9657$ when $f_{AVC,LPF} = 50$ Hz



(d) Dominant oscillation frequency when $f_{AVC,LPF} = 50$ Hz



(e) $K_{P,PLLcr} = 0.7857$ when $f_{AVC,LPF} = 100$ Hz



(f) Dominant oscillation frequency when $f_{AVC,LPF} = 100$ Hz

Fig. 3.7: Time domain simulations and frequency analysis (FFT) of the VSC inductor current I_L for different AVC filter cases. The stability impact of PLL in a weak grid (SCR = 1.5) was observed, caused after the step change in $K_{P,PLL0}$ to its critical value $K_{P,PLLcr}$ at $t=1.5$ s. The dominant oscillation frequency is shown when $K_{P,PLL}$ obtains its critical value. Source: [J1].

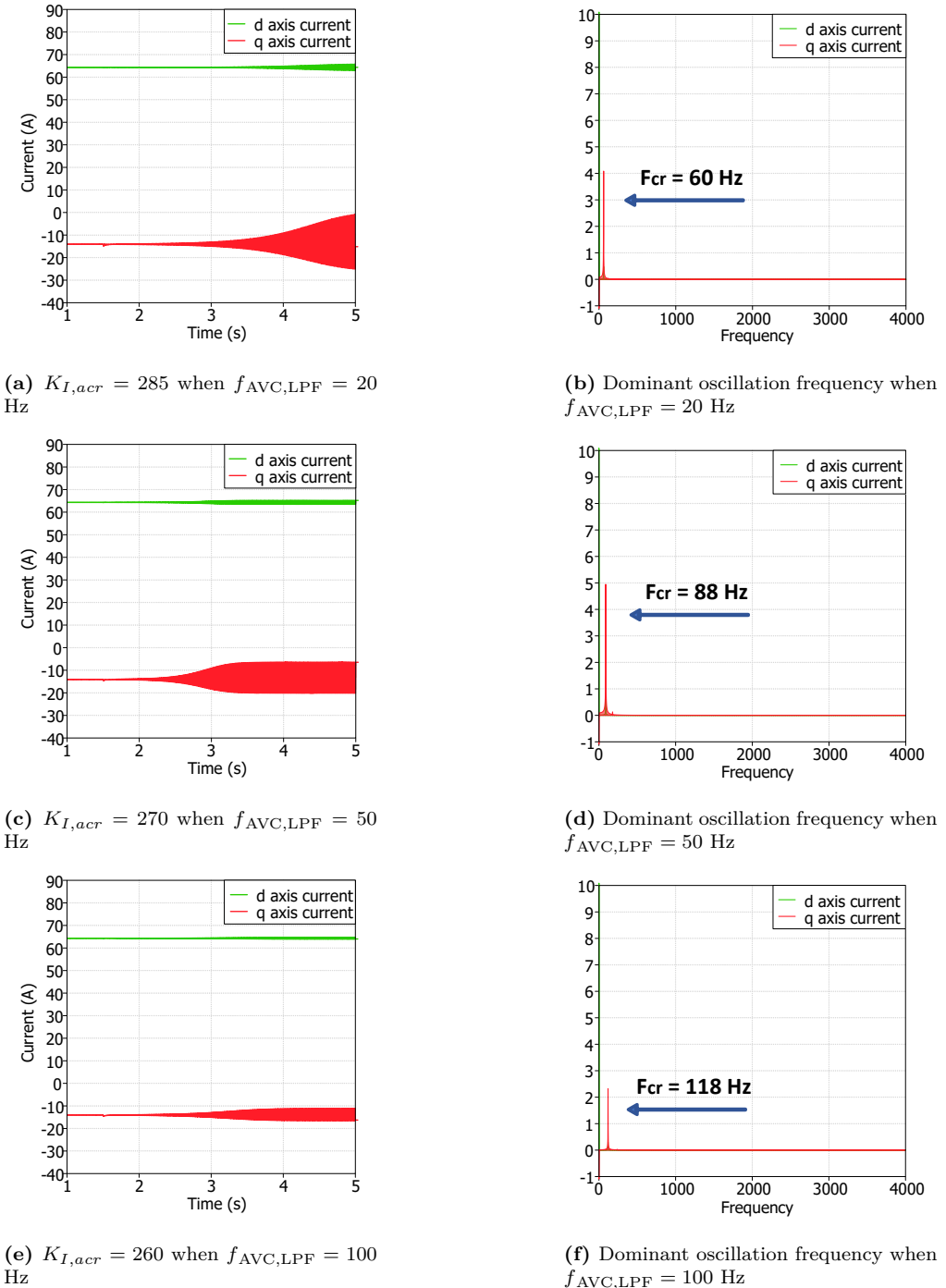


Fig. 3.8: Time domain simulations and frequency analysis (FFT) of the VSC inductor current I_L for different AVC filter cases. The stability impact of AVC in the weak grid ($SCR = 1.5$) is observed, caused after the ramp change in $K_{I,a0}$ to its critical value $K_{I,acr}$ at $t=1.5$ s. The dominant oscillation frequency is shown when $K_{I,a}$ obtains its critical value. Source: [J1].

3.3. Small-Signal Stability Analysis Assessment

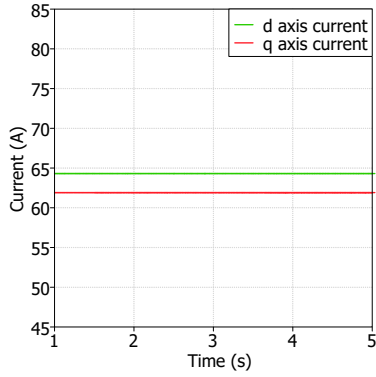
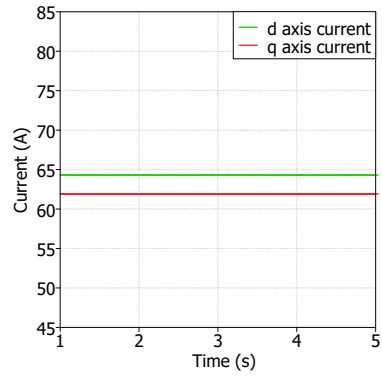
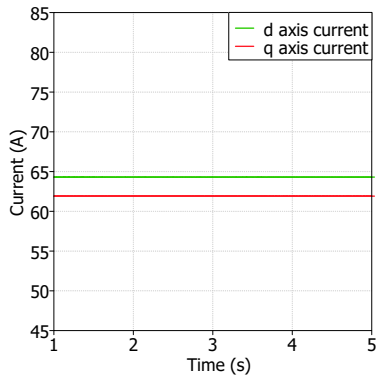
(a) $f_{AVC,LPF} = 20$ Hz(b) $f_{AVC,LPF} = 50$ Hz(c) $f_{AVC,LPF} = 100$ Hz

Fig. 3.9: Time domain simulations of the VSC inductor current I_L for different AVC filter cases. The step change in PLL's proportional gain at $t=1.5$ s from $K_{P,PLL0} = 0.1637$ to $K_{P,PLL} = 1.637$ has no stability impact in the strong grid case ($SCR = 10$). Source: [J1].

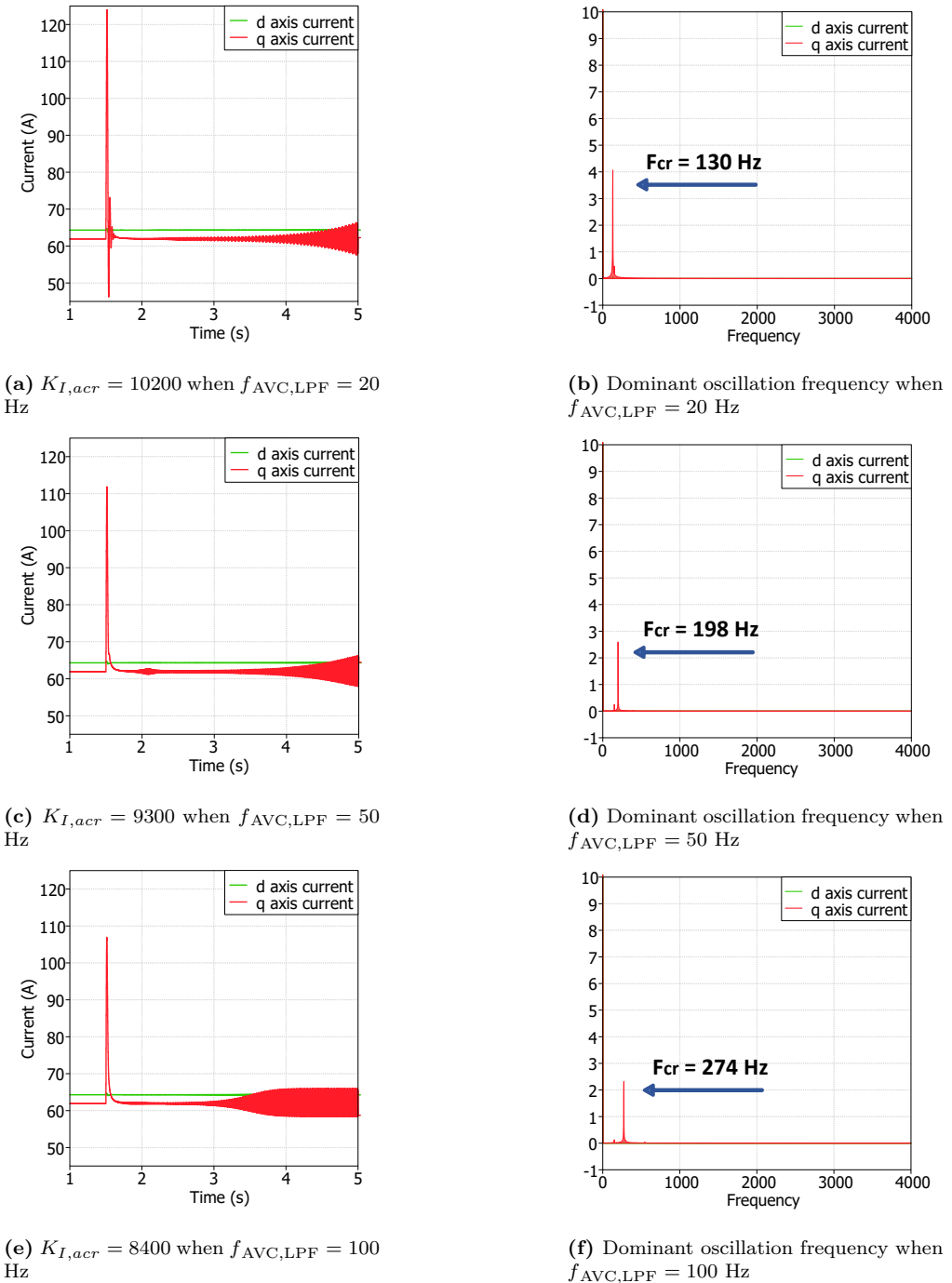


Fig. 3.10: Time domain simulations and frequency analysis (FFT) of the VSC inductor current I_L for different AVC filter cases. The stability impact of AVC in a strong grid ($SCR = 10$) is observed, caused after the ramp change in $K_{I,a0}$ to its critical value $K_{I,acr}$ at $t=1.5$ s. The dominant oscillation frequency is shown when $K_{I,a}$ obtains its critical value. Source: [J1].

3.4. Stability Region Mapping of PLL and AVC for Different Cases of AVC's LPF

in Figs. 3.5 and 3.6, respectively. Hence, in the strong grid case scenario—as it was observed in the weak grid case—the eigenvalue-based stability analysis has been precisely validated.

3.4 Stability Region Mapping of PLL and AVC for Different Cases of AVC's LPF

The assessment of the small-signal stability analysis, elaborated upon in subsection 3.3, provided the eigenvalue trajectories for the PLL and AVC bandwidths corresponding to specific values of the AVC's LPF cutoff frequency, $f_{\text{AVC,LPF}}$. This analysis, whose accuracy has been demonstrated by time domain simulation, facilitates the identification of stability regions for the system in Table 3.1 as $f_{\text{AVC,LPF}}$ varies, and that procedure is also described in [J1].

3.4.1 Weak Grid Case Scenario

In a weak grid case scenario ($\text{SCR} = 1.5$), the stability region of the PLL bandwidth is depicted in Fig. 3.11. As per these graphs, the critical PLL bandwidth is determined to be 58.2 Hz when $f_{\text{AVC,LPF}}$ is set at 20 Hz. This critical bandwidth is observed to sharply decline to 40 Hz, entering into the subsynchronous frequency range, as the cutoff frequency transitions from 20 Hz to 60 Hz. Then, this bandwidth diminishes more gradually, settling at 34.93 Hz as $f_{\text{AVC,LPF}}$ varies from 60 Hz to 100 Hz. For $f_{\text{AVC,LPF}}$ equal to 20 Hz, the oscillation frequency associated with the critical PLL bandwidth is equal to 120.16 Hz. As $f_{\text{AVC,LPF}}$ shifts from 20 Hz to 56 Hz, this frequency diminishes to 96.13 Hz, but ascends to 105.84 Hz when $f_{\text{AVC,LPF}}$ alters from 56 Hz to 100 Hz.

Similarly, the stability region of the AVC bandwidth in the weak grid case is illustrated in Fig. 3.12. Here, the critical AVC bandwidth is equal to 149 Hz for an $f_{\text{AVC,LPF}}$ of 20 Hz. This critical bandwidth declines to 143 Hz as the cutoff frequency increases from 24 Hz to 44 Hz, and ultimately stabilizes at 138 Hz up until $f_{\text{AVC,LPF}}$ reaches 100 Hz. Hence, the critical AVC bandwidth remains largely unaffected from fluctuations in $f_{\text{AVC,LPF}}$. The oscillation frequency corresponding to this critical AVC bandwidth stands at 58.9 Hz for an $f_{\text{AVC,LPF}}$ of 20 Hz, and this frequency increases to 118.4 Hz as $f_{\text{AVC,LPF}}$ ranges from 20 Hz to 100 Hz.

A general observation from the eigenvalue stability trends in a VSC system

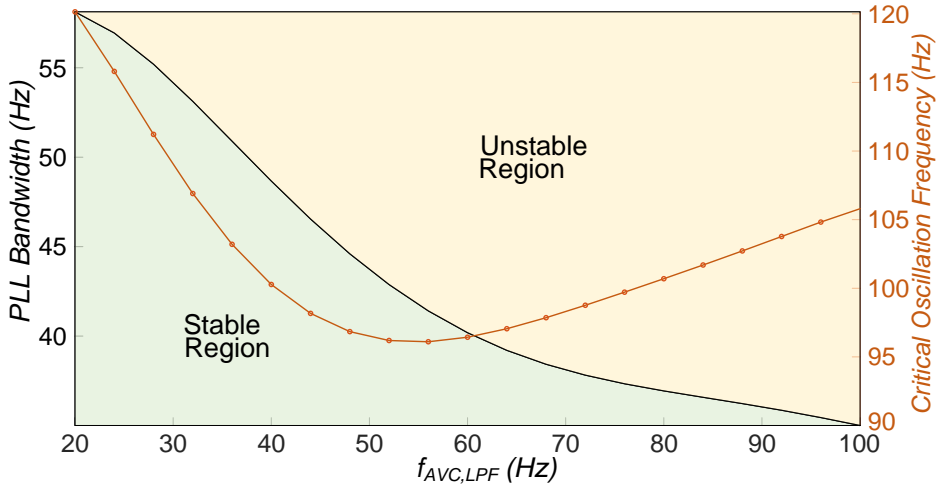


Fig. 3.11: Stability regions of PLL bandwidth in weak grid case ($SCR = 1.5$), when the $f_{AVC,LPF}$ varies from 20 to 100 Hz. The corresponding critical oscillation frequency to the critical PLL bandwidth is shown too (red). Source: [J1].

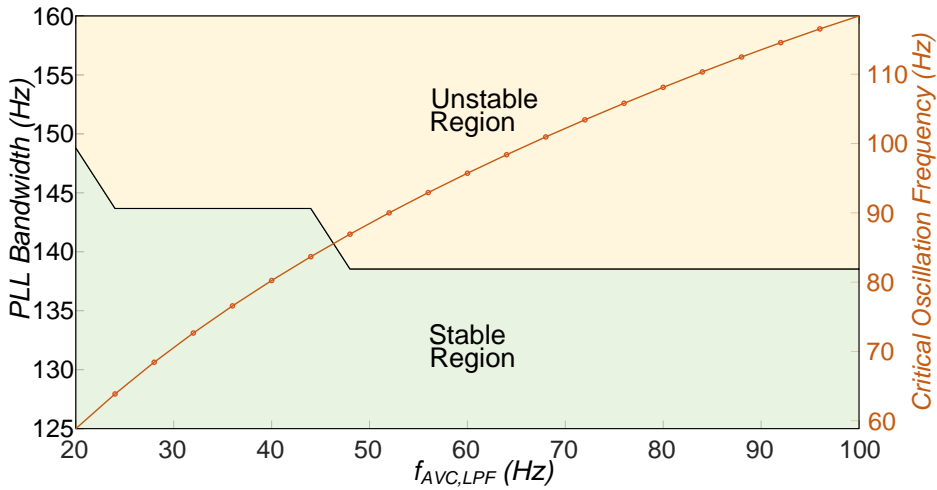


Fig. 3.12: Stability regions of AVC bandwidth in weak grid case ($SCR = 1.5$), when the $f_{AVC,LPF}$ varies from 20 to 100 Hz. The corresponding critical oscillation frequency to the critical AVC bandwidth is shown too (red). Source: [J1].

3.4. Stability Region Mapping of PLL and AVC for Different Cases of AVC's LPF

connected to a weak grid with a grid-following control structure, is that the outer-loop controllers' critical bandwidth for both the PLL and the AVC decreases as the $f_{AVC,LPF}$ rises. For the critical AVC, this decrease is minor, suggesting that the $f_{AVC,LPF}$ does not play a pivotal role in stability when the VSC system operates in connection with weak grids.

3.4.2 Strong Grid Case Scenario

In a strong grid case scenario ($SCR = 10$), Fig. 3.13 shows the stability region of the PLL. According to this result, the PLL bandwidth does not affect the system's stability under strong grid conditions, a finding that is in agreement with the small-signal stability evaluation as detailed in subsection 3.3. Thus, the instability region is stable, resulting in an absence of oscillation frequencies, and therefore it is a robust system.

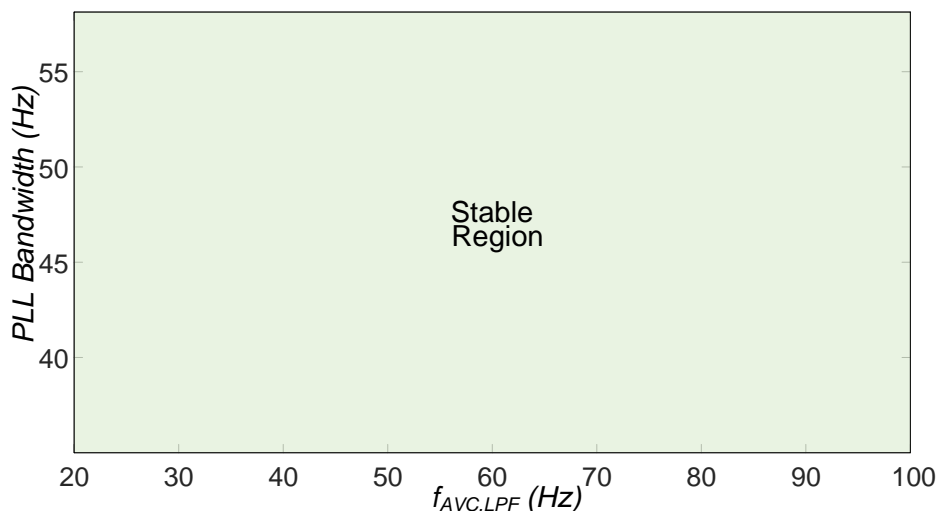


Fig. 3.13: Stability regions of PLL bandwidth in strong grid case ($SCR = 10$), when the $f_{AVC,LPF}$ varies from 20 to 100 Hz. The system is stable for the PLL bandwidth in question; therefore, no critical oscillation frequencies are shown. Source: [J1].

Similarly, the stability region of the AVC bandwidth under the strong grid scenario is depicted in Fig. 3.14. Here, the critical AVC bandwidth is approximately 781 Hz when $f_{AVC,LPF}$ is set at 20 Hz; this value drops to roughly 673 Hz

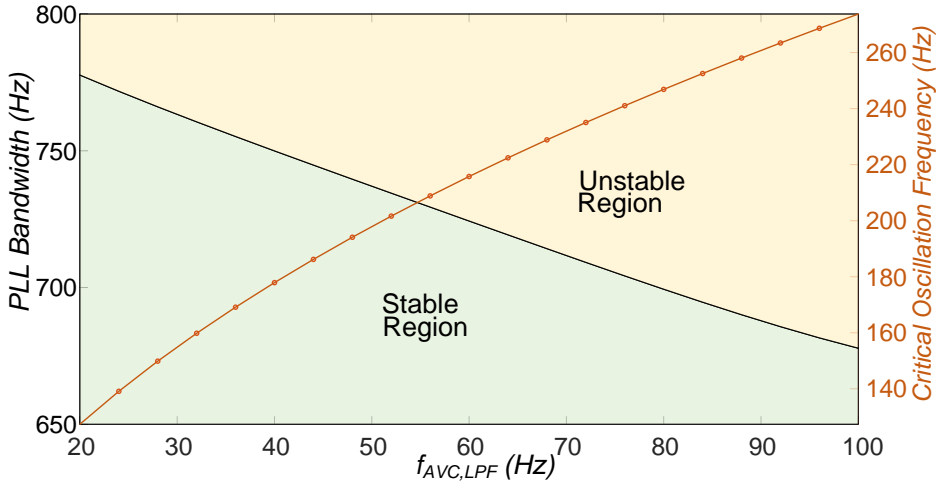


Fig. 3.14: Stability regions of the AVC bandwidth in a strong grid case ($SCR = 10$), when the $f_{AVC,LPF}$ varies from 20 to 100 Hz. The corresponding critical oscillation frequency to the critical AVC bandwidth is shown too (red). Source: [J1].

as the cutoff frequency fluctuates from 24 to 100 Hz. For $f_{AVC,LPF}$ equal to 20 Hz, the oscillation frequency tied to this critical AVC bandwidth is measured at 127 Hz, and this value increases to 273 Hz as $f_{AVC,LPF}$ varies from 20 to 100 Hz.

In general, from the eigenvalue stability trends in a VSC system, which is connected to a strong grid and has a grid-following control structure, it is evident that the PLL' design has minimal impact on the system's robustness. In contrast, the critical bandwidth of the AVC decreases significantly as the $f_{AVC,LPF}$ increases, highlighting an inverse relationship between them.

3.5 Small-Signal Analysis in Multi-Converter System

Having examined and validated the small-signal model of the VSC with AVC control, and after understanding its effects in both strong and weak grid scenarios, a pathway for developing a small-signal model for a system with multiple converters based on this setup has been paved. The main approach adopted for creating the initial model of the multi-converter system assumes that all VSCs have homogeneous dynamics. This implies that they have been designed sim-

3.5. Small-Signal Analysis in Multi-Converter System

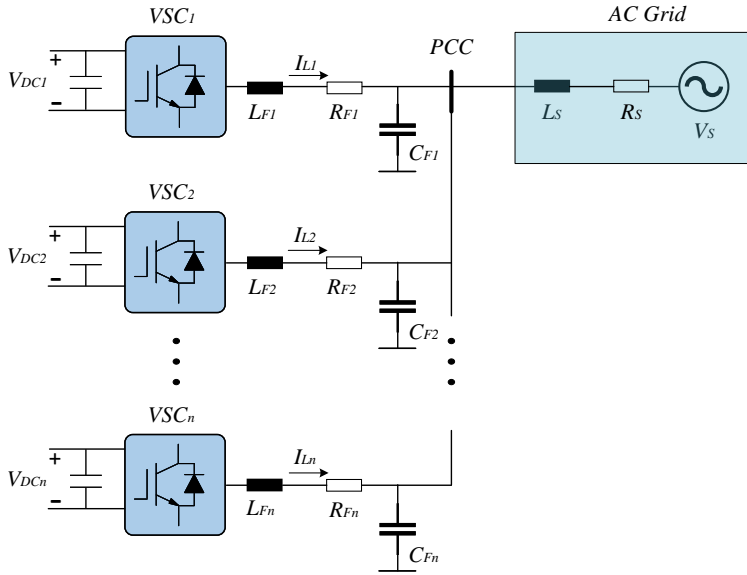


Fig. 3.15: Multi-VSC-Based Grid with n VSCs, where the sources are wind turbines. Source: [J3].

ilarly and adhere to the same control principles. When n of these converters are connected in parallel, a common synchronization point and a shared PCC are used. Due to this configuration, the decision was made not to consider the transformer's leakage inductance of each individual VSC in this study [J3]. This decision led to a simplified final model, which can be seen in Fig. 3.15.

By taking the nonlinear model, as referenced in (2.1) for one VSC, a framework has been established for a system including n parallel converters. The state equations of each converter connected to the grid were combined, resulting in

the state-space model for a system with n VSCs, detailed in (3.18).

$$\begin{aligned}
 \begin{bmatrix} \dot{x}_{VSC1} \\ \dot{x}_{VSC2} \\ \vdots \\ \dot{x}_{VSCn} \end{bmatrix} &= \begin{bmatrix} A_{VSC1} & 0 & \cdots & 0 \\ 0 & A_{VSC2} & \ddots & \vdots \\ \vdots & & \ddots & 0 \\ 0 & \cdots & 0 & A_{VSCn} \end{bmatrix} \begin{bmatrix} x_{VSC1} \\ x_{VSC2} \\ \vdots \\ x_{VSCn} \end{bmatrix} \\
 &+ \begin{bmatrix} R_{VSC1} & 0 & \cdots & 0 \\ 0 & R_{VSC2} & \ddots & \vdots \\ \vdots & & \ddots & 0 \\ 0 & \cdots & 0 & R_{VSCn} \end{bmatrix} \begin{bmatrix} x_{VSC1}, u_{VSC1} \\ x_{VSC2}, u_{VSC2} \\ \vdots \\ x_{VSCn}, u_{VSCn} \end{bmatrix} \quad (3.18)
 \end{aligned}$$

Subsequently, the equilibrium states for each converter are estimated. Given the influence of the AVC control setup, a generalized methodology similar to the one with one VSC was employed, but adapted for multiple VSCs, and the equilibrium state of the voltage V_{PCCi} and current I_{Li} are estimated for each converter on the dq axis, where $i = 1 \dots n$, and corresponds to the converter under study VSC_i .

The equilibrium state of the d-axis voltage at the PCC - which is defined as $V_{PCCdi,0}$ - between the VSC_i and the AC grid, is equal to the $V_{PCC,ref}$ and is the same for all VSCs of the system. Likewise, $V_{PCCqi,0}$ is equal to 0. In addition, the equilibrium state of the active inductor current for the grid-connected VSC_i , which is defined as $I_{Ldi,0}$, is equal to the reference active current $I_{d,ref}$. After following a methodology, which is analytically presented in [J3], the equilibrium state of the inductor current on the q-axis $I_{Lqi,0}$ for each converter can be gained from the following formula:

$$\begin{aligned}
 I_{Lqi,0} &= \left(\frac{K_{I,ai}}{K_{I,a1} + \dots + K_{I,an}} \right) \frac{1}{\omega_n L_S} \\
 &\times \left[\sqrt{|V_{Sabc}|^2 - (n\omega_n L_S I_{Ldref})^2} \right. \\
 &\left. + nR_S I_{Ldref} - V_{PCCref} (1 - n(\omega_n)^2 L_S C_{Fi}) \right] \quad (3.19)
 \end{aligned}$$

3.5. Small-Signal Analysis in Multi-Converter System

Upon determining the equilibrium states for the multi-VSC system, it becomes feasible to perform linearization around these states, thereby facilitating a stability analysis.

3.5.1 Eigenvalue Stability Analysis and Time Domain Analysis in Multi-Converter Model

A weak grid case scenario is defined when the SCR has been set to 1.5. As described in [J3], the grid strength becomes lower when more VSCs are connected to it. An eigenvalue analysis of the small-signal model has been displayed for the system and the control parameters found in Table 3.1. This approach mirrors what was done with the single VSC model. For this study, the AVC's LPF was kept constant, with $\omega_{AVC,LPF}$ established at 50 rad/s in order to mitigate possible voltage distortions.

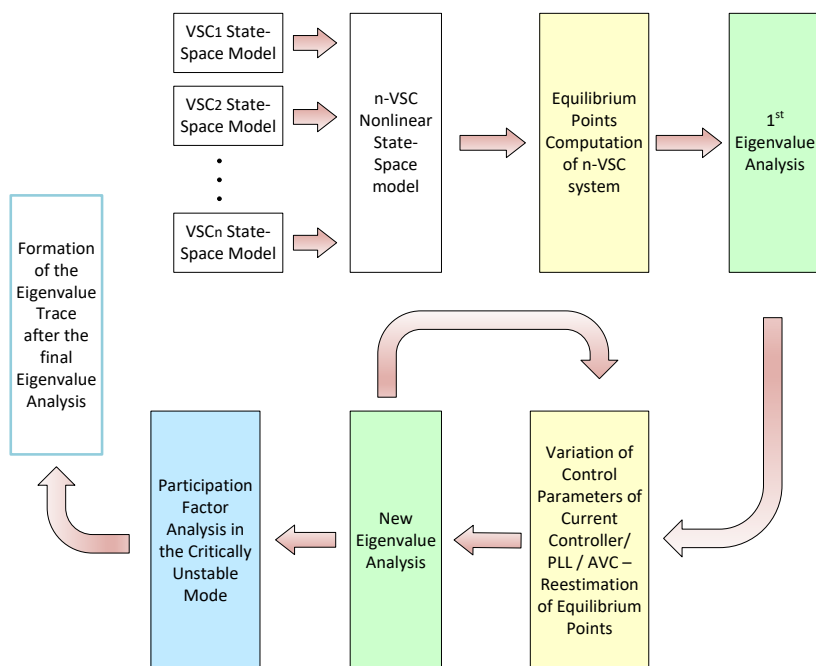


Fig. 3.16: Methodology for eigenvalue analysis in a n-VSC system when the control parameters are varied. Source: [J3].

As different controller variations have been explored, the equilibrium points of the system's state-space model were recalibrated, and the eigenvalue analysis identified any potential instability at times. The analysis steps of the eigenvalue analysis for an n -VSC system are illustrated in Fig. 3.16.

Eigenvalue-based Stability Analysis in Multi-Converter Model

First, the current controller proportional gain $K_{P,CC1}$ of a single VSC (VSC_1) was varied in a system with $n = 2$ VSCs, ranging from 0.1 (deep blue) to 10 (deep red) times its default value $K_{P,CC0}$. The unstable eigenvalue pairs are shown in Fig. 3.17a. In this figure, the notable critical gain and critical frequency are highlighted. From the observed movement of the eigenvalue trajectory, it can be seen that as the proportional gain of the current controller goes up, instability in the system tends to follow. Similarly to Chapter 2, the critical frequency was found to be roughly $1/6$ of the sampling frequency f_s .

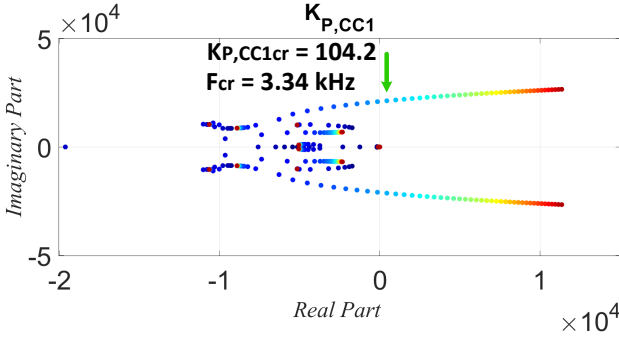
Moving to the stability analysis for the PLL, the proportional gain $K_{P,PLL1}$ of VSC_1 was varied from 0.1 (deep blue) to 20 (deep red) times its typical value $K_{P,PLL0}$. The aim here was to identify the critical PLL bandwidth that leads the multi-VSC system to an unstable condition. The outcomes are shown in Fig. 3.17b. Here, signs of system instability are clear when the PLL proportional gain obtains a value equal to 2.48, and the critical PLL bandwidth reaches 110.07 Hz. The dominant oscillation frequency is equal to $f_{cr} = 187$ Hz, and lies above the subsynchronous frequency range, which can be justified by the low value of the AVC's LPF.

Additionally, the AVC's outer loop was identified as a potential source of instability within the lower frequency spectrum in a multi-VSC system. This phenomenon is showcased in Fig. 3.17c, where the integral gain $K_{I,a1}$ of VSC_1 was varied between 0.1 (deep blue) and 200 (deep red) times its standard value $K_{I,a0}$. From the eigenvalue analysis, instability was observed when $K_{I,acr} = 857$, with a dominant oscillation frequency being near the 1st harmonic, specifically at $f_{cr} = 45$ Hz.

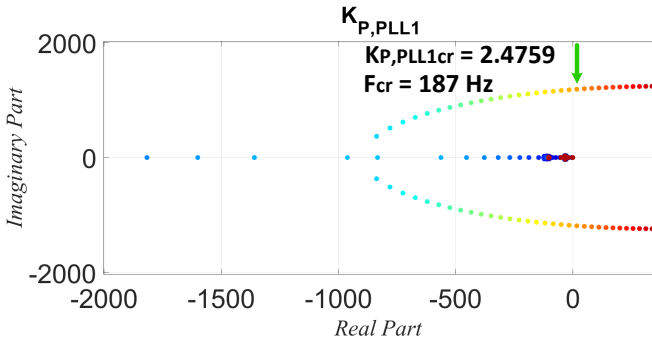
Participation Factor Analysis in Multi-Converter Model

Participation factor analysis was performed, in line with the eigenvalue analysis, to assess controllers' sensitivity in a multi-VSC system with $n = 2$ VSCs, as previously examined. This enables the identification of the dynamic states which

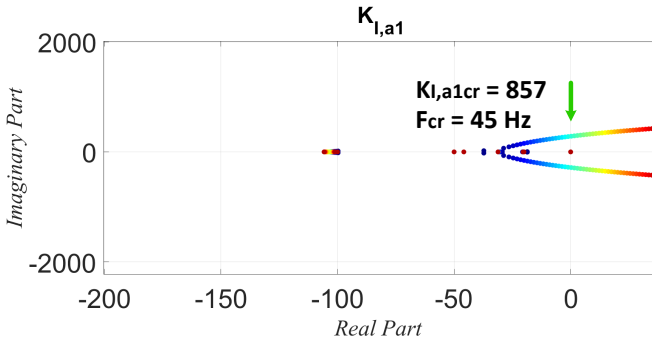
3.5. Small-Signal Analysis in Multi-Converter System



(a) Eigenvalue trace of current controller's proportional gain ($K_{P,CC}$) variation from 0.1 (deep blue) to 10 (deep red) times $K_{P,CC0}$



(b) Eigenvalue trace of PLL's proportional gain ($K_{P,PLL}$) variation from 0.1 (deep blue) to 20 (deep red) times $K_{P,PLL0}$



(c) Eigenvalue trace of AVC's integral gain ($K_{I,A}$) variation from 0.1 (deep blue) to 200 (deep red) times $K_{I,A0}$

Fig. 3.17: Eigenvalue-based stability analysis in a system with $n = 2$ VSCs for a weak grid case scenario ($SCR = 1.5$) where $\omega_{AVC,LPF}$ is set at 50 rad/s. The critical bandwidth of the current controller, the PLL and the AVC in VSC_1 is identified after the corresponding gains vary. Red arrow means instability. Source: [J3].

are most critical to the instability of the identified eigenvalue modes [J3]. The participation factors were normalized to ensure their cumulative sum is unity in each scenario. Here, dynamic states labeled with "1" pertain to VSC_1 , and those labeled "2" are associated with VSC_2 . Since each VSC system includes 20 dynamic states, 40 dynamic states are analyzed with $n = 2$ VSCs.

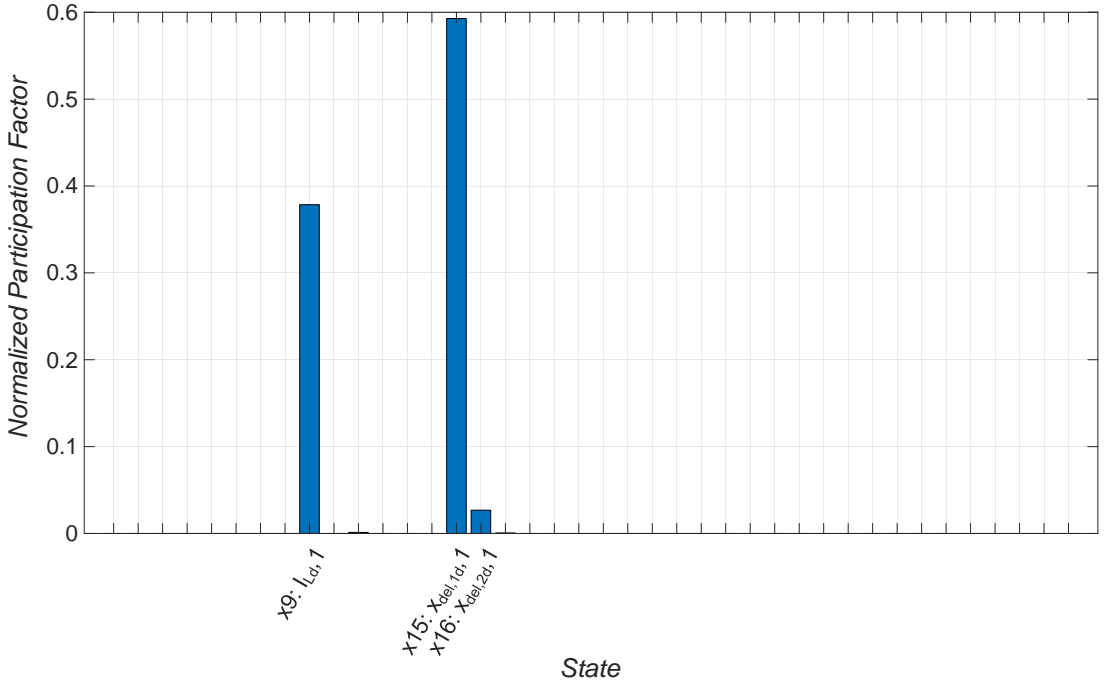


Fig. 3.18: Participation factors for critically unstable mode during variations of $K_{P,CC1}$. The critically unstable mode can be seen in the eigenvalue analysis shown in Fig. 3.17a. Source: [J3].

First, the participation factor analysis has been conducted for the case where variations in current controller's gain $K_{P,CC1}$ of VSC_1 led to instability in a system mode, as illustrated in Fig. 3.17a. The results depicted in Fig. 3.18 highlight the significance of the dynamics of the time delay in VSC_1 and the current I_{L1} on the d-axis to the instability within the super-synchronous range. As mentioned in subsection 2.2.3, the time delay is part of the current controller's

3.5. Small-Signal Analysis in Multi-Converter System

loop, and is proven to be the major cause of instability following alterations to the controller's design.

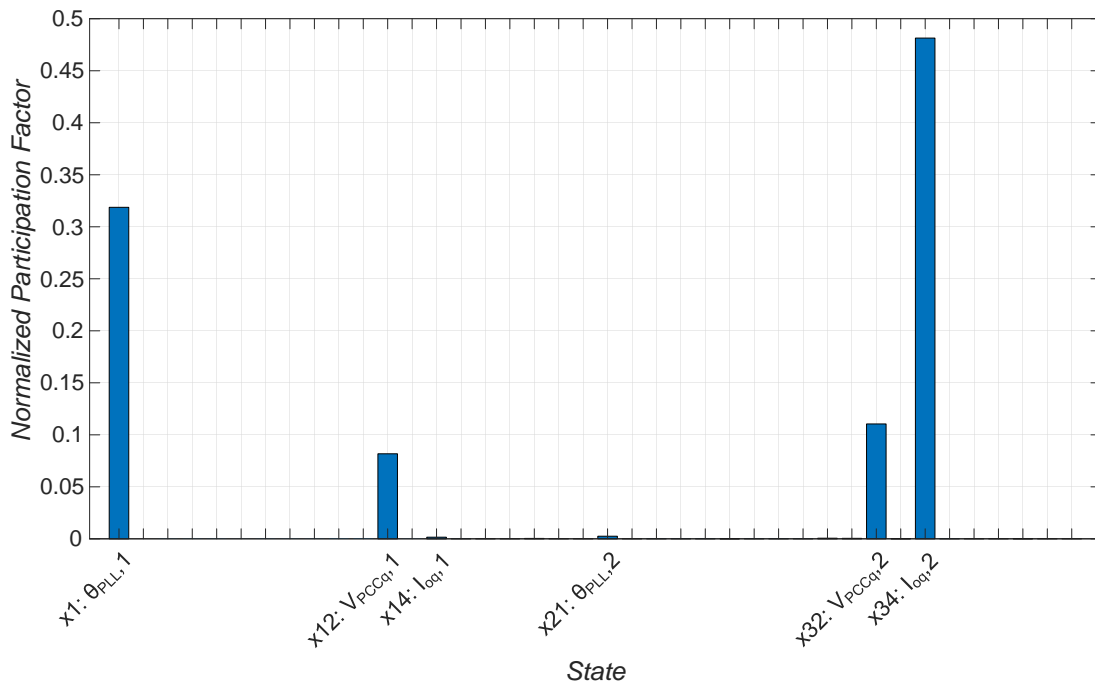


Fig. 3.19: Participation factors for critically unstable mode during variations of $K_{P,PLL1}$. The critically unstable mode can be seen in the eigenvalue analysis shown in Fig. 3.17b. Source: [J3].

Subsequently, the same approach was applied to a mode whose stability was affected by variations in the PLL's gain $K_{P,PLL1}$ of VSC_1 , as presented in Fig. 3.17b; the corresponding participation factor analysis is illustrated in Fig. 3.19. Here, the dynamic states of the θ_{PLL1} and the q-axis voltage V_{PCCq1} , representing the PLL's output and input in VSC_1 's control system, respectively, evidently impacted the mode's stability. Nevertheless, the most substantial impact was from the q-axis output current $I_{oq,2}$ in VSC_2 's control system. This indicates that the instability is a result of interactions between the control system of the two VSCs, particularly when synchronization between the multi-VSC

system and the grid is impacted due to alterations in the PLL bandwidth of one VSC.

Finally, in the case of the mode whose stability was influenced by variations in AVC's integral gain $K_{I,a1}$ of VSC_1 , as presented in Fig. 3.17c, the corresponding participation factor analysis is shown in Fig. 3.20. In this case, the dynamic states related to the AVC controller in VSC_1 play a dominant role in the instability of the system's mode under study.

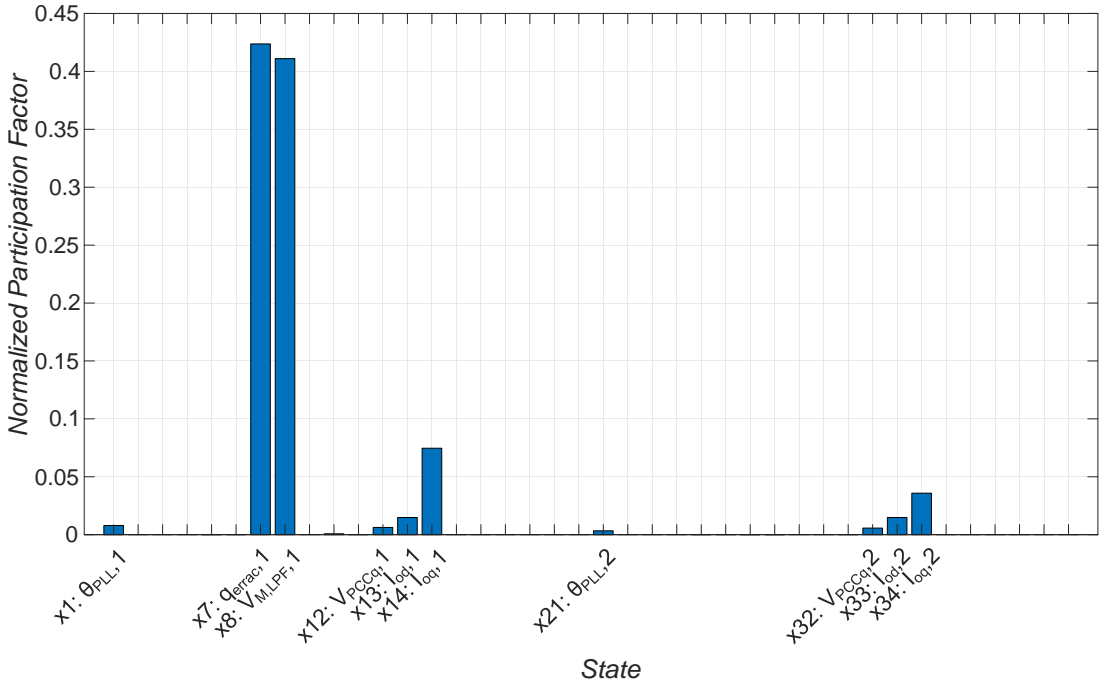


Fig. 3.20: Participation factors for critically unstable mode during variations of $K_{I,a1}$. The critically unstable mode can be seen in the eigenvalue analysis shown in Fig. 3.17c. Source: [J3].

Time domain Analysis in Multi-Converter Model

In the time-domain analysis, a weak grid scenario was also examined, having an SCR set to 1.5. A system, as depicted in Fig. 3.15, comprising two VSCs

3.6. Conclusion

($n = 2$), was subjected to time-domain simulations. To pinpoint when instability arises, a small step or ramp change was introduced to the control gain of the controller being tested in one VSC. At the beginning of instability, an FFT analysis was carried out to confirm that the dominant frequency aligns with the critical frequency determined from the corresponding eigenvalue-based stability study.

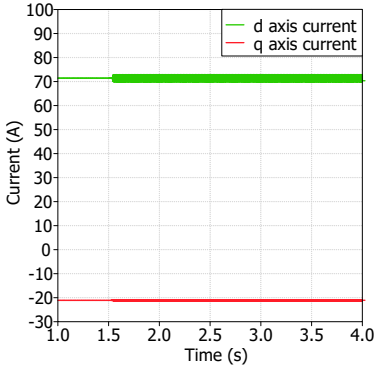
First, a step change was done to the proportional gain of the current controller $K_{P,CC1}$ to bring the instability in the high-frequency range into focus. Instability in the system was observed when this alteration brought forth a critical proportional gain value tagged at $K_{P,CC1cr} = 99.9$. In this case, the dominant frequency associated with instability was identified to be 3.34 kHz . The indication of this instability, both in time and frequency domains, is illustrated in Fig. 3.21a and Fig. 3.21b.

Then, simulations were run to observe subsynchronous resonances prompted by both the PLL and the AVC in a single VSC. By increasing the PLL proportional gain $K_{P,PLL1}$, the bandwidth where the system is led towards subsynchronous resonance was recognized. The critical gain here $K_{P,PLL1cr}$ was determined to be 2.55, with the PLL's bandwidth matching 113.37 Hz . The associated dominant oscillation frequency leading to instability was equal to 182 Hz . These results are shown in Fig. 3.21c and Fig. 3.21d. Similarly, adjustments were made to the AVC by imposing a ramp change on its integral controller $K_{I,a1}$. The instability's critical gain was seen at $K_{I,a1cr} = 750$, paired with an oscillation frequency of 44 Hz . These findings can be seen in Fig. 3.21e and Fig. 3.21f.

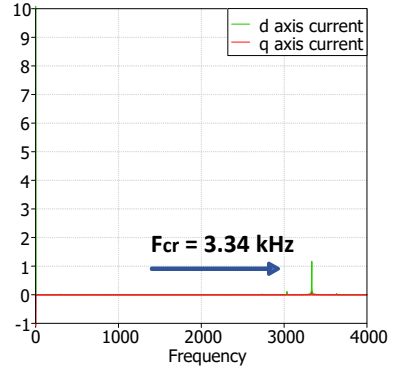
The results obtained here closely align with those presented in the corresponding eigenvalue-based stability analysis. In that section, a stability assessment of the small-signal model with n VSCs was conducted. A summary of all these findings is provided in Table 3.2. From the analysis, it was determined that the interactions influenced by each control loop were accurately captured by the model.

3.6 Conclusion

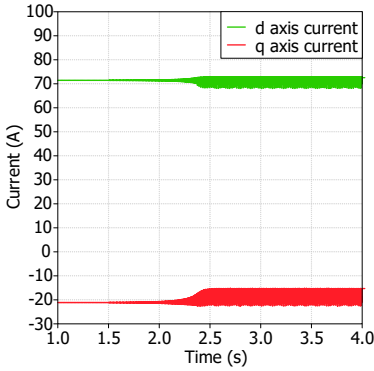
In this chapter, the effects of the AVC on a grid-connected VSC of a wind turbine were analyzed under varying grid strength scenarios, as defined by the SCR values of the power system. A nonlinear state-space model of a grid-following



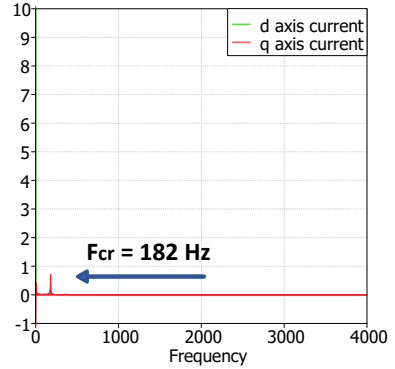
(a) Step change in current controller's proportional gain - $K_{P,CCcr} = 99.9$



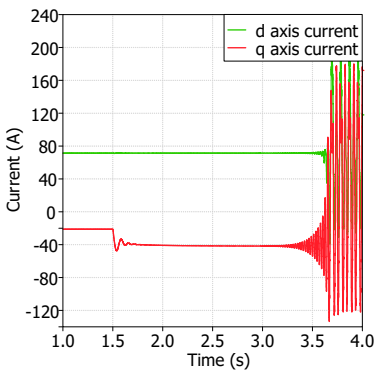
(b) Dominant oscillation frequency when high frequency range instability is caused by step change in $K_{P,CC}$



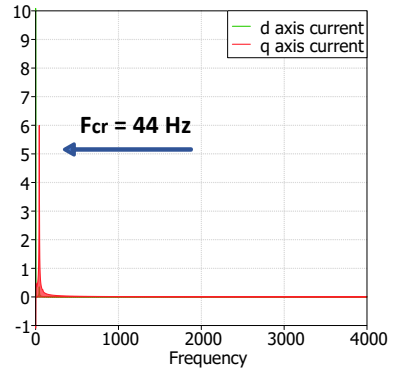
(c) Step change in PLL's proportional gain - $K_{P,PLLcr} = 2.55$



(d) Dominant oscillation frequency when low frequency range instability is caused by step change in $K_{P,PLL}$



(e) Ramp change in current controller's proportional gain - $K_{I,acr} = 750$



(f) Dominant oscillation frequency when low frequency range instability is caused by ramp change in $K_{I,a}$

Fig. 3.21: Time domain simulations and frequency analysis (FFT) of the multi-VSC inductor current I_L with $n=2$ VSCs. The stability impact of the current controller, the PLL and the AVC in the weak grid ($SCR = 1.5$) is observed, caused after the step/ ramp change in $K_{P,C0}$, $K_{P,PLL0}$ and $K_{I,A0}$ at $t=1.5$ s. The dominant oscillation frequency is shown when the control gains under study obtain their critical value. Source: [J3].

3.6. Conclusion

Table 3.2: Critical control gain with oscillation frequency in eigenvalue-based stability analysis and time domain analysis for a multi-VSC grid-connected system with $n = 2$ VSCs. Source: [J3].

	Eigenvalue-based analysis	Time domain analysis
<i>Current Controller</i>	$K_{P,CC1cr}=104.2$ $F_{cr}=3.34$ kHz	$K_{P,CC1cr}=99.9$ $F_{cr}=3.34$ kHz
<i>PLL</i>	$K_{P,PLL1cr}=2.4759$ $F_{cr}=187$ Hz	$K_{P,PLL1cr}=2.55$ $F_{cr}=182$ Hz
<i>AVC</i>	$K_{I,a1cr}=857$ $F_{cr}=45$ Hz	$K_{I,a1cr}=750$ $F_{cr}=44$ Hz

VSC was designed, incorporating the AVC controller's state-space submodel. The model's stability was evaluated using an eigenvalue-based stability analysis. Consequently, the traces of the calculated eigenvalues were examined, providing clear insights into the stability implications of each controller for different values of $f_{AVC,LPF}$.

The findings highlight that an increase in $f_{AVC,LPF}$ from 20 to 100 Hz causes a decrease in the critical AVC bandwidth in both the strong and weak grid case scenarios, although the alteration is not very significant in the weak grid scenario. At the same time, the oscillation frequency corresponding to the critical instances of instability is increased. On the other hand, the amplification of $f_{AVC,LPF}$ is found to decrease the critical PLL bandwidth in the weak grid case scenario. The oscillation frequencies corresponding to these critical PLL bandwidth instances of instability exhibit a notable trajectory; they decrease when $f_{AVC,LPF}$ is adjusted from 20 to 50 Hz, and subsequently increase until $f_{AVC,LPF}$ attains a value of 100 Hz. In the context of a strong grid, it is observed that variations in the PLL bandwidth do not affect the system's stability, even when $f_{AVC,LPF}$ undergoes variations. Time domain simulations were then conducted, and these were supplemented with FFT analysis. This methodology effectively substantiates the validity of the conclusions drawn in this research.

To conclude, a multi-VSC small-signal model was formulated, building on the previously constructed small-signal model with the AVC controller. As the single VSC model's stability characteristics were previously affirmed across various tests, further stability assessments were performed on the multi-VSC model, by utilizing both eigenvalue analysis and time-domain simulations. This was

undertaken to depict the stability effects in different frequency ranges. For this purpose, the current controller, PLL, and AVC of one VSC were tested for their sensitivity within a multi-converter framework, and the accuracy of the dynamic models was ascertained to be notably high. The stability analysis results were also enhanced by corresponding participation factor analysis which identified the most influential states on the system modes which became unstable in each case. That study could be further expanded into more complicated models of multi-VSCs, as it could reveal dynamic phenomena that could possibly be overlooked if an aggregated modelling approach was utilized. The level of complexity should also be considered in order to minimize possible future obstacles in such an analysis, such as the computational time, and at the same time ensure that the eigenvalues that correspond to the critical modes for the system's stability are included.

Similarly to Chapter 2, the current study focuses on VSCs operating at a low power level, specifically 30 kW for each unit. The purpose was to simplify the modeling process and to facilitate possible later laboratory experiments. Nevertheless, the high number of validated simulation results confirms the usefulness of the conclusions drawn, thus laying a solid foundation for the stability analysis of more large-scale systems to be explored in the next chapter.

Chapter 4

Modeling and Mitigation of Subsynchronous Oscillations in Wind Farms

4.1 Background

In previous chapters the grid side wind turbine dynamics have been investigated, primarily concentrating on small-signal stability. The weak grid case was thoroughly studied in many operational conditions, where subsynchronous oscillations (SSOs) were observed. In this chapter, the SSOs are studied at the wind farm level, where the installation of a Synchronous Condenser (SC) is investigated as a mitigation solution.

As indicated in the introduction, the SCs have become quite interesting in recent years as a mitigating measure of SSOs due to their capability to provide both voltage control and reactive power injection [94], [95]. However, the optimal power rating of SCs, which is vital for the mitigation of existing dynamic phenomena and in the prevention of new ones occurring after SCs are deployed, has not been widely discussed. Also, the influence of the SC power rating has been insufficiently explored. The aim in Chapter 4 is to analyze the pivotal role of the power rating of SCs in such dynamic phenomena.

Here, an analytical small-signal model of a wind farm based on the HVAC CIGRE benchmark model is first designed [46], where an aggregated modeling of grid-connected converters is utilized. This model describes the dynamics

of converters and passive elements through state equations. To validate the model's accuracy, eigenvalue analysis is employed on its controllers - similarly to the applied methods in Chapters 2 and 3 - and after the validation, the state-space model of the synchronous condenser is integrated. This chapter discusses the impact of the synchronous condenser on mitigating unwanted low-frequency oscillations under weak-grid conditions. A key contribution of this discussion is the identification of minimum and maximum SC ratings, which are critical in determining the mitigation of low-frequency oscillations and the emergence of new dynamic phenomena, respectively [J2].

4.2 Wind Farm's Small-Signal Model with HVAC Connection

The case under study is derived from the HVAC CIGRE benchmark model for a wind farm [46]. This model is a product of the collaborative efforts within the CIGRE working group C4.49, entitled "Multi-frequency stability of converter-based modern power systems." The primary intent of this benchmark power system is to serve as a standard for exploring interactions both between converters and between converters and the grid. In this wind farm model, aggregated Power Generation Units (PGUs), connected to an AC power grid, are taken into consideration. Specifically, the model incorporates PGUs amounting of a total of 240 MW—comprising 20 units, each of 12 MW [46]. These are employed in the developed small-signal model as depicted in Fig 4.1; the equivalent structure featuring the aggregated grid-following converter control is illustrated in Fig 4.2.

4.2.1 Aggregated Wind Turbine Model

The aggregated wind turbine model employed here operates under the control structure illustrated in Fig. 4.3. To simplify the analysis, the mechanical system of the wind turbines is omitted from consideration in this scenario. The approach to the converter control structure is influenced by the concepts presented in Chapter 2, incorporating a grid-following converter control that employs vector current control. The addition of Active Damping (AD) control is an adaptation aimed to enhance the system stability in the context of weak or highly dynamic grids. A PLL facilitates the synchronization between the converter and the

4.2. Wind Farm's Small-Signal Model with HVAC Connection

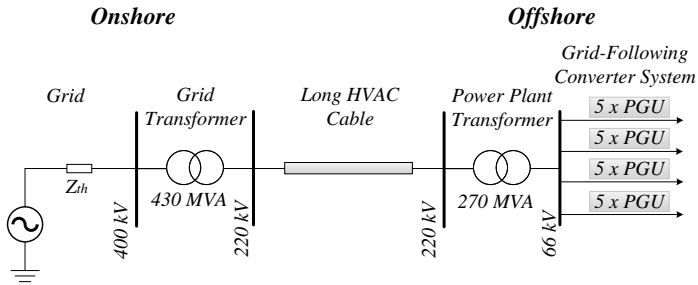


Fig. 4.1: Wind farm model with aggregated Power Generation Units (PGUs) connected to a Thevenin equivalent grid. Source: [J2].

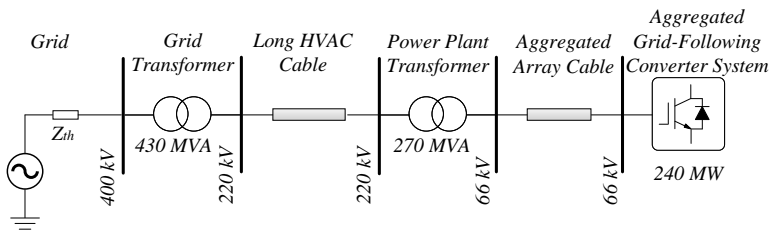


Fig. 4.2: Aggregated grid following converters connected to a Thevenin equivalent grid including cables. Source: [J2].

grid; therefore, the grid and the control dq frame are utilized, a control process discussed in detail in Section 2.2.1. An ideal converter is assumed in this model, with the DC link voltage of the inverter being constant and the reference output current established as default. This implies also that the outer-loop control is not taken into account in this simplified representation [J2].

4.2.2 HVAC Transmission System Model

The passive components between the VSC and the grid include cables, transmission lines and step-up transformers, and their modelling is presented below and also in [J2].

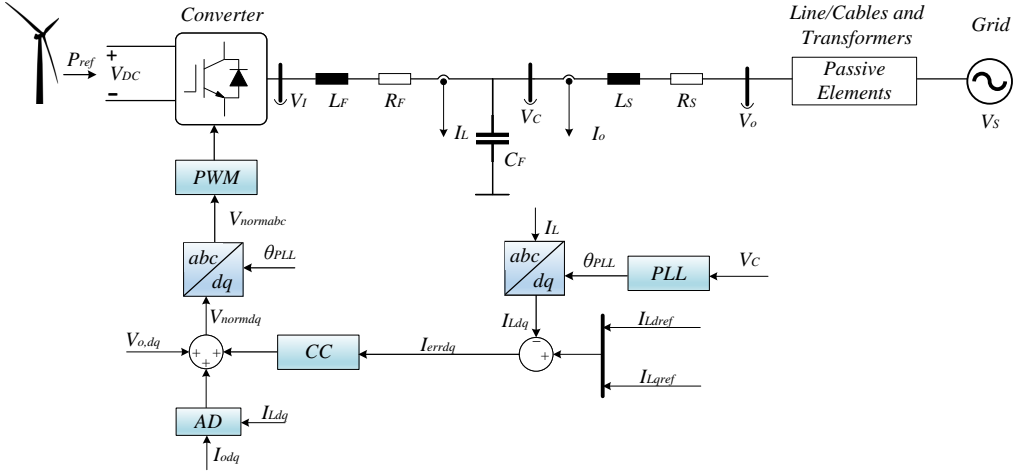


Fig. 4.3: Control structure of a simplified aggregated wind turbine model with grid-following converter using a PLL for synchronization. Source: [J2].

Transmission Line and Cable Modelling

Lines and cables are crucial, given their significant contribution to the system impedance. Their main difference is that cables possess a capacitance, causing the system resonance to be at lower frequencies compared to lines [110]. For both cables and lines, a nominal pi model is employed for state-space representation, as illustrated in Fig. 4.4. Here, R_1 and L_1 are the elements of the model's lumped impedance, and the model's shunt admittance is divided into two equal parts (C_1 and C_2) and placed at the two ends. For accurate modeling of the transmission line, an adequate number of pi-sections is utilized, enhancing the precision of the model [110].

Two different cable types are utilized for formulating the array cable; the 500 mm^2 3-core cable and the 150 mm^2 3-core cable. Each cable string integrates five PGUs. The 500 mm^2 3-core cable is employed for the first three PGUs, while the 150 mm^2 3-core cable is used for the remaining two, and the cable length between the PGUs in the cable string is equal to 5 km. In addition, when formulating the transmission cable, ten pi-sections of the 1200 mm^2 HVAC cable are employed [46]. The array cable and HVAC cable parameters utilized in the

4.2. Wind Farm's Small-Signal Model with HVAC Connection

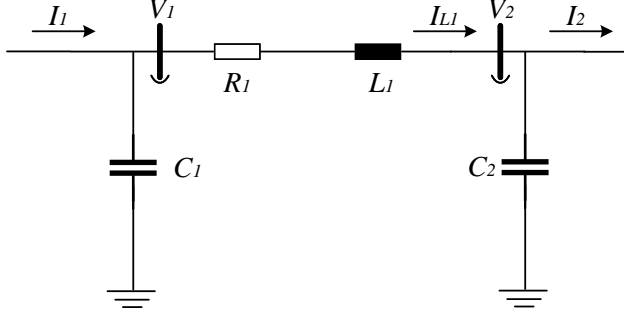


Fig. 4.4: A nominal pi-section utilized for cable and transmission line modelling (Passive Elements in Fig. 4.3). Source: [J2].

model under study are depicted in Table 4.1.

The state equations correlating to the nominal pi model of Fig. 4.4 in the dq domain can be presented as:

$$\dot{V}_{1d} = \frac{1}{C_1} I_{1d} + \left(-\frac{1}{C_1} I_{L1d} \right) + \omega_n V_{1q} \quad (4.1)$$

$$\dot{V}_{1q} = \frac{1}{C_1} I_{1q} + \left(-\frac{1}{C_1} I_{L1q} \right) - \omega_n V_{1d} \quad (4.2)$$

$$\dot{I}_{L1d} = -\frac{R_1}{L_1} I_{L1d} + \left(-\frac{1}{L_1} V_{2d} \right) + \omega_n I_{L1q} + \frac{1}{L_1} V_{1d} \quad (4.3)$$

$$\dot{I}_{L1q} = -\frac{R_1}{L_1} I_{L1q} + \left(-\frac{1}{L_1} V_{2q} \right) - \omega_n I_{L1d} + \frac{1}{L_1} V_{1q} \quad (4.4)$$

$$\dot{V}_{2d} = \frac{1}{C_2} I_{L1d} + \left(-\frac{1}{C_2} I_{2d} \right) + \omega_n V_{2q} \quad (4.5)$$

$$\dot{V}_{2q} = \frac{1}{C_2} I_{L1q} + \left(-\frac{1}{C_2} I_{2q} \right) - \omega_n V_{2d} \quad (4.6)$$

where ω_n is the nominal angular frequency corresponding to 50 Hz.

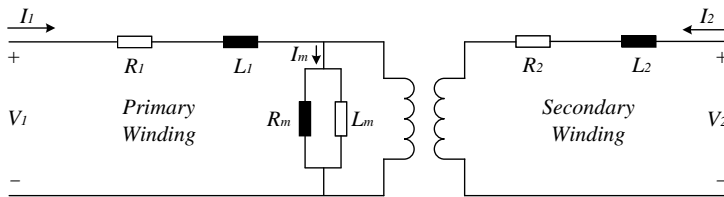
Transformer Model

The transformer serves as a passive component, facilitating the long-distance power transfer through magnetic coupling between different voltage levels; its

Table 4.1: Cable Parameters used for the wind farm system in Fig. 4.2 [46].

500 mm² Array Cable 66 kV	
Description	Value
Inductance	0.34 mH/km
Resistance	0.06 Ω/km
Capacitance	0.29 μF/(km/2)
150 mm² Array Cable 66 kV	
Description	Value
Inductance	0.41 mH/km
Resistance	0.14 Ω/km
Capacitance	0.19 μF/(km/2)
1200 mm² HVAC Cable 220 kV	
Description	Value
Inductance	0.406 mH/km
Resistance	0.047 Ω/km
Capacitance	0.208 μF/(km/2)

classical model is illustrated in Fig. 4.5.

**Fig. 4.5:** Classical transformer equivalent model with lumped parameters (Passive Elements in Fig. 4.3). Source: [J2].

Given the large magnetization inductance L_m in Fig. 4.5, the magnetizing branch draws minimal excitation current I_m and can often be neglected. Consequently, the winding resistances (R_1 and R_2) and reactances (L_1 and L_2) in Fig. 4.5, now in series, are combined into the transformer's equivalent resistance R_{eq} and reactance L_{eq} , viewed from its respective side. The equivalent circuit of the transformer, representing the transformer's elements as referenced to the

4.2. Wind Farm's Small-Signal Model with HVAC Connection

primary side, is displayed in Fig.4.6.

Below are the state equations of the transformer's equivalent model of Fig. 4.6 in the dq system:

$$\dot{I}_{1d} = -\frac{R_{eq}}{L_{eq}} I_{1d} + \left(-\frac{1}{L_{eq}} V'_{2d} \right) + \omega_n I_{1q} + \frac{1}{L_{eq}} V_{1d} \quad (4.7)$$

$$\dot{I}_{1q} = -\frac{R_{eq}}{L_{eq}} I_{1q} + \left(-\frac{1}{L_{eq}} V'_{2q} \right) - \omega_n I_{1d} + \frac{1}{L_{eq}} V_{1q} \quad (4.8)$$

where V'_{2dq} is the secondary terminal voltage V_2 of the transformer referred to the primary side in the dq axis system, and ω_n the nominal angular frequency corresponding to 50 Hz.

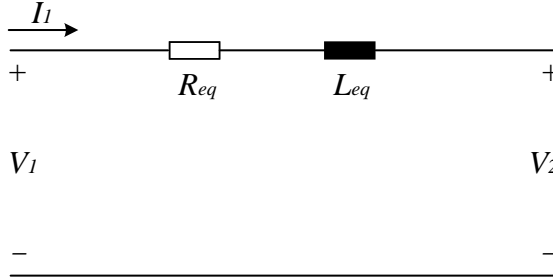


Fig. 4.6: Transformer equivalent model reflected to one voltage level after neglecting the magnetizing branch. Source: [J2].

To enhance power transmission from the wind farm to the shore, the voltage undergoes multiple voltage elevations, from 0.69 kV at the wind turbine terminals to the typical grid connection point at transmission level for a nominal voltage of 400 kV. Likewise, the step-up transformer of the SC is modelled to elevate the voltage from 26 kV to 220 kV. The respective transformer parameters are specified in Table 4.2.

Table 4.2: Transformer Parameters used for the wind farm system in Fig. 4.2 [46]. The synchronous condenser transformer is later included in the system, as shown in Fig. 4.19.

Grid Transformer	
Description	Value
Voltage Ratio (kV/kV)	400/220
Rated Power (MVA)	430
Inductance (H)	0.12
Resistance (Ω)	0.0014
Power Plant Transformer	
Description	Value
Voltage Ratio (kV/kV)	220/66
Rated Power (MVA)	270
Inductance (H)	0.12
Resistance (Ω)	0.0025
PGU Transformer	
Description	Value
Voltage Ratio (kV/kV)	66/0.69
Rated Power (MVA)	240
Inductance (H)	0.0261
Resistance (Ω)	0.0054
Synchronous Condenser Transformer	
Description	Value
Voltage Ratio (kV/kV)	26/220
Rated Power (MVA)	270
Inductance (H)	0.14
Resistance (Ω)	20

4.2.3 Wind Farm Model Accuracy through Eigenvalue-Based Stability Analysis

An eigenvalue analysis based on small-signal models of the whole system is depicted for the controllers of the aggregated wind turbine model from Fig. 4.3 to evaluate the model's accuracy. This procedure is important, as the incorporation of an SC will then be allowed [J2]. The corresponding system and control parameters of the system under study are shown in Table 4.3, where the PLL's

4.2. Wind Farm's Small-Signal Model with HVAC Connection

Table 4.3: System and Control Parameters of Converter System. Source: [J2], [46].

	Description	Value
f_{sw}	Switching Frequency	2950 Hz
f_S	Sampling Frequency	5900 Hz
S_b	Rated Power (Aggr. System)	240 MW
V_b	L-L RMS Voltage	690 V
L_F	Filter Inductance	0.1056 pu
R_F	Filter Resistance	0.0053 pu
C_F	Filter Capacitance	0.0757 pu
L_S	Output Inductance	0.0261 pu
R_S	Output Resistance	0.0054 pu
$K_{I,CC0}$	Default Integral Gain of Current Control	0.1246
$K_{P,CC0}$	Default Proportional Gain of Current Control	0.0004
K_D	Active Damping Gain of Current Control	0.0004
K_{FFV}	Feedforward Gain of Current Control	1
$K_{I,PLL0}$	Default Integral Gain of PLL	0.9106
$K_{P,PLL0}$	Default Proportional Gain of PLL	0.0455

bandwidth is set at a lower frequency of 11.95 Hz in order to mitigate high-order harmonics. The current controller's bandwidth is set at 133 Hz, which is approximately 1/20 of the switching frequency f_{sw} , and the operating power is equal to 240 MW, which is the nominal power of the aggregated system.

Eigenvalue Analysis for Current Controller's Control Parameters

Firstly, the sensitivity of the current controller is examined. Controller gains are ranged from 1 (deep blue) to 15 (deep red) times the controller's default value shown in Table 4.3. Fig. 4.7 illustrates the pair of instability eigenvalues, where the corresponding critical gain $K_{PCC,cr}$, the critical oscillation frequency $F_{oscill,cr}$, and the controller's bandwidth $CC\ BW$ of the unstable mode are highlighted. Observations from the eigenvalue trajectories reveal that increasing the proportional gain of the current controller results in system instability.

To corroborate the dynamic response of the small-signal model, electromagnetic transient (EMT) simulations are executed, applying a step change to the default proportional gain of the CC K_{PCC0} at $t = 3$ seconds, during operation

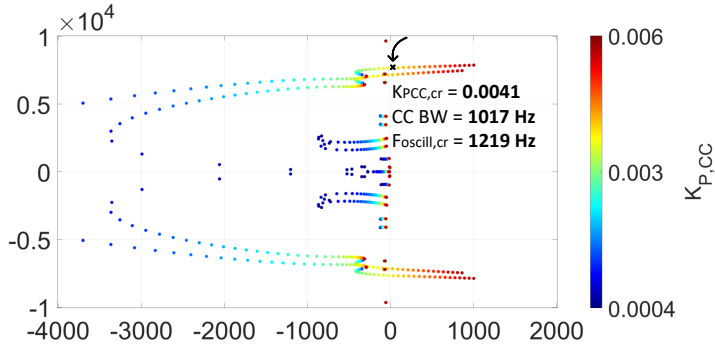


Fig. 4.7: Eigenvalue-based stability analysis—trajectories for CC's proportional gain are shown. Source: [J2].

of a state of system stability. The altered controller's gain reached a critical value impacting system stability ($K_{PCC,cr} = 0.0042$), utilizing the filter current I_L in the dq frame to illustrate the instability. Fig. 4.8 and Fig. 4.9 depict the simulated outcomes, portraying $K_{PCC,cr}$ and the predominant oscillation frequency identified from the FFT analysis ($F_{dom} = 1220$ Hz). The time-domain simulations align very well with the CC's eigenvalue analysis in Fig. 4.7.

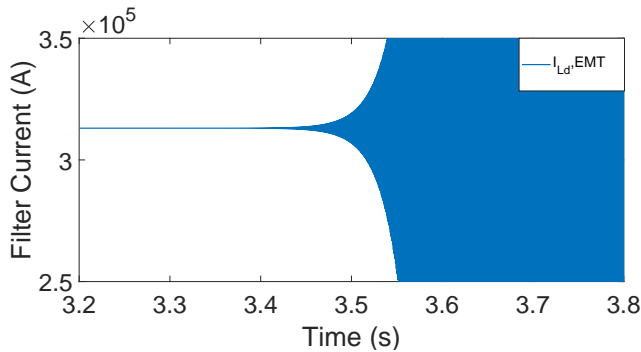


Fig. 4.8: Time domain simulations of the filter current I_{Ld} when $K_{PCC} = K_{PCC,cr}$ at $t = 3$ seconds. Source: [J2].

4.2. Wind Farm's Small-Signal Model with HVAC Connection

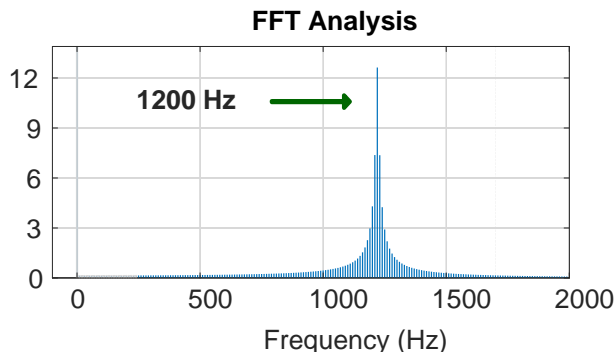


Fig. 4.9: FFT Analysis of the filter current I_{Ld} when $K_{PCC}=K_{PCC,cr}$ at $t = 3$ seconds (see Fig. 4.8). Source: [J2].

Eigenvalue Analysis for PLL's Control Parameters

The sensitivity of the PLL is then assessed. The controller gains here range from 0.1 (deep blue) to 10 (red) times the controller's default value shown in Table 4.3. Fig. 4.10 displays the pair of instability eigenvalues, highlighting the corresponding critical gain $K_{PPLL,cr}$, the critical oscillation frequency $F_{oscill,cr}$, and the PLL's bandwidth $PLL BW$ of the unstable mode. The observations from the eigenvalue analysis indicate the beginning of instability in the system with an increase in the proportional gain of the PLL.

To confirm the dynamic response of the small-signal model, another set of EMT simulations are performed. A step change is applied to the default proportional gain of the PLL K_{PPLL0} at $t = 3$ seconds, when the system is stable. The controller's gain reached a critical level ($K_{PPLL,cr} = 0.1821$), impacting the system stability, and the filter current I_L in the dq frame is used to depict the instability scenario. The simulation results, illustrated in Fig. 4.11 and Fig. 4.12, show $K_{PPLL,cr}$ and the corresponding dominant oscillation frequency from the FFT analysis ($F_{dom} = 47$ Hz). Again, the time-domain simulations closely mirror the eigenvalue analysis of the PLL. Hence, the precision of the wind farm's small-signal model allows the incorporation of the SC state-space submodel in order to assess the whole system.

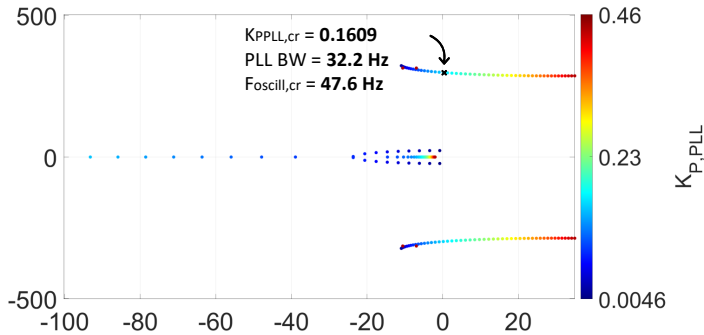


Fig. 4.10: Eigenvalue-based stability analysis—trajectories for PLL’s proportional gain are shown. Source: [J2].

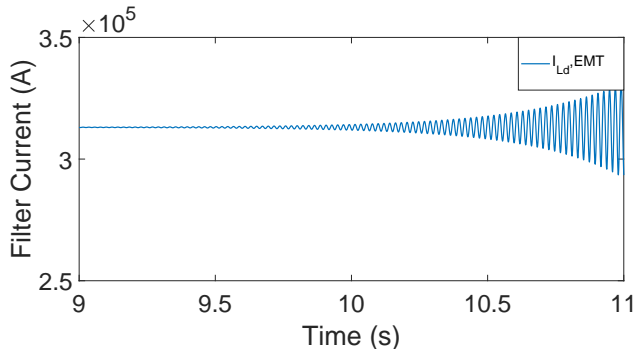


Fig. 4.11: Time domain simulations of the filter current I_{Ld} when $K_{P,PLL} = K_{P,PLLcr}$ at $t = 3$ seconds. Source: [J2].

4.3 Mitigation of Subsynchronous Oscillations with Synchronous Condenser

The SC is essentially a type of synchronous machine that operates without any mechanical drive, meaning there is no prime mover involved. As such, the SC is not able to generate active power, with the mechanical torque T_m being zero, but it has the ability to control reactive power through regulating its excitation. As noted earlier, the SC, unlike other compensatory devices such as SVC and

4.3. Mitigation of Subsynchronous Oscillations with Synchronous Condenser

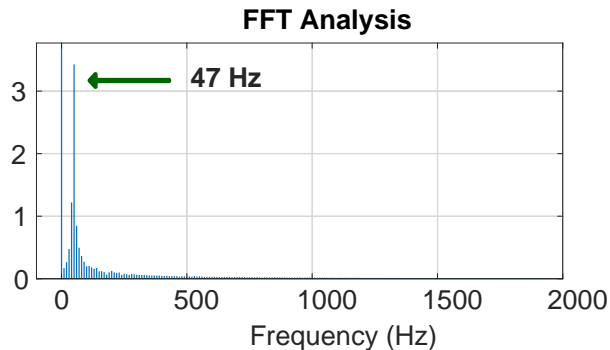


Fig. 4.12: FFT Analysis of the filter current I_{Ld} when $K_{P,PLL}=K_{P,PLLcr}$ at $t = 3$ seconds (see Fig. 4.11). Source: [J2].

STATCOM, possesses the capability to increase the SCR of the power system [95].

4.3.1 Synchronous Condenser's State-Space Model

The SC's state-space model is formulated from the Synchronous Generator and Automatic Voltage Regulator (AVR) sub-models, both of which are presented in [J2]. Fig. 4.13 shows the state-space representation of the SC, depicting its connection to the power system. The parameters of the SC model are defined and outlined in Table 4.4, and the relations between the synchronous generator's inductances are defined in Table 4.5. Here, the parameters of the synchronous generator are presented in a per unit (pu) system, while the SC's power rating S_N is used to express the generator's parameters in the International System of Units (SI) [J2]. The value of S_N is varied in the test cases of the following subsections, determining the SC's stability impact.

Synchronous Generator Model

The primary windings of the generator are the stator and field windings. The rotor also contains a set of damper windings, where during steady states no current flows. Thus, the damper circuits are closed circuits with no external voltage applied, and experience induced currents only when there is a change in

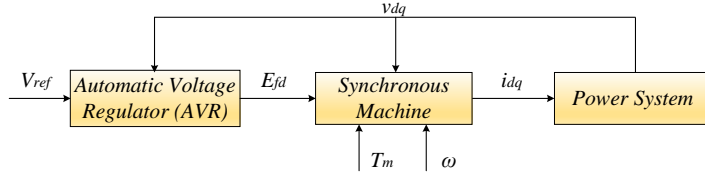


Fig. 4.13: System diagram of a Synchronous Condenser connected to a power system including a grid-connected offshore wind farm. Source: [J2].

Table 4.4: Parameters of a Synchronous Generator and Automatic Voltage Regulator (AVR) used in a Synchronous Condenser. The rating S_N depends on the case under study. Source: [J2].

	Description	Value
S_N	Rated Power	-
V_B	Base Voltage	26 kV
ω_b	Base Frequency	50 Hz
L_{ad}	Mutual air-gap inductance d-axis	2.1 pu
L_{aq}	Mutual air-gap inductance q-axis	2.1 pu
L_{al}	Leakage inductance in stator winding	0.35 pu
L_{fdl}	Leakage inductance in field winding	0.22 pu
L_{kd}	Leakage inductance in damper winding d-axis	0.1826 pu
L_{kq}	Leakage inductance in damper winding q-axis	0.1281 pu
D	Damping Constant	1 pu
R_a	Armature Resistance	0.007 pu
R_{fd}	Field Winding Resistance	0.0016 pu
R_{kd}	Damper Winding Resistance d-axis	0.0085 pu
R_{kq}	Damper Winding Resistance q-axis	0.0085 pu
H	Inertia	4 s
K_A	Exciter Gain	5 pu
T_A	Exciter Time Constant	0.0065 s
T_R	Transducer Time Constant	0.001 s

the magnetic field generated by the stator windings or the field winding [17].

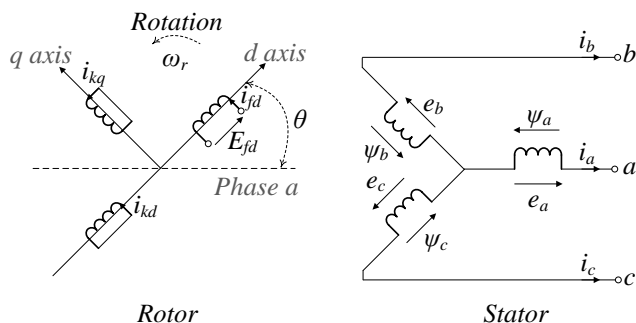
In this derivation, the field winding aligns with the d-axis, and circuits of damper winding are present in the rotor on both the d- and q-axes. Voltage is not

4.3. Mitigation of Subsynchronous Oscillations with Synchronous Condenser

Table 4.5: Synchronous Generator's Inductances relations. Source: [J2].

Inductance	Description
$L_d = L_{ad} + L_{al}$	Self inductance of d-axis stator winding
$L_q = L_{aq} + L_{al}$	Self inductance of q-axis stator winding
$L_{ffd} = L_{ad} + L_{fdl}$	Self inductance in field winding d-axis
$L_{kkd} = L_{ad} + L_{kdl}$	Self inductance in damper winding d-axis
$L_{kkq} = L_{ad} + L_{kql}$	Self inductance in damper winding q-axis

applied in the dampers, therefore they are short-circuited, as already discussed. The dynamic behavior of the synchronous machine is driven by the magnetic couplings between these windings, represented by the internal inductances [111]. Fig. 4.14 illustrates the structure of the synchronous machine and thereby the synchronous condenser.

**Fig. 4.14:** Electrical Model of Synchronous Generator with rotor and stator including excitation. Source: [J2].

Based on Fig. 4.14, the rotor winding aligns with the d-axis. The overall flux linkage equations of the synchronous machine in the dq-frame are presented below.

$$\begin{bmatrix} \psi_d \\ \psi_{fd} \\ \psi_{kd} \\ \psi_q \\ \psi_{kq} \end{bmatrix} = \begin{bmatrix} -L_d & L_{ad} & L_{ad} & 0 & 0 \\ -L_{ad} & L_{ffd} & L_{fk d} & 0 & 0 \\ -L_{ad} & L_{fk d} & L_{kkd} & 0 & 0 \\ 0 & 0 & 0 & -L_q & L_{aq} \\ 0 & 0 & 0 & -L_{aq} & L_{kkq} \end{bmatrix} \begin{bmatrix} i_d \\ i_{fd} \\ i_{kd} \\ i_q \\ i_{kq} \end{bmatrix} \quad (4.9)$$

The voltage equations of the synchronous machine, including stator voltages, field voltage and rotor voltages, are given below:

$$u_d = -R_a i_d + \frac{1}{\omega_b} \dot{\psi}_d - \omega \psi_q \quad (4.10)$$

$$u_q = -R_a i_q + \frac{1}{\omega_b} \dot{\psi}_q + \omega \psi_d \quad (4.11)$$

$$e_{fd} = R_{fd} i_{fd} + \frac{1}{\omega_b} \dot{\psi}_{fd} \quad (4.12)$$

$$u_{kd} = R_{kd} i_{kd} + \frac{1}{\omega_b} \dot{\psi}_{kd} = 0 \quad (4.13)$$

$$u_{kq} = R_{kq} i_{kq} + \frac{1}{\omega_b} \dot{\psi}_{kq} = 0 \quad (4.14)$$

From the aforementioned voltage equations, the state-space submodel of the synchronous generator can be obtained. The synchronous generator currents have to be expressed first, by employing (4.9) as:

$$[\Psi] = [\mathbf{L}][\mathbf{i}] \Rightarrow [\mathbf{i}] = [\mathbf{L}^{-1}][\Psi] \quad (4.15)$$

The current equations derived from (4.15) are as:

$$i_d = L_{[1,1]}^{-1} \psi_d + L_{[1,2]}^{-1} \psi_{fd} + L_{[1,3]}^{-1} \psi_{kd} \quad (4.16)$$

$$i_{fd} = L_{[2,1]}^{-1} \psi_d + L_{[2,2]}^{-1} \psi_{fd} + L_{[2,3]}^{-1} \psi_{kd} \quad (4.17)$$

$$i_{kd} = L_{[3,1]}^{-1} \psi_d + L_{[3,2]}^{-1} \psi_{fd} + L_{[3,3]}^{-1} \psi_{kd} \quad (4.18)$$

$$i_q = L_{[4,4]}^{-1} \psi_q + L_{[4,5]}^{-1} \psi_{kq} \quad (4.19)$$

$$i_{kq} = L_{[5,4]}^{-1} \psi_q + L_{[5,5]}^{-1} \psi_{kq} \quad (4.20)$$

4.3. Mitigation of Subsynchronous Oscillations with Synchronous Condenser

Subsequently, (4.16)-(4.20) are integrated into (4.10)-(4.14), to derive the state equations of the flux linkages. The expression h_{ij} is utilized for simplicity, where i and j denote the row and column of (4.9), respectively:

$$h_{ij} = R_i L_{i,j}^{-1} \omega_b \quad (4.21)$$

In addition to the state equations of the flux linkages, the equation of motion and the state equation of the δ angle are essential to interface the grid and the SC dq-frames.

$$\Delta \dot{\omega} = \frac{1}{2H} (\Delta T_m - \Delta T_e - D \Delta \omega) \quad (4.22)$$

$$\Delta \dot{\delta} = \omega_b \Delta \omega \quad (4.23)$$

Thus, based on [112] and [J2], the overall linearized state-space model detailing the dynamics of the synchronous generator is as follows:

$$\begin{aligned} \Delta \dot{\psi}_d &= h_{11} \Delta \psi_d + h_{12} \Delta \psi_{fd} + h_{13} \Delta \psi_{kd} + \omega_0 \omega_b \Delta \psi_q \\ &\quad + \omega_b \psi_{q0} \Delta \omega + \omega_b \Delta v_d \end{aligned} \quad (4.24)$$

$$\begin{aligned} \Delta \dot{\psi}_{fd} &= -h_{21} \Delta \psi_d - h_{22} \Delta \psi_{fd} - h_{23} \Delta \psi_{kd} + k \omega_b \Delta \omega \\ &\quad + \omega_b \Delta E_{fd} \end{aligned} \quad (4.25)$$

$$\Delta \dot{\psi}_{kd} = -h_{31} \Delta \psi_d - h_{32} \Delta \psi_{fd} - h_{33} \Delta \psi_{kd} \quad (4.26)$$

$$\begin{aligned} \Delta \dot{\psi}_q &= -\omega \omega_b \Delta \psi_d + h_{44} \Delta \psi_q + h_{45} \Delta \psi_{kq} \\ &\quad - \omega_b \psi_{d0} \Delta \omega + \omega_b \Delta v_d \end{aligned} \quad (4.27)$$

$$\Delta \dot{\psi}_{kq} = -h_{54} \Delta \psi_q - h_{55} \Delta \psi_{kq} \quad (4.28)$$

$$\Delta \dot{\delta} = \omega_b \Delta \omega \quad (4.29)$$

$$\begin{aligned} \Delta \dot{\omega} &= -\frac{a_d}{2H} \Delta \psi_d - \frac{a_{fd}}{2H} \Delta \psi_{fd} - \frac{a_{kd}}{2H} \Delta \psi_{kd} \\ &\quad - \frac{a_q}{2H} \Delta \psi_q - \frac{a_{kq}}{2H} \Delta \psi_{kq} - \frac{D}{2H} \Delta \omega \end{aligned} \quad (4.30)$$

where

$$\begin{aligned} a_d &= i_{q0} - \frac{1}{3} \psi_{q0} L_{[1,1]}^{-1}, & a_{fd} &= -\frac{1}{3} \psi_{q0} L_{[1,2]}^{-1}, \\ a_{kd} &= -\frac{1}{3} \psi_{q0} L_{[1,3]}^{-1}, & a_q &= i_{q0} - \frac{1}{3} \psi_{q0} L_{[4,1]}^{-1}, \\ a_{kq} &= \frac{1}{3} \psi_{d0} L_{[4,2]}^{-1}. \end{aligned} \quad (4.31)$$

and the steady-state flux linkages are obtained by (4.32)-(4.33):

$$\psi_{d0} = u_{q0} + R_a i_{q0} \quad (4.32)$$

$$\psi_{q0} = -u_{d0} - R_a i_{d0} \quad (4.33)$$

The steady-state operating points for voltage and current of the synchronous machine are equal to 1 pu.

Automatic Voltage Regulator (AVR) Model

The field-voltage E_{fd} is controlled by the AVR, subject to the voltage at a selected bus, thus enabling the synchronous machine to be deployed for voltage and reactive power control in the system. The voltage amplitude V_{dq} serves as an input to the AVR, and it is smoothed by a first order filter in the transducer. Additional controllers, such as a power system stabilizer (PSS) can also be included in the AVR [J2]. Fig 4.15 illustrates the configuration of the AVR.

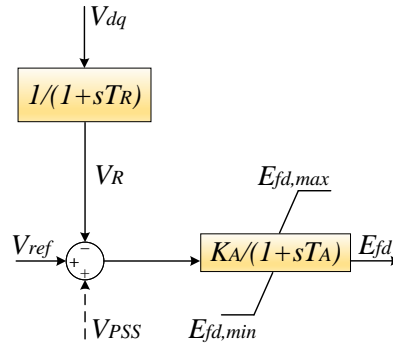


Fig. 4.15: Structure of Automatic Voltage Regulator (AVR) which controls E_{fd} in Fig. 4.14. Source: [J2].

The state variables are identified as V_R and E_{fd} , and the related state equations are given as below:

4.3. Mitigation of Subsynchronous Oscillations with Synchronous Condenser

$$\Delta \dot{V}_R = -\frac{1}{T_R} \Delta V_R + \frac{v_{d0}}{V_{t0} T_R} \Delta v_d + \frac{v_{q0}}{V_{t0} T_R} \Delta v_q \quad (4.34)$$

$$\Delta \dot{E}_{fd} = -\frac{V_{t0} K_A}{T_A} \Delta V_R - \frac{1}{T_A} \Delta E_{fd} + \frac{V_{t0} K_A}{T_A} \Delta V_{ref} \quad (4.35)$$

Modeling Validation

To corroborate the small-signal model of the SC, a small external system is formulated and the SC is integrated into it as illustrated in Fig. 4.16. The system parameters of the external system are shown in Table 4.6, and the SC parameters are those presented in Table 4.4 for a machine's power rating of 100 kVA. The state equations corresponding to the electrical elements of the external system follow the same concept as described in previous chapters, and the incorporation of the SC is implemented using the component-connection method (CCM) [70].

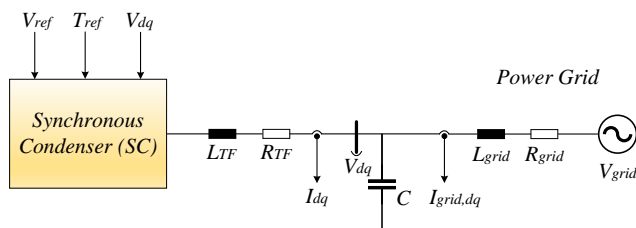
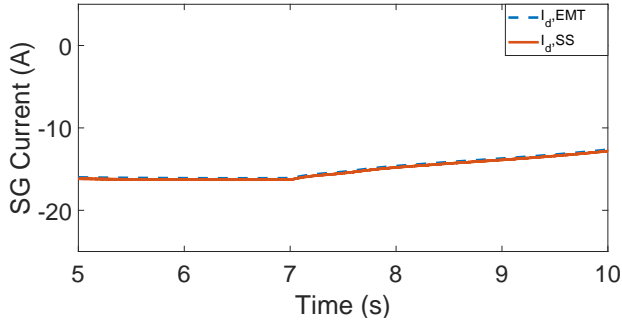
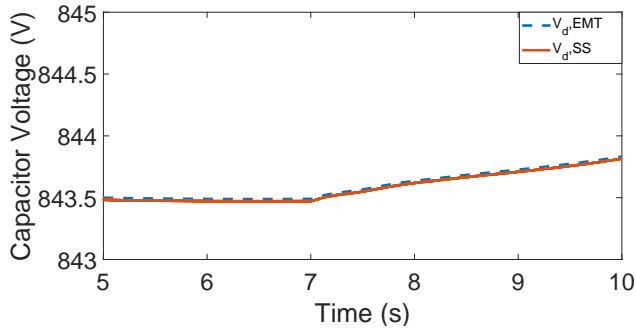


Fig. 4.16: SC connected to external power system for model validation. Source: [J2].

The validation procedure is implemented following a small step in the input reference voltage V_{ref} of the SC from 1 p.u. to 1.05 p.u. at $t = 7$ seconds. The EMT simulation is then compared with the state-space (SS) response. As evidenced in Fig. 4.17 and Fig. 4.18, the simulation outcomes of EMT and SS, relating to the current I_d and the voltage V_d , are almost the same after the minor disturbance at V_{ref} . Hence, the SC's small-signal model can be employed for the stability analysis.

Table 4.6: System Parameters of External System in Fig. 4.16 for validating the Synchronous Condenser Model. Source: [J2].

	Description	Value
V_{grid}	Grid Phase Voltage (peak value)	690 V
f_n	Rated Frequency	50 Hz
L_{TF}	Transformer Inductance	1 μ H
R_{TF}	Transformer Resistance	1 Ω
C	Filter's Capacitance	100 μ F
L_{grid}	Grid Inductance	10 nH
R_{grid}	Grid Resistance	0.1 Ω

**Fig. 4.17:** Current I_d under a step change in the reference voltage V_{ref} . Source: [J2].**Fig. 4.18:** Voltage V_d under a step change in reference voltage V_{ref} . Source: [J2].

4.3. Mitigation of Subsynchronous Oscillations with Synchronous Condenser

4.3.2 Stability Impact of Synchronous Condenser's Rating

After the corroboration of the SC's small-signal model, it becomes possible to include it into the small-signal model of the HVAC CIGRE benchmark model, as outlined in Section 4.2. In the HVAC CIGRE benchmark model, the installation of the SC takes place at the onshore substation through a step-up transformer, as illustrated in Fig. 4.19.

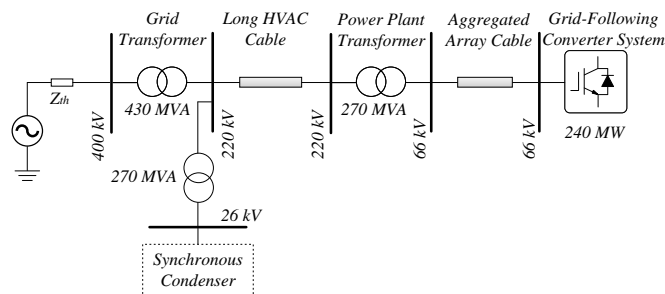


Fig. 4.19: HVAC CIGRE power system with 240 MW wind power plant and a Synchronous Condenser connected to the onshore substation. Source: [J2].

The SC is vital for reducing SSOs in the HVAC CIGRE Benchmark model. To create a scenario of a critical weak grid with dynamic instability for simulation, the SCR of the model is lowered to a critical instability value of 2.4, as defined in [113]. This results in an increased array cable impedance, forming a critical scenario where SSOs appear and the system loses stability. However, integrating the SC mitigates these SSOs, with the effectiveness of mitigation depending on the power rating of the SC, as shown in Fig. 4.20. The oscillation frequency of the SSOs is presented in Fig. 4.21.

The EMT simulation in Fig. 4.20 shows that a higher SC power rating leads to a regular and stable operation. More precisely, at a 5 MVA rating for the SC, SSOs are not mitigated, but they are at a 10 MVA rating. It is noted that approximately 10 MVA is the minimum acceptable limit for SC ratings in this test case.

However, considering the wind farm's capacity of 240 MW, the highest possible power rating of the added SC is a crucial factor for retaining the system's stability. In fact, time domain simulations have demonstrated that connecting an excessively rated SC to the wind farm's onshore substation could resolve

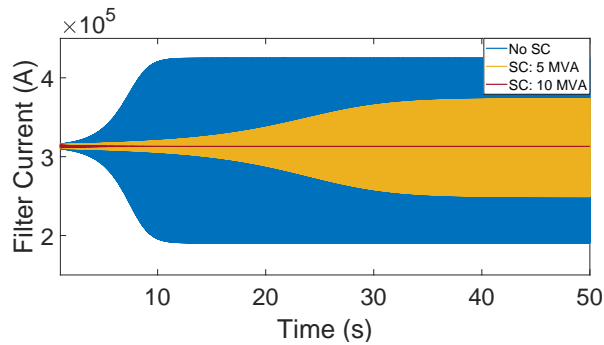


Fig. 4.20: Filter current I_{Ld} of the grid-following converter system in HVAC CIGRE benchmark model with SC when $SCR_{cr} = 2.4$ under three different cases of low SC power ratings (0, 5, 10 MVA). Source: [J2].

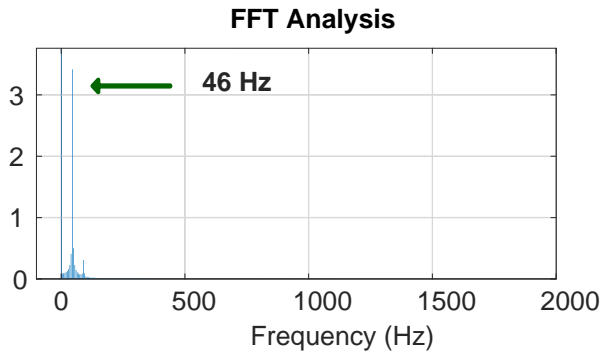


Fig. 4.21: FFT Analysis of the filter current I_{Ld} of the grid-following converter system in HVAC CIGRE benchmark model when $SCR_{cr} = 2.4$ and SSOs are not mitigated by the SC. Source: [J2].

system operations fast but might also introduce SSOs.

More specifically, Fig. 4.22 reveals that no low-frequency oscillations exist for an SC rating of 90 MVA. If the SC rating is adjusted to 110 MVA, low-frequency oscillations are detected at $t = 96$ seconds, as the EMT simulations in the same figure illustrate. Additionally, an 150 MVA SC rating destabilizes the system much faster, at around 22 seconds. This type of SSO, linked to the relatively high rating of the SC, is identified when the SC rating is at approximately 100

4.3. Mitigation of Subsynchronous Oscillations with Synchronous Condenser

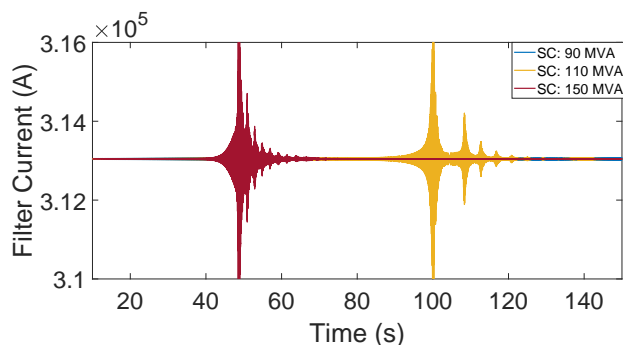


Fig. 4.22: Filter current I_{Ld} of the grid-following converter system in HVAC CIGRE benchmark model with SC when $SCR_{cr} = 2.4$ under three different cases of high SC power ratings (90, 110, 150 MVA). Source: [J2].

MVA.

Further analysis is done on the small-signal model of the HVAC CIGRE Benchmark model with the SC. Eigenvalue-based stability analysis is applied, observing the trajectory of the SC's power rating S_N .

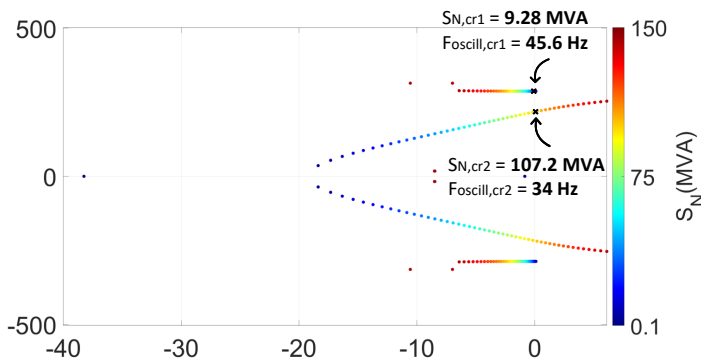


Fig. 4.23: Eigenvalue-based stability analysis—trajectories for different SC's ratings S_N . Source: [J2].

From this trajectory of S_N , it is observed that at $SCR_{cr} = 2.4$, the system is initially unstable, stabilizing when an SC of 9.28 MVA is integrated. However, escalating the SC rating to 107.2 MVA reintroduces instability. This implies

there is an acceptable range of SC ratings in MVA, defined as $S_{N,acc}$, for the critical case of the grid with an $SCR_{cr} = 2.4$, as shown below:

$$9.28 \text{ MVA} < S_{N,acc} < 107.2 \text{ MVA} \quad (4.36)$$

This observation is in harmony with the EMT simulations shown in Figs. 4.20 and 4.22, validating the small-signal model's accuracy in choosing a suitable SC to mitigate SSOs in specific critical cases of a weak grid, given that the AVR parameters remain the same. The acceptable range of SC power ratings can be visualized for all potential SCR scenarios around the critical value of $SCR_{cr} = 2.4$, as presented in Fig. 4.24.

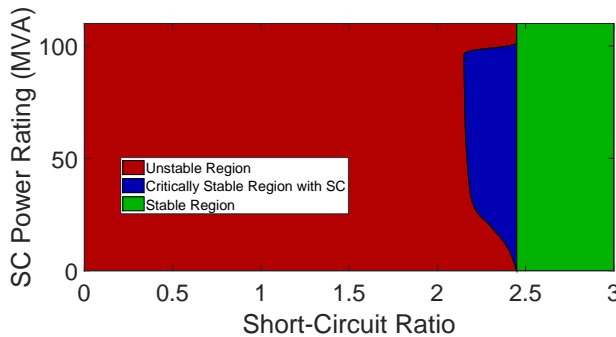


Fig. 4.24: Acceptable SC's power rating S_N for all possible SCRs corresponding to a weak grid in the wind farm under study (240 MW) in Fig. 4.19. Green region is stable. Blue region can be stabilized with a SC. Red region is unstable and cannot be stabilized. Source: [J2].

Hence, the small-signal model under study can be considered suitable and of significant value for choosing the ideal SC to successfully mitigate SSOs and maintain system stability in a wind farm. The obtained results are related to the nominal power of the wind farm system; however, this study can be used for more system operating points. It has to be mentioned, though, that the wind farm's capacity, as well as the specification of the AVR in the SC's model, should be taken into consideration during the stability analysis.

4.4 Conclusion

This chapter has studied the influence of the SC's power rating for small-signal stability of wind farms. Initially a wind farm model is presented, featuring an

4.4. Conclusion

aggregated grid-connected converter that adopts grid-following control, and incorporating passive components like cables and transformers for grid connection. This model is built upon the HVAC CIGRE benchmark model and has been developed to ensure the accuracy of the current controller and the PLL, allowing for the integration of the validated state-space submodel of the SC.

The addition of the SC, at a base rating of 10 MVA, successfully mitigates the harmful SSOs encountered in weak-grid conditions. However, if the parameters of the AVR in the SC are kept constant, the stability analysis based on eigenvalues recommends the highest permissible SC rating to be around half of the wind farm's capacity to prevent the return of instability problems. For a wind farm with a 240 MW rating, the highest permissible SC rating is identified as 107.2 MVA at a certain SCR [J2].

This study obtains its results using time-domain simulations (EMT) and FFT analysis, affirming the reliability of the conclusions drawn. The findings of the developed model are crucial for the ideal selection of a synchronous condenser to tackle SSOs. A notable limitation is that the results are specific to a particular weak grid case, power level, as well as AVR settings of the SC. Future research could explore the effects of varying the SC control and AVR properties and build upon the conclusions presented in this chapter.

Chapter 5

Conclusion

This chapter summarizes the main results and research outcomes of the Ph.D. project *Modeling and Stability Analysis of Converter-Based Wind Turbine Systems*. Initially, a brief summary of the thesis is given, then the research contributions are highlighted. Finally, future research perspectives are discussed.

5.1 Summary

This thesis primarily focuses on investigating the dynamics and the stability impact of wind turbines used in modern power systems. The shift towards modern power systems with a high penetration of wind power necessitates the use of power-electronic converters for grid connection due to their flexibility. However, it is crucial to further study the dynamic phenomena that emerge, particularly SSOs associated with small disturbances, which have been reported at a significant rate globally. An in-depth study of these phenomena is vital to safely integrating more wind power into the main grid, particularly considering the future goal of complete reliance on renewable energy in the power system. Therefore, this Ph.D. project delves into the stability issues that are related to the grid-connected converter systems of wind turbines, and provides insights regarding wind turbine modeling and control design in line with stability concerns. Strategies to mitigate the instability are also proposed.

In *Chapter 1*, the stability issue associated with the integration of wind power into the power system is introduced. Quantitative data on the increasing global wind power capacity is presented, and the technology employed in the design

of wind turbine systems based on power-electronic converters is outlined. A reevaluation of power system stability is conducted, starting with a presentation of traditional power system categories and succeeded by the introduction of new stability categories that emerged after the widespread adoption of converter-based technology. Small-signal instabilities are identified as the primary root of these new stability categories, leading to oscillations in the system. An overview of different ways of small-signal modeling for wind turbines is given, with their key characteristics emphasized. Solutions for SSOs are divided into software and hardware solutions and brought forward. The research objectives to address these challenges are defined, highlighting the necessity for accurate small-signal modeling of wind turbines for investigating the dynamic phenomena that might potentially occur.

In *Chapter 2*, the small-signal modelling of wind turbine systems is discussed in depth. An analytical design of a non-linear state-space model for a grid-connected wind turbine's VSC is described. Emphasis is given to state-space based submodels of the PLL, the current control loops, the LC filter, and the digital time delay for studying the system's dynamics under different grid strength conditions. Linearization is implemented around the system's equilibrium points and stability is evaluated through eigenvalue analysis. Valuable insights into the model's sensitivity under different SCR conditions are provided from the eigenvalue analysis associated with each controller [C1]. Time-domain simulations validate the model, and enable the use of the model for further stability studies.

Therefore in *Chapter 3*, the small-signal model is enhanced with an outer-loop AVC controller that regulates the voltage at the PCC, and the impact of the AVC's design on the system's stability is under study. The stability impacts of the AVC controller are studied through eigenvalue-based stability analysis, revealing that the cutoff frequency of the AVC's low-pass filter influences the PLL and AVC bandwidths of instability, as well as the corresponding critical oscillation frequencies. This phenomenon has been observed in both weak and strong grids. Consequently, the small-signal stability regions of the PLL and AVC bandwidth can be identified for the range of the AVC's low-pass filter's cutoff frequency under study. The ways the AVC's design influences the aforementioned stability regions in relation to grid strength conditions are determined, and a high precision validation is provided by the time-domain model [J1].

To reinforce this study further, given that the previously discussed model for

5.2. Main Contributions of the Thesis

the single VSC has been corroborated in various test scenarios, a small-signal model of a multi-VSC is formulated based on a generalized methodology, where the VSC submodels represent the wind turbines of a wind farm. The stability of the multi-VSC model is examined in both the low and high frequency ranges after evaluating the sensitivity of all the controllers' parameters for one VSC of the system. The precision of this model has been confirmed to be very high, establishing its suitability to describe the small-signal interactions in a multi-VSC configuration [J3].

The study in the previous chapters gave the opportunity to do a proper tuning of the controllers based on their eigenvalue trends in order to overcome instability phenomena, especially at low frequencies. *Chapter 4* examines the effect of a synchronous condenser connected to an offshore wind farm in mitigating SSOs during weak grid conditions. Specifically, the influence of a synchronous condenser's power rating on the small-signal stability of a wind farm is investigated, where an aggregated grid-connected converter is modeled for the turbines in the wind farm. The study demonstrates that existing SSOs can effectively be mitigated by a properly selected synchronous condenser, but an incorrect selection can give rise to detrimental low-frequency oscillations. The range of accepted power ratings of a synchronous condenser is related to the wind farm's capacity, given that the AVR settings remain unchanged [J2].

5.2 Main Contributions of the Thesis

The main research contributions of this Ph.D. project, based on the research objectives as described in *Chapter 1*, are summarized below.

Providing an in-depth understanding of the accuracy of small-signal model of wind turbine and its sensitivity to different operating cases

A state-space model of a grid-connected VSC with grid-following control has been developed and evaluated under different SCR conditions. This model took into account the impacts of PLL dynamics, current control dynamics, LC filter, and digital time delay. The resulting eigenvalue trajectories were then thoroughly assessed through time-domain simulations and frequency analysis when the system approached instability. The high accuracy of the time-domain model in validating the small-signal analysis across different grid strength test

cases has verified the controllers' sensitivity and formed the foundation for all the models and control methodologies introduced in this Ph.D. project.

Identifying the impact of the outer-loop AVC controller's design on the stability regions of PLL and AVC bandwidths in a grid-connected converter system

An AVC outer-loop controller has been incorporated into the grid-connected VSC's small-signal model, and its stability impact has been examined for several grid strength cases. The stability regions of the PLL and the AVC were defined, along with the oscillation frequency, in accordance with the selected AVC's low-pass filter. These findings provide valuable insight into how to select the AVC controller's low-pass filter in order to avoid low-frequency instability and guide for a proper tuning of the PLL and AVC based on the AVC's design and the SCR level.

Developing a multi-VSC small-signal model to illustrate instabilities in the low and high frequency range

A modular nonlinear state-space modelling approach with multiple VSCs in a power system has been developed, with each VSC representing a wind turbine within a wind farm. The approach applied to determine the equilibrium points is generalized and applicable to various scenarios with different control and system parameters, as the formulas derived for the steady-state currents can be utilized for several cases of multi-VSC systems. Their accuracy is corroborated by time-domain results in steady states. Eigenvalue analysis and participation factor analysis present the influence of each VSC's controller on system stability across both high and low-frequency range. Thus, the model serves as a comprehensive tool, accurately depicting the small-signal interactions on the grid side of a wind farm, and adaptable to a range of control and system parameters.

Identifying the power rating range of a synchronous condenser for mitigating SSOs in a wind farm

The effect of incorporating a synchronous condenser into a wind farm's model has been examined, focusing on mitigating SSOs under weak grid conditions. An acceptable power rating range of the synchronous condenser was identified via the corresponding eigenvalue trajectories in small-signal analysis, taking into

5.3. Research Perspectives and Future Work

account grid strength conditions and the specific system parameters of the simulated wind farm model under study. This analysis gives the foundation for a proper selection of a synchronous condenser power rating and controller design for addressing critical SSOs, and offers a starting point for future studies regarding the impact of the remaining synchronous condenser's parameters.

5.3 Research Perspectives and Future Work

This three-year Ph.D. project tried to cover some main challenges in regards to the modeling and the stability analysis of converter-based wind turbine systems. As the wind power penetration will be increasing in the upcoming years, this research field will bring many more challenges that will need to be addressed on an academic as well as an industrial level. Aside from the work in this thesis, some possible work are worth to continue with in the future, which are listed as follows:

- The focus of this research has primarily been on the sensitivity of grid-following converter control, which is currently the dominant control structure of converter-based systems. Nevertheless, with the increasing interest in grid-forming control, the necessity to study its sensitivity to different grid strength scenarios cannot be undermined. The scope of the study could be broadened to include systems employing mixed grid-following and grid-forming control as well as pure grid-forming control.
- Similarly, the influence of a synchronous condenser on the stability of wind farms was investigated using a converter-based system regulated by grid-following control. It would be interesting to apply the same system parameters to a system employing grid-forming control, in order to determine whether the introduction of a synchronous condenser yields similar outcomes in mitigating SSOs.
- The research direction of this thesis was primarily aligned with the study of GSC control. However, incorporating MSC control into the analysis could offer a more complete understanding of the control dynamics of wind turbines and its influence to the grid. That also includes the dc-link dynamics between the MSC and GSC. Along with the MSC and GSC dynamics, it could also be interesting to study the impact of storage in the system.

- The core of the research in this thesis was the investigation of small-signal disturbances, with large-signal disturbances being primarily addressed through time-domain simulation modeling. Considering the likelihood of power systems facing severe disturbances, there is a critical need for further research into large-signal modeling, as well as the development of effective system restoration strategies. Here, challenges can appear with large-scale system analysis, as they can be complicated and time consuming to simulate.
- In *Chapter 2* and *Chapter 3*, a small-scale converter system was used to build the corresponding small-signal models and the EMT models for time-domain simulations. This approach provides a controlled, risk-free environment that is essential for future laboratory tests while ensuring the relevance of stability impacts. However, it is important to acknowledge the realism and specific differences present in large-scale power systems, such as the one explored in *Chapter 4*, especially with respect to controller designs. Therefore, future research could involve designing and analyzing large-scale systems, where hardware-in-the-loop tests could be employed for validation, thus bridging the gap between small-scale simulations and real-world applicability. Also for the large systems, the switching frequency could be lower and impact the analysis.

References

- [1] F. M. Gonzalez-Longatt, M. N. Acosta, H. R. Chamorro, and J. L. Rueda Torres, *Modelling and Simulation of Power Electronic Converter Dominated Power Systems in PowerFactory*. Springer International Publishing, 2021, ISBN: 978-3-030-54123-1.
- [2] IRENA and CPI(2023), “Global landscape of renewable energy finance,” Abu Dhabi, International Renewable Energy Agency, 2023.
- [3] REN21, “Renewables in energy supply,” Renewables 2023 Global Status Report collection, 2023.
- [4] Global Wind Energy Council, “Global Wind Report 2023,” Global Wind Energy Council: Belgium, Brussels, 2023.
- [5] F. Blaabjerg and K. Ma, “Wind energy systems,” *Proceedings of the IEEE*, vol. 105, no. 11, pp. 2116–2131, 2017.
- [6] Z. Chen, J. M. Guerrero, and F. Blaabjerg, “A review of the state of the art of power electronics for wind turbines,” *IEEE Transactions on Power Electronics*, vol. 24, no. 8, pp. 1859–1875, 2009.
- [7] M. Liserre, R. Cárdenas, M. Molinas, and J. Rodriguez, “Overview of multi-MW wind turbines and wind parks,” *IEEE Transactions on Industrial Electronics*, vol. 58, no. 4, pp. 1081–1095, 2011.
- [8] R. Peña, J. Clare, and G. Asher, “Doubly fed induction generator using back-to-back PWM converters and its application to variable-speed wind-energy generation,” *IEE Proceedings - Electric Power Applications*, vol. 143, pp. 231–241, May 1996.
- [9] H. Polinder, J. A. Ferreira, B. B. Jensen, A. B. Abrahamsen, K. Atallah, and R. A. McMahon, “Trends in wind turbine generator systems,” *IEEE Journal of Emerging and Selected Topics in Power Electronics*, vol. 1, no. 3, pp. 174–185, 2013.
- [10] H. Polinder, F. van der Pijl, G.-J. de Vilder, and P. Tavner, “Comparison of direct-drive and geared generator concepts for wind turbines,” *IEEE Transactions on Energy Conversion*, vol. 21, no. 3, pp. 725–733, 2006.

- [11] A. Ragheb and M. Ragheb, “Wind turbine gearbox technologies,” in *Proc. of 2010 1st International Nuclear Renewable Energy Conference (IN-REC)*, 2010, pp. 1–8.
- [12] F. Blaabjerg, Y. Yang, K. A. Kim, and J. Rodriguez, “Power electronics technology for large-scale renewable energy generation,” *Proceedings of the IEEE*, vol. 111, no. 4, pp. 335–355, 2023.
- [13] ENTSO-E, “HVDC links in system operations,” Brussels, European Institute of Transmission System Operators for Electricity, 2019.
- [14] Energinet DK, “Technical regulation 3.2.5 for wind power plants above 11 kW,” Tech. Rep., 2016. [Online]. Available: <https://en.energinet.dk/Electricity/Rules-and-Regulations/Regulations-for-grid-connection/>
- [15] P. Kundur, J. Paserba, V. Ajjarapu, G. Andersson, A. Bose, C. Canizares, N. Hatziargyriou, D. Hill, A. Stankovic, C. Taylor, T. Van Cutsem, and V. Vittal, “Definition and classification of power system stability IEEE/CIGRE joint task force on stability terms and definitions,” *IEEE Transactions on Power Systems*, vol. 19, no. 3, pp. 1387–1401, 2004.
- [16] N. Hatziargyriou, J. Milanovic, C. Rahmann, V. Ajjarapu, C. Canizares, I. Erlich, D. Hill, I. Hiskens, I. Kamwa, B. Pal, P. Pourbeik, J. Sanchez-Gasca, A. Stankovic, T. Van Cutsem, V. Vittal, and C. Vournas, “Definition and classification of power system stability – revisited extended,” *IEEE Transactions on Power Systems*, vol. 36, no. 4, pp. 3271–3281, 2021.
- [17] P. Kundur, *Power system stability and control*, 1st ed. McGraw-Hill, Inc., 1994, ISBN: 978-0-07-035958-X.
- [18] R. Teodorescu, M. Liserre, and P. Rodríguez, *Grid Converters for Photovoltaic and Wind Power Systems.*, 1st ed. Wiley, 2011, ISBN: 978-0-470-05751-3.
- [19] T. v. Cutsem and C. Vournas, *Voltage Stability of Electric Power Systems*, 1st ed. Springer-Verlag, 2007, ISBN: 978-0-387-75535-9.
- [20] P. Tielens and D. Van Hertem, “The relevance of inertia in power systems,” *Renewable and Sustainable Energy Reviews*, vol. 55, pp. 999–1009, 2016.

References

- [21] P. Pourbeik, S. Soni, A. Gaikwad, and V. Chadliev, "Providing primary frequency response from photovoltaic power plants," in *Proc. of CIGRE Symp. 2017*, 2017, p. 1–10.
- [22] B. Kroposki, B. Johnson, Y. Zhang, V. Gevorgian, P. Denholm, B.-M. Hodge, and B. Hannegan, "Achieving a 100% renewable grid: Operating electric power systems with extremely high levels of variable renewable energy," *IEEE Power and Energy Magazine*, vol. 15, no. 2, pp. 61–73, 2017.
- [23] X. Wang and F. Blaabjerg, "Harmonic stability in power electronic-based power systems: Concept, modeling, and analysis," *IEEE Transactions on Smart Grid*, vol. 10, no. 3, pp. 2858–2870, 2019.
- [24] E. Ebrahimzadeh, F. Blaabjerg, X. Wang, and C. L. Bak, "Harmonic stability and resonance analysis in large PMSG-based wind power plants," *IEEE Transactions on Sustainable Energy*, vol. 9, no. 1, pp. 12–23, 2018.
- [25] X. Wang, F. Blaabjerg, and W. Wu, "Modeling and analysis of harmonic stability in an AC power-electronics-based power system," *IEEE Transactions on Power Electronics*, vol. 29, no. 12, pp. 6421–6432, 2014.
- [26] J. He, Y. W. Li, D. Bosnjak, and B. Harris, "Investigation and active damping of multiple resonances in a parallel-inverter-based microgrid," *IEEE Transactions on Power Electronics*, vol. 28, no. 1, pp. 234–246, 2013.
- [27] Y. Xu, S. Zhao, Y. Cao, and K. Sun, "Understanding subsynchronous oscillations in DFIG-based wind farms without series compensation," *IEEE Access*, vol. 7, pp. 107 201–107 210, 2019.
- [28] Y. Xu and Y. Cao, "Sub-synchronous oscillation in PMSGs based wind farms caused by amplification effect of GSC controller and PLL to harmonics," *IET Renewable Power Generation*, vol. 12, no. 7, pp. 844–850, 2018.
- [29] J. Z. Zhou, H. Ding, S. Fan, Y. Zhang, and A. M. Gole, "Impact of short-circuit ratio and phase-locked-loop parameters on the small-signal behavior of a VSC-HVDC converter," *IEEE Transactions on Power Delivery*, vol. 29, no. 5, pp. 2287–2296, 2014.

- [30] S.-H. Huang, J. Schmall, J. Conto, J. Adams, Y. Zhang, and C. Carter, "Voltage control challenges on weak grids with high penetration of wind generation: ERCOT experience," in *Proc. of 2012 IEEE Power and Energy Society General Meeting*, 2012, pp. 1–7.
- [31] "Reader's guide to subsynchronous resonance," *IEEE Transactions on Power Systems*, vol. 7, no. 1, pp. 150–157, 1992.
- [32] J. Adams, C. Carter, and S.-H. Huang, "ERCOT experience with subsynchronous control interaction and proposed remediation," in *Proc. of PES TD 2012*, 2012, pp. 1–5.
- [33] K. Narendra, D. Fedirchuk, R. Midence, N. Zhang, A. Mulawarman, P. Mysore, and V. Sood, "New microprocessor based relay to monitor and protect power systems against sub-harmonics," in *Proc. of 2011 IEEE Electrical Power and Energy Conference*, 2011, pp. 438–443.
- [34] L. Wang, X. Xie, Q. Jiang, H. Liu, Y. Li, and H. Liu, "Investigation of SSR in practical DFIG-based wind farms connected to a series-compensated power system," *IEEE Transactions on Power Systems*, vol. 30, no. 5, pp. 2772–2779, 2015.
- [35] Y. Li, L. Fan, and Z. Miao, "Replicating real-world wind farm SSR events," *IEEE Transactions on Power Delivery*, vol. 35, no. 1, pp. 339–348, 2020.
- [36] L. Yunhong, L. Hui, C. Xiaowei, H. Jing, and Y. Li, "Impact of PMSG on SSR of DFIGs connected to series-compensated lines based on the impedance characteristics," *The Journal of Engineering*, vol. 2017, pp. 2184–2187(3), 2017.
- [37] X. Xie, X. Zhang, H. Liu, H. Liu, Y. Li, and C. Zhang, "Characteristic analysis of subsynchronous resonance in practical wind farms connected to series-compensated transmissions," *IEEE Transactions on Energy Conversion*, vol. 32, no. 3, pp. 1117–1126, 2017.
- [38] F. Blaabjerg, R. Teodorescu, M. Liserre, and A. Timbus, "Overview of control and grid synchronization for distributed power generation systems," *IEEE Transactions on Industrial Electronics*, vol. 53, no. 5, pp. 1398–1409, 2006.

References

- [39] L. Harnefors, X. Wang, A. G. Yepes, and F. Blaabjerg, “Passivity-based stability assessment of grid-connected VSCs—an overview,” *IEEE Journal of Emerging and Selected Topics in Power Electronics*, vol. 4, no. 1, pp. 116–125, 2016.
- [40] L. Harnefors, R. Finger, X. Wang, H. Bai, and F. Blaabjerg, “VSC input-admittance modeling and analysis above the Nyquist frequency for passivity-based stability assessment,” *IEEE Transactions on Industrial Electronics*, vol. 64, no. 8, pp. 6362–6370, 2017.
- [41] X. Wang, F. Blaabjerg, and P. C. Loh, “Passivity-based stability analysis and damping injection for multiparalleled VSCs with LCL filters,” *IEEE Transactions on Power Electronics*, vol. 32, no. 11, pp. 8922–8935, 2017.
- [42] X. Wang, L. Harnefors, and F. Blaabjerg, “Unified impedance model of grid-connected voltage-source converters,” *IEEE Transactions on Power Electronics*, vol. 33, no. 2, pp. 1775–1787, 2018.
- [43] D. Yang, X. Wang, and F. Blaabjerg, “Sideband harmonic instability of paralleled inverters with asynchronous carriers,” *IEEE Transactions on Power Electronics*, vol. 33, no. 6, pp. 4571–4577, 2018.
- [44] H. Huang, C. Mao, J. Lu, and D. Wang, “Small-signal modelling and analysis of wind turbine with direct drive permanent magnet synchronous generator connected to power grid,” *IET Renewable Power Generation*, vol. 6, pp. 48–58, 2012.
- [45] X. Wang, M. G. Taul, H. Wu, Y. Liao, F. Blaabjerg, and L. Harnefors, “Grid-synchronization stability of converter-based resources—an overview,” *IEEE Open Journal of Industry Applications*, vol. 1, pp. 115–134, 2020.
- [46] L. Kocewiak, R. Blasco-Gimenez, C. Buchhagen, J. B. Kwon, Y. Sun, A. S. Trevisan, M. Larsson, and X. Wang, “Overview status and outline of stability analysis in converter-based power systems,” in *Proc. of 19th Wind Integration Workshop*, 2020, pp. 1–10.
- [47] L. Kocewiak, R. Blasco-Gimenez, C. Buchhagen, J. B. Kwon, M. Larsson, Y. Sun, and X. Wang, “Practical aspects of small-signal stability analy-

- sis and instability mitigation,” in *Proc. of 21st Wind Solar Integration Workshop (WIW 2022)*, vol. 2022, 2022, pp. 138–150.
- [48] I. Vieto and J. Sun, “Small-signal impedance modelling of Type-III wind turbine,” in *Proc. of 2015 IEEE Power Energy Society General Meeting*, 2015, pp. 1–5.
- [49] B. Wen, D. Boroyevich, R. Burgos, P. Mattavelli, and Z. Shen, “Analysis of D-Q small-signal impedance of grid-tied inverters,” *IEEE Transactions on Power Electronics*, vol. 31, no. 1, pp. 675–687, 2016.
- [50] Y. Liao and X. Wang, “Impedance-based stability analysis for interconnected converter systems with open-loop RHP poles,” *IEEE Transactions on Power Electronics*, vol. 35, no. 4, pp. 4388–4397, 2020.
- [51] C. Yoon, X. Wang, C. L. Bak, and F. Blaabjerg, “Stabilization of multiple unstable modes for small-scale inverter-based power systems with impedance-based stability analysis,” in *Proc. of 2015 IEEE Applied Power Electronics Conference and Exposition (APEC)*, 2015, pp. 1202–1208.
- [52] M. Amin and M. Molinas, “Small-signal stability assessment of power electronics based power systems: A discussion of impedance- and eigenvalue-based methods,” *IEEE Transactions on Industry Applications*, vol. 53, no. 5, pp. 5014–5030, 2017.
- [53] J. Kwon, X. Wang, F. Blaabjerg, C. L. Bak, A. R. Wood, and N. R. Watson, “Linearized modeling methods of AC–DC converters for an accurate frequency response,” *IEEE Journal of Emerging and Selected Topics in Power Electronics*, vol. 5, no. 4, pp. 1526–1541, 2017.
- [54] C. Buchhagen, C. Rauscher, A. Menze, and J. Jung, “Borwin1 - first experiences with harmonic interactions in converter dominated grids,” in *Proc. of International ETG Congress 2015; Die Energiewende - Blueprints for the new energy age*, 2015, pp. 1–7.
- [55] N. Kroutikova, C. A. Hernandez-Aramburo, and T. C. Green, “State-space model of grid-connected inverters under current control mode,” *IET Electric Power Applications*, vol. 1, pp. 329–338, May 2007.

References

- [56] A. Egea-Alvarez, S. Fekriasl, F. Hassan, and O. Gomis-Bellmunt, “Advanced vector control for voltage source converters connected to weak grids,” *IEEE Transactions on Power Systems*, vol. 30, no. 6, pp. 3072–3081, 2015.
- [57] G. S. Misyris, J. A. Mermet-Guyennet, S. Chatzivasileiadis, and T. Weckesser, “Grid supporting VSCs in power systems with varying inertia and short-circuit capacity,” in *Proc. of 2019 IEEE Milan PowerTech*, 2019, pp. 1–6.
- [58] M. Amin, J. A. Suul, S. D’Arco, E. Tedeschi, and M. Molinas, “Impact of state-space modelling fidelity on the small-signal dynamics of VSC-HVDC systems,” in *Proc. of 11th IET International Conference on AC and DC Power Transmission*, 2015, pp. 1–11.
- [59] F. Cecati, R. Zhu, M. Liserre, and X. Wang, “Nonlinear modular state-space modeling of power-electronics-based power systems,” *IEEE Transactions on Power Electronics*, vol. 37, no. 5, pp. 6102–6115, 2022.
- [60] F. Mandrile, S. Musumeci, E. Carpaneto, R. Bojoi, T. Dragičević, and F. Blaabjerg, “State-space modeling techniques of emerging grid-connected converters,” *Energies*, vol. 13, no. 18, 2020.
- [61] L. Marin, A. Tarrasó, I. Candela, and P. Rodriguez, “Stability analysis of a droop-controlled grid-connected VSC,” in *Proc. of 2018 IEEE Energy Conversion Congress and Exposition (ECCE)*, 2018, pp. 4161–4167.
- [62] D. Yang and X. Wang, “Unified modular state-space modeling of grid-connected voltage-source converters,” *IEEE Transactions on Power Electronics*, vol. 35, no. 9, pp. 9700–9715, 2020.
- [63] L. Harnefors, M. Bongiorno, and S. Lundberg, “Input-admittance calculation and shaping for controlled voltage-source converters,” *IEEE Transactions on Industrial Electronics*, vol. 54, no. 6, pp. 3323–3334, 2007.
- [64] H. Zhang, L. Harnefors, X. Wang, J.-P. Hasler, S. Östlund, C. Danielsson, and H. Gong, “Loop-at-a-time stability analysis for grid-connected voltage-source converters,” *IEEE Journal of Emerging and Selected Topics in Power Electronics*, vol. 9, no. 5, pp. 5807–5821, 2021.

- [65] G. F. Gontijo, M. K. Bakhshizadeh, H. Kocewiak, and R. Teodorescu, “State space modeling of an offshore wind power plant with an MMC-HVDC connection for an eigenvalue-based stability analysis,” *IEEE Access*, vol. 10, pp. 82 844–82 869, 2022.
- [66] S. Rezaee, A. Radwan, M. Moallem, and J. Wang, “Voltage source converters connected to very weak grids: Accurate dynamic modeling, small-signal analysis, and stability improvement,” *IEEE Access*, vol. 8, pp. 201 120–201 133, 2020.
- [67] A. Musengimana, H. Li, X. Zheng, and Y. Yu, “Small-signal model and stability control for grid-connected PV inverter to a weak grid,” *Energies*, vol. 14, no. 13, 2021.
- [68] H. Gholami-Khesht, P. Davari, M. Novak, and F. Blaabjerg, “A probabilistic framework for the robust stability and performance analysis of grid-tied voltage source converters,” *Applied Sciences*, vol. 12, no. 15, 2022.
- [69] A. J. Agbemuko, J. L. Domínguez-García, O. Gomis-Bellmunt, and L. Harnefors, “Passivity-based analysis and performance enhancement of a vector controlled VSC connected to a weak AC grid,” *IEEE Transactions on Power Delivery*, vol. 36, no. 1, pp. 156–167, 2021.
- [70] Y. Wang, X. Wang, Z. Chen, and F. Blaabjerg, “Small-signal stability analysis of inverter-fed power systems using component connection method,” *IEEE Transactions on Smart Grid*, vol. 9, no. 5, pp. 5301–5310, 2018.
- [71] “A bibliography for the study of subsynchronous resonance between rotating machines and power systems,” *IEEE Transactions on Power Apparatus and Systems*, vol. 95, no. 1, pp. 216–218, 1976.
- [72] Y. Cheng, L. Fan, J. Rose, S.-H. Huang, J. Schmall, X. Wang, X. Xie, J. Shair, J. R. Ramamurthy, N. Modi, C. Li, C. Wang, S. Shah, B. Pal, Z. Miao, A. Isaacs, J. Mahseredjian, and J. Zhou, “Real-world subsynchronous oscillation events in power grids with high penetrations of inverter-based resources,” *IEEE Transactions on Power Systems*, vol. 38, no. 1, pp. 316–330, 2023.

References

- [73] K. Gu, F. Wu, and X.-P. Zhang, “Sub-synchronous interactions in power systems with wind turbines: a review,” *IET Renewable Power Generation*, vol. 13, no. 1, pp. 4–15, 2019.
- [74] V. Sewdien, X. Wang, J. Rueda Torres, and M. van der Meijden, “Critical review of mitigation solutions for SSO in modern transmission grids,” *Energies*, vol. 13, no. 13, 2020.
- [75] H. Liu, X. Xie, Y. Li, H. Liu, and Y. Hu, “Mitigation of SSR by embedding subsynchronous notch filters into DFIG converter controllers,” *IET Generation, Transmission Distribution*, vol. 11, pp. 2888–2896, 2017.
- [76] H. He, D. Lv, L. Wen, W. Lu, H. Geng, and J. Gao, “Analysis and suppression strategies of sub-synchronous resonance on DFIG,” in *Proc. of 2018 IEEE International Power Electronics and Application Conference and Exposition (PEAC)*, 2018, pp. 1–5.
- [77] H. Liu, X. Xie, J. He, H. Liu, and Y. Li, “Damping DFIG-associated SSR by adding subsynchronous suppression filters to DFIG converter controllers,” in *Proc. of 2016 IEEE Power and Energy Society General Meeting (PESGM)*, 2016, pp. 1–5.
- [78] H. Liu, X. Xie, Y. Li, H. Liu, and Y. Li, “Damping DFIG-associated SSR with subsynchronous suppression filters: A case study on a practical wind farm system,” in *Proc. of International Conference on Renewable Power Generation (RPG 2015)*, 2015, pp. 1–6.
- [79] Y. Cao, W. Wang, Y. Li, Y. Tan, C. Chen, L. He, U. Häger, and C. Rehtanz, “A virtual synchronous generator control strategy for VSC-MTDC systems,” *IEEE Transactions on Energy Conversion*, vol. 33, no. 2, pp. 750–761, 2018.
- [80] J. R. Pérez, J. A. Suul, S. D’Arco, A. Rodríguez-Cabero, and M. Prodanovic, “Virtual synchronous machine control of VSC HVDC for power system oscillation damping,” in *Proc. of IECON 2018 - 44th Annual Conference of the IEEE Industrial Electronics Society*, 2018, pp. 6026–6031.
- [81] L. Wang, J. Peng, Y. You, and H. Ma, “SSCI performance of DFIG with direct controller,” *IET Generation, Transmission Distribution*, vol. 11, pp. 2697–2702(5), July 2017.

- [82] Y. Zheng and Y. Li, “Stability analysis of doubly-fed wind power generation system based on phase-locked loop,” in *Proc. of 2008 International Conference on Electrical Machines and Systems*, 2008, pp. 2251–2254.
- [83] W. Du, W. Dong, Y. Wang, and H. Wang, “Small-disturbance stability of a wind farm with virtual synchronous generators under the condition of weak grid connection,” *IEEE Transactions on Power Systems*, vol. 36, no. 6, pp. 5500–5511, 2021.
- [84] K. Gu, F. Wu, X.-P. Zhang, P. Ju, H. Zhou, J. Luo, and J. Li, “SSR analysis of DFIG-based wind farm with VSM control strategy,” *IEEE Access*, vol. 7, pp. 118 702–118 711, 2019.
- [85] R. K. Varma, S. Auddy, and Y. Semsedini, “Mitigation of subsynchronous resonance in a series-compensated wind farm using FACTS controllers,” *IEEE Transactions on Power Delivery*, vol. 23, no. 3, pp. 1645–1654, 2008.
- [86] H. Xie and M. M. de Oliveira, “Mitigation of SSR in presence of wind power and series compensation by SVC,” in *Proc. of 2014 International Conference on Power System Technology*, 2014, pp. 2819–2826.
- [87] A. Moharana, R. K. Varma, and R. Seethapathy, “SSR alleviation by STATCOM in induction-generator-based wind farm connected to series compensated line,” *IEEE Transactions on Sustainable Energy*, vol. 5, no. 3, pp. 947–957, 2014.
- [88] M. S. El-Moursi, B. Bak-Jensen, and M. H. Abdel-Rahman, “Novel STATCOM controller for mitigating SSR and damping power system oscillations in a series compensated wind park,” *IEEE Transactions on Power Electronics*, vol. 25, no. 2, pp. 429–441, 2010.
- [89] A. Moharana, R. K. Varma, and R. Seethapathy, “SSR mitigation in wind farm connected to series compensated transmission line using STATCOM,” in *Proc. of 2012 IEEE Power Electronics and Machines in Wind Applications*, 2012, pp. 1–8.
- [90] L. Ding, X. Lu, and J. Tan, “Small-signal stability analysis of low-inertia power grids with inverter-based resources and synchronous condensers,” in *Proc. of 2022 IEEE Power Energy Society Innovative Smart Grid Technologies Conference (ISGT)*, 2022, pp. 1–5.

References

- [91] M. Nedd, C. Booth, and K. Bell, “Potential solutions to the challenges of low inertia power systems with a case study concerning synchronous condensers,” in *Proc. of 2017 52nd International Universities Power Engineering Conference (UPEC)*, 2017, pp. 1–6.
- [92] H. T. Nguyen, G. Yang, A. H. Nielsen, and P. H. Jensen, “Frequency stability improvement of low inertia systems using synchronous condensers,” in *Proc. of 2016 IEEE International Conference on Smart Grid Communications (SmartGridComm)*, 2016, pp. 650–655.
- [93] V. Arayamparambil Vinaya Mohanan, I. M. Mareels, R. J. Evans, and R. R. Kolluri, “Stabilising influence of a synchronous condenser in low inertia networks,” *IET Generation, Transmission & Distribution*, vol. 14, no. 17, pp. 3582–3593, 2020.
- [94] G. Zhou, D. Wang, A. Atallah, F. McElvain, R. Nath, J. Jontry, C. Bolton, H. Lin, and A. Haselbauer, “Synchronous condenser applications: Under significant resource portfolio changes,” *IEEE Power and Energy Magazine*, vol. 17, no. 4, pp. 35–46, 2019.
- [95] H. T. Nguyen, G. Yang, A. H. Nielsen, and P. H. Jensen, “Combination of synchronous condenser and synthetic inertia for frequency stability enhancement in low-inertia systems,” *IEEE Transactions on Sustainable Energy*, vol. 10, no. 3, pp. 997–1005, 2019.
- [96] S. Hadavi, M. Z. Mansour, and B. Bahrani, “Optimal allocation and sizing of synchronous condensers in weak grids with increased penetration of wind and solar farms,” *IEEE Journal on Emerging and Selected Topics in Circuits and Systems*, vol. 11, no. 1, pp. 199–209, 2021.
- [97] Y. Wang, L. Wang, and Q. Jiang, “Impact of synchronous condenser on sub/super-synchronous oscillations in wind farms,” *IEEE Transactions on Power Delivery*, vol. 36, no. 4, pp. 2075–2084, 2021.
- [98] R. P. Jiménez, C. A. Platero, M. E. Sánchez, and E. R. Barneto, “Synchronous condenser for european grid code compliance: A case study of a PV power plant in Spain,” *IEEE Access*, vol. 11, pp. 54 713–54 723, 2023.

- [99] S. Ganjefar and M. Farahani, “Comparing SVC and synchronous condenser performance in mitigating torsional oscillations,” *International Transactions on Electrical Energy Systems*, vol. 25, no. 11, pp. 2819–2830, 2015.
- [100] L. Bao, L. Fan, and Z. Miao, “Comparison of synchronous condenser and STATCOM for wind farms in weak grids,” in *2020 52nd North American Power Symposium (NAPS)*, 2021, pp. 1–6.
- [101] J. Jia, G. Yang, A. H. Nielsen, and V. Gevorgian, “Investigation on the combined effect of VSC-based sources and synchronous condensers under grid unbalanced faults,” *IEEE Transactions on Power Delivery*, vol. 34, no. 5, pp. 1898–1908, 2019.
- [102] J. Jia, G. Yang, A. H. Nielsen, and P. Rønne-Hansen, “Impact of VSC control strategies and incorporation of synchronous condensers on distance protection under unbalanced faults,” *IEEE Transactions on Industrial Electronics*, vol. 66, no. 2, pp. 1108–1118, 2019.
- [103] S. Hadavi, J. Saunderson, A. Mehrizi-Sani, and B. Bahrani, “A planning method for synchronous condensers in weak grids using semi-definite optimization,” *IEEE Transactions on Power Systems*, vol. 38, no. 2, pp. 1632–1641, 2023.
- [104] L. Richard, Nahid-Al-Masood, T. K. Saha, W. Tushar, and H. Gu, “Optimal allocation of synchronous condensers in wind dominated power grids,” *IEEE Access*, vol. 8, pp. 45 400–45 410, 2020.
- [105] J. Jia, G. Yang, A. H. Nielsen, E. Muljadi, P. Weinreich-Jensen, and V. Gevorgian, “Synchronous condenser allocation for improving system short circuit ratio,” in *2018 5th International Conference on Electric Power and Energy Conversion Systems (EPECS)*, 2018, pp. 1–5.
- [106] F. Arraño-Vargas, Z. Shen, S. Jiang, J. Fletcher, and G. Konstantinou, “Challenges and mitigation measures in power systems with high share of renewables—The Australian experience,” *Energies*, vol. 15, no. 2, 2022.
- [107] R. Rosso, “Stability analysis of converter control strategies for power electronics-dominated power systems,” Ph.D. dissertation, Christian-Albrecht University of Kiel, 2020.

References

- [108] Q. Fu, W. J. Du, G. Y. Su, and H. F. Wang, “Dynamic interactions between VSC-HVDC and power system with electromechanical oscillation modes - a comparison between the power synchronization control and vector control,” in *Proc. of 2016 IEEE PES Asia-Pacific Power and Energy Engineering Conference (APPEEC)*, 2016, pp. 949–956.
- [109] L. Zhang, L. Harnefors, and H.-P. Nee, “Power-synchronization control of grid-connected voltage-source converters,” *IEEE Transactions on Power Systems*, vol. 25, no. 2, pp. 809–820, 2010.
- [110] M. B. Dowlatabadi, “Harmonic modelling, propagation and mitigation for large wind power plants connected via extra long HVAC cables: With special focus on harmonic stability,” Ph.D. dissertation, Aalborg Universitetsforlag, 2018.
- [111] K. Martin, A. Margitova, and M. Kolcun, “Modeling of synchronous machines including voltage regulation,” in *Przegląd Elektrotechniczny*, vol. 95, no. 7, 2019, p. 125–132.
- [112] P. M. Anderson, B. L. Agrawal, and J. E. Van Ness, *Subsynchronous Resonance in Power Systems*, 1st ed. IEEE Press, 1990, ISBN: 978-0780353503.
- [113] Working Group B4.62, “Connection of wind farms to weak AC networks,” CIGRE Technical Brochure, 2016.

